CONFIGURATION OF MULTIPLE INPUT MULTIPLE OUTPUT ANTENNA ARRAYS FOR WIRELESS COMMUNICATIONS IN UNDERGROUND MINES

by

Arghavan Emami Forooshani

B.Sc., Iran University of Science and Technology, 2000
M.Sc., University of Manitoba, 2006

A THESIS SUBMITTED IN PARTIAL FULLFILLMENT OF
THE REQUIREMENTS FOR THE DEGREE OF
DOCTOR OF PHILOSOPHY
in
The Faculty of Graduate and Postdoctral Studies
(Electrical and Computer Engineering)

THE UNIVERSITY OF BRITISH COLUMBIA
(Vancouver)

August 2013

ABSTRACT

In recent years, the underground mining community has begun to embrace standards-based short-range wireless communications technology as a key part of their strategy for enhancing the safety and productivity of their operations. Here, we show how the significant differences between wireless propagation in conventional surface environments and underground mines affect the design of modern wireless communications systems based upon multiple-input multiple-output (MIMO) antenna array technology. In order to achieve this goal, we have employed a variety of approaches to characterize wireless propagation (and MIMO-based wireless system performance) in underground environments representative of those found in modern hard rock mines, including: 1) field measurements collected using a custom-designed channel sounder in both a building service tunnel at the University of British Columbia and an underground lead-zinc mine at Myra Falls, BC, 2) simulations based upon ray-tracing in representative environments and 3) theoretical models based upon waveguide mode expansion in representative environments. We have used the results obtained: 1) to determine the reduction in the angular spread of multipath signals that arrive at the receiver in an underground mine compared to that observed in conventional surface environments and the manner in which it decreases with increasing transmitter-receiver separation and 2) to show that the antenna elements in MIMO antenna arrays used in underground environments must therefore be separated by several wavelengths (rather than the customary half-wavelength used in surface environments) in order to achieve acceptable performance. Further, the separation between the antennas must increase as the transmitter-receiver separation increases, higher order modes attenuate and, as a consequence, angular spread decreases. Other outcomes of this work include: 1) demonstration that the power azimuth spectrum (PAS) in underground mine environments can be modeled by a Gaussian distribution and 2) development of a novel technique based upon particle swarm optimization (PSO) for assessing and optimizing the performance of distributed-MIMO antenna systems in underground mine environments.

PREFACE

This thesis presents research conducted by Arghavan Emami-Forooshani under the supervision of Prof. David G. Michelson in the Radio Science Lab (RSL) at the University of British Columbia, Vancouver campus. Prof. Sima Noghanian (University of North Dakota) provided valuable technical suggestions and feedback during various stages of the thesis project.

A version of Chapter 2, "A survey on wireless propagation modeling in underground mines" has been accepted for publication in *IEEE Communications Surveys and Tutorials* [manuscript ID: COMST-00130-2012-R1]. Prof. Sima Noghanian read an early draft and provided valuable technical feedback. Shahzad Bashir suggested some revisions to the Introduction and Conclusions.

During the development of the MIMO channel sounder in Chapter 3, Robert D. White assisted with development of the data acquisition code.

A poster based on Chapter 4, "Effect of antenna configuration on performance of MIMO-based access points in a service tunnel" was presented at *IEEE APS/USNC-URSI 2012(Chicago, IL),* in Jul. 2012 and an abstract was published in the conference proceedings.

A version of Chapter 5, "Effect of antenna array properties on MIMO system performance in an underground mine," has been accepted for publication in *IET Microwave, Antennas and Propagation* [manuscript ID: MAP-2013-0102.R1]. Robert D. White participated in the MIMO measurement campaign in the underground mine.

For Chapter 6, Prof. Sima Noghanian provided valuable technical feedback throughout the project.

TABLE OF CONTENTS

LIST OF TABLES

LIST OF FIGURES

ABBREVIATIONS

AP	Access Point
AS	Angular Spread
BS	Base Station
BWc	Coherence Bandwidth
CAD	Computer Aided Design
CCDF	Complementary Cumulative Distribution Function
CDF	Cumulative Distribution Function
CDMA	Code Division Multiple Access
CIM	Cascade Impedance Method
CIR	Channel Impulse Response
C-MIMO	Collocated MIMO
CN	Condition Number
DAS	Distributed Antenna System
dBi	deciBel isotropic
D-MIMO	Distributed MIMO
DOA	Direction Of Arrival
DOD	Direction Of Departure
DS	Delay Spread
EM	Electromagnetic
FDTD	Finite Difference Time Domain
FM	Frequency Modulation
FSPL	Free Space Path Loss
GA	Genetic Algorithm
GO	Geometry Optics
GPIB	General Purpose Interface Bus
GSM-R	Global Systsem for Mobile communications - Railway
GTD	Geometrical Theory of Diffraction

HVAC	Heating, Ventilation and Air Conditioning
IEEE	Institute of Electrical and Electronics Engineers
i.i.d.	independent and identically distributed
ISI	Intersymbol Interference
ISM	Industrial, Scientific and Medical
LAN	Local Area Network
LF	Low Frequency
LOS	Line Of Sight
LTE	Long Term Evolution
MATLAB	MATrix LABoratory
MF	Medium Frequency
MIMO	Multiple-Input-Multiple-Output
MINER	Mine Improvement and New Emergency Response
NB	Narrow Band
NLOS	Non Line Of Sight
PAS	Power Azimuth Spectrum
PCS	Personal Communications Service
PDP	Power Delay profile
PEC	Perfect Electric Conductor
PED	Personal Emergency Device
PL	Path Loss
PLC	Programmable Logic Controller
PNA	Professional grade Network Analyzer
PSO	Particle Swarm Optimization
RF	Radio Frequency
RFID	Radio Frequency IDentification
RMS	Root Mean Square
RSL	Radio Science Lab
Rx	Receiver
SBR	Shooting Bouncing Ray
SCPI	Standard Commands for Programmable Instruments

SHF	Super High Frequency
SISO	Single-Input-Single-Output
SNR	Signal to Noise Ratio
SSM	Segmental Statistical Method
TE	Transverse Electric
TM	Transverse Magnetic
TL	Transmission Line
TOA	Time Of Arrival
TTA	Through The Air
TTE	Through The Earth
TTW	Through The Wire
Tx	Transmitter
UBC	University of British Columbia
UHF	Ultra High Frequency
UMTS	Universal Mobile Telecommunications System
ULA	Uniform Linear Array
UTD	Uniform Theory of Diffraction
UWB	Ultra Wide Band
VHF	Very High Frequency
VLF	Very Low Frequency
VNA	Vector Network Analyzer
WI	Wireless InSite
WiMAX	World wide interoperability for Microwave Access
WLAN	Wireless Local Area Network
WPAN	Wireless Personal Area Network

ACKNOWLEDGEMENTS

Pursuing my Ph.D. was one of the most precious experiences I have ever had in my life. This achievement would not have been possible without the help, support and inspiration of many people around me.

First of all, I would like to express my sincere appreciation and gratitude to my supervisor. I had the honour to work with Prof. David G. Michelson who is a successful, and well-known professor in both experimental and theoretical research. His valuable knowledge, experience, comments, and suggestions have improved different aspects of my PhD program. Throughout my PhD, he has been a great role model for conducting research, writing skills, and technical presentations. Many thanks to him.

My special thank to Prof. Sima Noghanian for her time and effort she devoted during my four-month visit to University of North Dakota under the Michael Smith Foreign Study Supplements Program (*i.e.*, CGS-MSFSS, granted by NSERC). I learnt a lot from our fruitful technical discussions.

Thanks to my kind colleagues Robert White, Pooyan Abouzar, Wadah Muneer, Shahzad Bashir, Carol Lee, James Chuang, Anthony Liou, and Kyle Sivertsen for their kind support and help for different research activities, particularly in conducting MIMO measurement campaigns in a service tunnel at UBC and in Myra Falls located in Vancouver Island, BC. It is a privilege to be surrounded by such kind people who are always available to help; I appreciate all of them.

I would like to thank National Sciences and Engineering Research Council of Canada (NSERC), Western Economic Diversification Canada (WD) and Modular Mining, and British Columbia Innovation Council (BCIC) for supporting my Ph.D. research through an NSERC Alexander Graham Bell Canada Graduate Scholarship, a Graduate Research Assistantship and a BCIC Innovation Scholars Award, respectively. Such support tremendously impacted my Ph.D. life. They brought me great inspiration and encouragement to continue challenging journey of Ph.D. program with strength and confidence. The equipment provided to our lab under grants from the Canadian Foundation for Innovation (CFI), WD and NSERC was essential to completion of the experimental portions of this work.

Finally, I would like to thank UBC Building Operations for providing us with access to the service tunnel underneath the Woodward Instructional Resources Centre and Nystar Mining for providing us with access to their Cu-Pb-Zn mine near Myra Falls on Vancouver Island for the purpose of collecting measurement data. Such access was also essential to completion of the experimental portions of this work.

To my dear parents, sister,

and to

all brave women and men who have sacrificed their lives and families to make the world a better place for others......

to

Rachel Corrie (peace activist)

Sattar Beheshti (blogger),

Nasrin Sotoodeh (human rights lawyer),

Bradley Manning (soldier),

....

CHAPTER 1: INTRODUCTION AND OVERVIEW

In 2008, the mining industry in British Columbia generated gross revenues of $8.4 billion (up from $6.9 billion in 2007) with net earnings of $3.2 billion (up from $ 1.2 billion in 2007). The mining industry in British Columbia directly employs some 7,600 people and indirectly employs another 21,000. The province is also home to several companies, including Modular Mining Systems Canada, Nautilus Automation and Wenco International Mining Systems, which provide mine communications and automation systems to clients around the world. Accordingly, methods for making underground mine communications more reliable and less expensive is of obvious strategic importance to the provincial economy [1].

In recent years, the underground mining community has begun to embrace short-range wireless communications technology as a key part of their strategy for enhancing the safety and productivity of their operations. Multiple-input-multiple-output (MIMO) antenna array technology has recently emerged as an important technology for boosting the capacity of wireless networks in conventional residential, commercial and industrial environments though exploitation of multipath propagation. However, wireless propagation in tunnels and underground mines is quite different from that in conventional surface environments. Here, we seek to assist those seeking to deploy MIMO-based wireless systems in underground mines by: 1) characterizing wireless propagation in straight sections of drifts or tunnels typical of those found in modern hard rock mines, 2) assessing the manner in which the configuration and placement of both conventional and distributed MIMO antenna arrays and transmitter-receiver separation affects the performance of such systems and 3) validating our results by employing alternative methods for characterizing wireless propagation (and MIMO-based wireless system performance) in underground environments.

1.1 Wireless in Underground Mines

1.1.1 **Legacy Systems**

Although early efforts to deploy wireless technology in underground mines and transportation tunnels date back to the 1920's [2],[3] much of this work was experimental and lacked theoretical support. Moreover, most early work was conducted at relatively low frequencies and achieved only limited success due to the extremely high path losses that were encountered [4]. In the late 1960's and early 1970's, safety concerns prompted government regulators and safety boards in both Europe and North America to encouraging the mining industry to improve communications with underground workers by deploying wireless systems based upon VHF-FM portable radios and leaky feeder distribution systems [3]. At VHF, wireless coverage in tunnels and drifts in underground mines and transportation tunnels is very poor because these structures function as waveguides operated below cutoff. Radiating coaxial cable, popularly known as leaky feeder, was developed during the 1950's and 60's in order to extend the coverage of VHF wireless communication systems to the relatively short underground transportation tunnels often found in major urban centres [5]. Underground mines presented a special challenge because they are typically far greater in extent, have much more complicated geometries, and evolve more rapidly over time than transportation tunnels.

Although leaky feeder based distribution systems have played an important role in underground wireless communications for almost four decades, their limitations in underground mining environments have become apparent in recent years. First, they are fixed infrastructure that is susceptible to damage from blasting if placed too close to the face, *i.e.*, the blind end of a drift or closed tunnel that protrudes into an ore body and the place where most of the activity in a mine takes place. That wireless coverage tends to be weakest where it is needed most is a serious limitation. Second, it is time consuming and expensive to deploy leaky feeder, reconfigure it, or extend it as the face is pushed forward into the ore body (at rates between 2 m and 10 m per day, depending on the mine type). Finally, currently deployed leaky feeder distribution systems are not compatible with recently developed wireless standards and technologies which offer much higher performance and greater capability, *e.g.*, integrated voice and data.

1.1.2 **Modern Systems**

Many of the limitations of VHF leaky feeder distribution systems can be avoided by moving to higher frequencies where signal attenuation is vastly reduced. Although commercial radios capable of operating at frequencies above 850 MHz have been available since the mid-1980's, interest in replacing existing leaky feeder distribution systems did not materialize immediately (Figure 1-1). By the late 1990's, growing interest in mine automation and tele-operation of mining equipment and the advent of standards-based digital wireless communication systems that operate above 800 MHz finally rendered leaky feeder distribution systems obsolete. Operating at higher frequencies eliminates the need for expensive leaky feeder cable infrastructure and maintenance, permits rapid redeployment and reconfiguration of the system as required, and allows effective wireless communication to be carried out at the face. The new systems also permit voice, data and video communications to be provisioned using a common infrastructure.

During the late 1990's and early 2000's, several mining companies, including Inco Ltd., evaluated the performance of various UHF wireless communications systems including 1.8 GHz PCS CDMA cellular and ISM 915 and ISM 2450 Wireless LAN in underground mine environments. The mining industry has recently started investing in future-oriented technologies such as machine-to-machine (M2M) solutions, offering a high degree of optimization potential in deeper underground mines. This requires a solid wireless communication platform to simultaneously handle various services and devices such as, hand-held devices, remotely-controlled machines, cameras, dispatches, RFIDs, toxic gas-detectors, thermal, humidity, and geological sensors, *etc.*

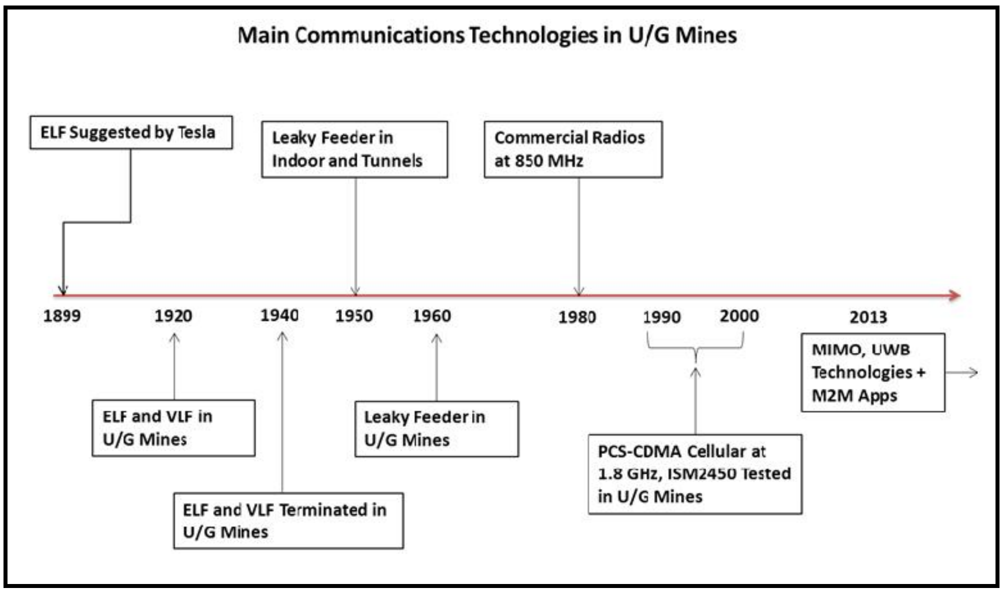

Figure 1-1 Technology push into mining underground mines over time.

Among different standardized products, IEEE 802.11-based wireless LAN-based systems that operate in the ISM 2450 band have attracted the most interest because they offer an effective combination of economy and flexibility in deployment and configuration. However, performance of such systems is uncertain because most of them are based on multiple-antenna systems which have not been studied for applications in underground mines. While performance degradation due to channel impairments is troublesome when users are accessing voice or information services, it can be intolerable in mine automation or tele-operation applications where response times are critical. As a result, MIMO-based wireless systems, well known for offering high performance in conventional environments, need to be modeled and carefully designed in underground mines.

1.2 Characterization of MIMO-Based Systems

In this section, we recall two key parameters of MIMO systems: the first one is channel capacity in bit/sec/Hz, a performance parameter, while the second one is angular spread, an environmental parameter.

1.2.1 MIMO Channel Capacity

Scattering by objects in the environment leads to multiple transmission paths between the transmitter and receiver. While this raises the possibility of increasing link capacity by utilizing each path as an independent channel, such paths are often so closely spaced in angle that one cannot distinguish between them using simple beamforming. A more sophisticated approach is to use space-time coding to distribute the data stream over the N_{Tx} transmitting antennas and recover the stream by suitably combining the signals received by the N_{Rx} receiving antennas. The resulting multiplexing or capacity gain, is achieved without requiring either additional power or additional bandwidth [6].

Capacity, which is a fundamental property of a MIMO-based system, may be predicted as follows. First, consider a wireless communications system that uses only one transmission path to send data. Shannon's Law gives the maximum capacity C_1 of the link in bit/s/Hz as:

$$C_1 = \log_2 \left(1 + {}^\circ \right) \tag{1}$$

where ρ is the signal-to-noise ratio (SNR) at the receiver input. The capacity C (in bit/s/Hz) of a MIMO-based system with N_{Tx} transmitting antennas and N_{Rx} receiving antennas is given by [6]:

$$C = \log_2 \left[\det \left(I_{N_{Rx}} + \frac{SNR}{N_{Tx}} H_{nor} H_{nor}^{*} \right) \right] \quad \text{b/sec/Hz} \qquad (2)$$

where $*$ denotes the transpose-conjugate, H is the $N_{Rx} \times N_{Tx}$ channel matrix and we have assumed that the N_{Tx} sources have equal power and are uncorrelated.

In a rich multipath environment where signal fading observed by individual receiving antennas is uncorrelated, the channel matrix has full-rank and the increase in capacity is proportional to the minimum of the number of transmitting and receiving antennas. Because the multiple transmission paths fade independently of each other in such cases, this approach also increases overall link reliability. If the subchannels are highly correlated then the channel matrix will be rank deficient and hence no capacity gain is achievable. This may occur when the angular spread of incoming signals at the receiver is very low. It is apparent that full appreciation of the strengths and limitations of alternative MIMO schemes requires that their performance be assessed [7].

1.2.2 **Angular Spread**

The main focus of characterization of single-input single-output (SISO) systems is the pathloss and delay spread. For characterization of MIMO channels, however, the spatial domain becomes equally important as the temporal domain. Similar to power-delay-profile (PDP), power-azimuth-spectrum (PAS) has been defined, which determines the spatial distribution of the received power over the azimuth domain. Consequently, angular-spread

(AS) is defined as the standard deviation of PAS, being equivalent to the root-mean-square (RMS) delay-spread of PDP [8]. AS is found to govern many properties of MIMO-based system metrics, *e.g.*, singular value and capacity distributions [9]. In addition, parameter that characterizes space selective fading is the coherence-distance (D_C) that is inversely proportional to the AS. The D_C is the spatial separation for which the autocorrelation coefficient of the spatial fading drops to 0.7 [10].

In conventional indoor and macrocell environments, the PAS at the mobile unit tends to be broad so fading on adjacent antenna elements tends to be uncorrelated for relatively small element separations (smaller D_C). Linear confined spaces such as tunnels and drifts in underground mines tend to function as overmoded waveguides at radio frequencies. As a result, the PAS in such environments is expected to be considerably narrower than in conventional environments and the performance of MIMO wireless systems, is likely to be reduced. However, no experimental or theoretical study has been performed to predict or estimate angle-of-arrival distribution.

Consequently, we decided to theoretically study angular properties of the tunnels. Several theoretical approaches, such as single-mode waveguide model and geometrical-optical models (*i.e.*, are explained in great detail in Chapter 2) [11]-[16] were developed to predict propagation in underground tunnels at UHF and above during the 1970’s. For our study, we chose multimode waveguide model which has been recently developed. This model is the advanced version of the single-mode waveguide model and is able to accurately model both near-field and far-field of tunnels.

1.3 Previous Efforts to Design Antenna Configuration in Indoor Environments

Considering different antenna properties, such as radiation pattern, polarization and array configuration and spacing (in case of MIMO systems) introduces the flexibility in an effective design of communication systems. Here, the main antenna properties that are taken into account in system designs and deployments for indoor areas are discussed.

1.3.1 Antenna Radiation Pattern

For antenna design and deployment of SISO systems in outdoor and indoor environments, the main focus is coverage and interference. Antenna radiation pattern (omni-directional or directional) plays a key role in coverage and interference. Use of directional antenna is well-established for outdoor and indoor environments to increase coverage and reduce interference [17]. However, the disadvantage is that the performance of directional antenna is highly dependent on the antenna orientation while optimal orientation itself is dependent on the layout of the environment and propagation scenario [17], [18].

In [17], the performance of omni-directional discone and directional patch antennas was compared in the presence of internal obstacles and external interference in an indoor environment. The general suggestion of this study is to illuminate distinct regions of the floor area and away from each other with different directional APs. This guarantees sufficiently high signal reception across the entire area while minimizing the mutual interference between APs and mitigating external interference, which leads to improvement in overall system performance. However, signal coverage is compromised by this improvement and thus additional APs may be required at the expense of increased deployment complexity.

1.3.2 **Antenna Polarization**

Unlike outdoor environments where different antenna polarizations perform quite differently (mainly due to the ground effect), in conventional indoor environments, such as offices and labs they behave similarly. However, in hallways the results are a bit different. Researchers at Stanford University have conducted narrowband measurements at 1.95 GHz in a hallway (LOS paths) with laboratories (NLOS paths) on both sides of the hallway [19],[20]. The Tx was located in one end of the hallway and Rx was moved along the hallway and inside the labs. They showed that horizontally polarized waves attenuate more quickly than vertically polarized waves in the hallway but they both attenuate at about the same rate in the labs. It has been attributed to the Brewster angle phenomena which happen in interaction of horizontally polarized waves with dielectric sidewalls (which unlike conductive floor and ceiling behave differently for different polarizations).

The effect of antenna polarization has been studied for SISO systems in tunnels too. The main result of the studies is that in empty tunnels with horizontal aspect ratio (*i.e.*, width is larger than height), attenuation of the horizontal polarization is lower. However, their performance for MIMO systems and in presence of infrastructure is uncertain and needs to be studied.

1.3.3 **Antenna Array Configuration and Spacing**

In MIMO systems, in addition to coverage and interference, the correlation among antenna elements is also important. This correlation is also influenced by antenna properties, such as interelement spacing, array orientation, antenna radiation pattern, and polarization as well as angular spread of the wireless channel. Because conventional indoor environments such as offices are often rich in terms of scattering, angular spread is sufficiently large. Therefore, different array configurations, such as UCA and ULA with both polarizations show suitable performance. For indoor offices, λ/2 interelement separation between neighboring antenna elements show sufficient level of decorrelation between antenna elements, however, in hallways the spacing should be larger than λ [19],[20].

Figure 1-2 Different types of MIMO antenna configurations, such as ULA and UCA for indoor environments.

A research group at the University of Lille in France has conducted several studies of 4×4-MIMO wireless channels in transportation tunnels used for railways, roadways and/or subways [21]-[24]. These studies have focused on the 900 MHz band for GSM-R (a variant of GSM designed for use by high speed railways) applications. Several ULA orientations were compared. The Tx antennas were fixed and placed on the station platform with following array orientations: 1) parallel to the tunnel axis, 2) diagonal (along a line at an angle of 30^o from the centreline), and 3) perpendicular to the tunnel axis. Due to safety and clearance issues, mobile antennas cannot be installed on the train roof, therefore, the mobile Rx was installed on the train's windshield. In order to have sufficient degree of fading decorrelation among MIMO antennas, antenna spacing at Tx was more than 3λ and1.4λ at

Rx. Based on this study, the MIMO performance found to be significantly sensitive to the Tx array orientation, which is due to the low AS caused by the waveguide effect inside the tunnel. The best performing orientations were diagonal and the one aligned perpendicular to the tunnel axis.

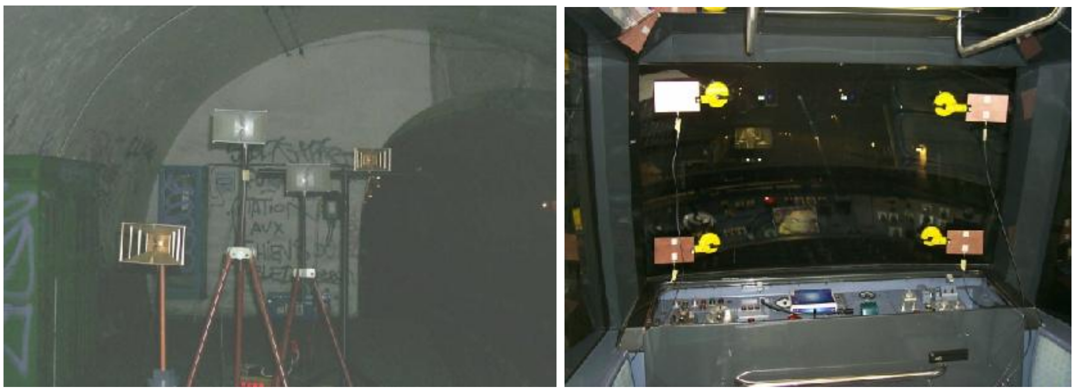

Figure 1-3 Fixed Tx ULA placed on the platform, Mobile Rx ULA installed on the train windshield [21].

1.4 Implications for MIMO Antenna Configuration Design and Deployment in Underground Mines

While previous studies of MIMO modeling and configuration design in other confined spaces have yielded useful insights, they cannot replace studies conducted in underground mines. As a result, mine communication engineers have had little to guide them as they seek to design and deploy MIMO-based wireless systems underground. Compared to transportation tunnels (the most similar to mine tunnels), underground mine tunnels and galleries are considerably narrower which may lead to higher modal cut off frequencies and lower angular spread that will limit MIMO performance. In addition, mine tunnels have branches, considerably rougher walls, and irregular geometry, which cause much more diffuse scatter. As a result, further study is required in order to assess the relative magnitude of these effects and to determine the MIMO performance that can be achieved.

1.5 Objectives of This Work

We have sought to contribute to the safe and efficient operation of underground mines and transportation systems and overcome the limitations of past work by: 1) developing a MIMO measurement system to experimentally assess the MIMO performance for various deployment scenarios in underground mine environments, 2) using three complementary modelling and prediction tools: i) field measurements using a custom-designed channel sounder in both a building service tunnel at the University of British Columbia and an underground lead-zinc mine at Myra Falls, BC, ii) simulations based upon ray-tracing and iii) theoretical models based upon waveguide mode expansion to assess and compare strategies for effective configuration and deployment of MIMO antennas in underground mines, 3) experimentally validating a theoretical model for tunnels (multimode waveguide model), which has not been validated for short mine tunnels, 4) characterizing angular-spread and MIMO channel capacity based on this theoretical model and 5) developing techniques to assess and optimize the performance of distributed MIMO systems based on the multimode waveguide model.

1.6 Organization of the Thesis

The organization of the thesis is as follows: In Chapter 2, we present a comprehensive literature survey on wireless developments and propagation modeling in underground mines from 1920-2012 is presented. In Chapter 3, we describe our MIMO measurement setup and data acquisition software. In Chapter 4, we present and compare the results of MIMO simulations and measurement campaign conducted in a service tunnel at UBC. In Chapter 5, we present the results of a MIMO measurement campaign performed in the underground Cu-Pb-Zn mine at Myra Falls, BC operated by Nystar Mining. In Chapter 6, we present the results of characterizing MIMO wireless channels in an underground mine using a multimode waveguide model. In Chapter 7, we present a novel method for optimizing the placement of distributed MIMO antenna elements in underground mines using multimode waveguide modelling and particle swarm optimization. Finally, in Chapter 8, we present the conclusions of this study and suggest possible next steps.

CHAPTER 2: A SURVEY OF WIRELESS COMMUNICATIONS AND PROPAGATION MODELING IN UNDERGROUND MINES

2.1 Introduction

The mining industry plays a vital role in the global economy. The current estimated market capitalization of global mining companies is about $962 billion [25],[26]. A large portion of these operations are underground and involve specialized equipment and processes. Communication systems play an increasingly important role in ensuring personnel safety and optimizing the mining process. The estimated size of underground mining equipment market alone is currently about $45 billion [27], a small but important portion of which is allocated communications systems.

Although interest in deploying wireless communication systems in underground mines dates back to the 1920's [28],[29] the first wide deployment didn’t take place until the early 1970's when the mining industry began to deploy very-high-frequency (VHF) radios and leaky feeder distribution systems [30]-[34]. The modern era of underground communications began in the early 2000's as the mining industry sought to take advantage of considerable advances in ultra-high-frequency (UHF) technology, especially cellular phones, wireless-local-area-network (WLAN), UWB and radio-frequency-identification (RFID). Although the mining industry is generally conservative and reluctant to invest in costly new technologies, high profile accidents often prompted regulators to require that the mining (and mining communications) industry devote increasing attention to safety and safety communications [35]. Recent interest in deploying next generation wireless communications technology in underground mines has stemmed from: (1) recent advances in short-range wireless communications technology and commercial-off-the-shelf WLAN, wireless-personal-area-network (WPAN), UWB, RFID, radar devices, and (2) the potential to increase mine efficiency and productivity through more effective voice communications, better access to management information systems and automated dispatch [36],[37].

In an underground mine, there are three possible mechanisms for communication signaling: through-the-earth (TTE) at extremely-low-frequency (ELF)/very-low-frequency (VLF)/low-frequency (LF) bands, through-the-wire (TTW) at medium-frequency (MF)/VHF/lower-UHF (*e.g.*, leaky feeders) and through-the-air (TTA) at upper-UHF/super-high-frequency (SHF) [38]. Each has been developed for different applications and each requires specified propagation channel modeling and design. Most of the recent wireless systems fall under the TTA category and also seem to be promising wireless technology for future applications. Accordingly, the main focus of this survey is on methods for characterization of the TTA wireless channels at UHF-band; TTE and TTW are only briefly considered.

The need to understand and characterize wireless channels has been recognized since the earliest days of wireless communications. The objective of channel characterization or modeling is to capture understanding of the manner in which the propagation environment impairs and distorts wireless signals in a form useful in the design, test and simulation of wireless systems. Subway tunnels lack the rough and tilted walls that characterize underground mines. However, because their propagation characteristics show some similarities to those of underground mines, they have been considered here as well.

For decades, researchers have recognized and studied the differences between wireless propagation in tunnels and underground mines and surface environments. Valuable theoretical and experimental contributions have been made by several groups including J. Wait *et al*., S. F. Mahmoud, A. E. Goddard *et al.*, A. G. Emslie *et al*., P. Delogne, Y. P. Zhang *et al*., M. Lienard *et al*., and C. Despins *et al*. Two non-recent reviews, one from 1978 [31] and one from 1991 [34], are about early stage wired/wireless communication technologies such as different types of phones, pagers, leaky feeders and TTE communications. In 2009, the Canada Center for Mineral and Energy Technology (CANMET) reviewed the current state of wireless communications technology for underground mines including products manufactured by key suppliers, their specifications, limitations and advantages [39]. Products by key companies, such as Becker Mining Systems, Mine Radio Systems, MineSite Technology, MineCom, Tunnel Radio of America and Varis, are evaluated in this study. In addition, for documents involving safety and permissible designs for electronic communications systems, the National Institute for Occupational Safety and Health (NIOSH) has provided online resources such as collections of past and current mine communications publications, tutorials and workshops [40]. In another recent survey [41], both past and current communication systems in wired/wireless forms are introduced and the significance of each is briefly discussed.

Despite of all of this past effort, there is no comprehensive survey to date of underground communications that not only introduces the technologies and their significance but also reviews the propagation channel models developed for underground tunnels and mines. This can be a barrier for those who want to enter into this field or would like to know more about the subject matter.

In this chapter, we aim to present a comprehensive survey of wireless propagation in tunnels and underground mines with a focus on current wireless channel modeling, technologies and applications. Our objective is to put previous work in perspective, identify trends and gaps, and summarize accomplishments and opportunities. In Sec. 2, we begin the survey with a brief review of the basic wireless propagation terminology. In Sec. 3, we present a brief history of wireless communications in underground environments. In Sec. 4, we show how the related numerical and analytical models have evolved over time. In Sec. 5, we consider measurement-based models. In Sec. 6, we summarize the practical implications for wireless system design based on significant contributions of several researchers. Finally, in Sec. 7, we present the conclusions of this chapter.

2.2 Wireless Propagation Terminology

In this section, some technical terms that will be required throughout the dissertation are addressed and explained. These terms will be described by explaining how a transmit signal undergoes pathloss and fading before reaching a receiver. Most of material presented here has been extracted from a comprehensive survey on propagation models for mobile communications in [42] as well as a book chapter [43].

As a wireless signal traverses the path from a transmitter to a receiver, it experiences different propagation phenomena such as *reflection*, *diffraction*, *scattering* and *refraction* (Figure 2-1). Reflection occurs when the electromagnetic (EM) wave is incident upon a smooth surface, whose dimensions are large compared with the signal wavelength.

Diffraction is a propagation scenario in which an object whose dimension is larger than the signal wavelength and which has sharp edges obstructs a path between transmitter and receiver and causes new secondary waves to be generated. Scattering occurs when incoming signal is incident upon an object whose size is of the order of the wavelength of the signal or less. Refraction is the change in direction of a wave due to a change in its velocity while traveling between media with different refractive indexes.

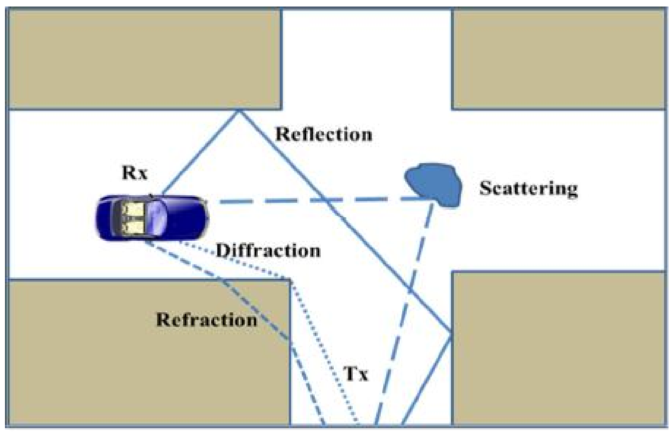

Figure 2-1 Wireless propagation phenomena

As a result of interaction of signal with the surrounding area, replicas of the signal may take multiple paths from the transmitter to the receiver. Because the replicas reach the receiver after different delays, the signal experiences *time dispersion* (quantified by delay spread) and because they also arrive from different directions, the signal experiences *angular dispersion* (quantified by angular spread) [43]. If either the scatterers or one of the terminals (Tx or Rx) moves, rapid changes in the phase relationship between multipath components can cause the signal to fade randomly, *i.e.*, *fading*. Such variation in received signal strength over time is equivalent to *frequency dispersion* (quantified by Doppler spread). Fading can be categorized into two main types: *small-scale fading* and *large-scale fading* which are shown in Figure 2-2.

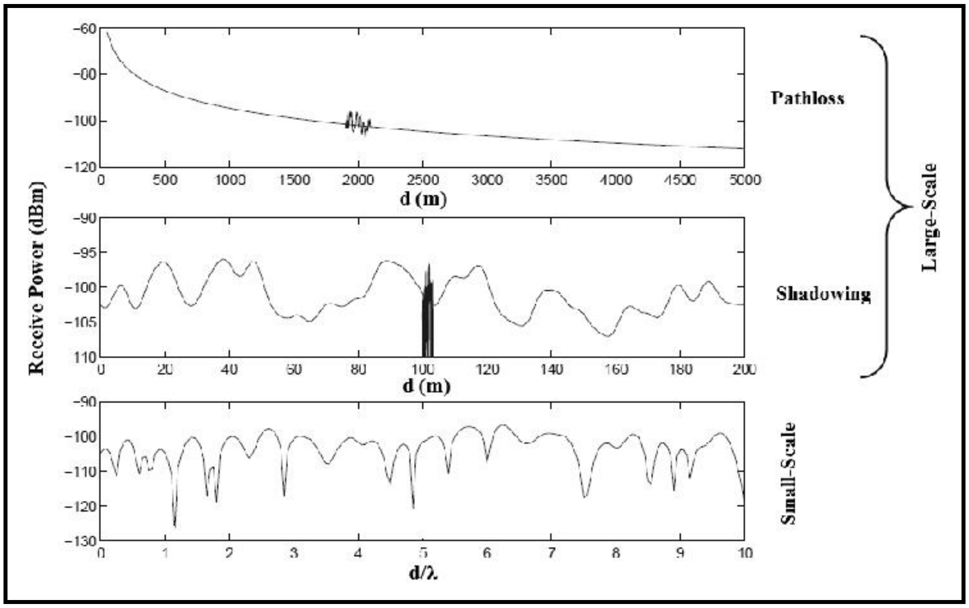

Figure 2-2 Large-scale and small-scale fadings

Small-scale fading is due to small changes in position (as small as half wavelength) or to changes in the environment (surrounding objects, people crossing the line of sight between transmitter and receiver, opening or closing of doors, *etc*.). Small-scale fading models, therefore characterize the rapid fluctuations of the receiver signal strength over very short travel distances (few wavelengths).

Large-scale fading is due to motion in a large area, and can be characterized by the distance between transmitter and receiver. Large-scale fading models therefore predict the mean signal strength for an arbitrary transmitter-receiver (Tx-Rx) distance are useful for estimating the radio coverage. *Pathloss* and *pathloss exponent* (or distance exponent, power-distance-factor) are terms used in large-scale models for indoor and outdoor environment.

Pathloss, the most fundamental measure of channel quality, is the attenuation of the transmitted signal as it propagates. In decibels, pathloss, *PL* is defined as:

$$PL = P_{Tx} + G_{Tx} + G_{Rx} - P_{Rx} \tag{1}$$

where P_{Tx} and P_{Rx} are the time-averaged power levels (in dBm) at the output of the Tx and the input of the Rx, respectively, and G_{Tx} and G_{Rx} are the gains (in dBi) of the transmitting and receiving antennas. The relationship between pathloss and the distance, *d*, between the Tx and Rx follows a power-law relation and can be described by [43]:

$$PL(d) = PL_0 + n10\log_{10}\frac{d}{d_0} + X_{\pm} \tag{2}$$

where P_{L0} is the value of pathloss (in dB) at the reference distance d_0, *n* is the distance exponent and X_σ is a zero-mean Gaussian random variable with standard deviation *σ*. The random variable *X* accounts for the location variability or shadow fading that is generally attributed to differences in the degree to which the path is obstructed at different points throughout the coverage area.

The pathloss exponent is a measure that yields to what power of separation the signal power in the profile decays. It can be determined by applying regression analysis to the large fading component of a received signal data file. It is in the range of 2 (for free space) to 4 (for the case of specular reflection from the ground surface). In some environments, such as buildings and other indoor environments, the pathloss exponent can reach values in the range of 4 to 6. On the other hand, a hallway or a tunnel may act as a waveguide, resulting in a pathloss exponent less than 2. Most of pathloss models have one or several *breakpoints* which distinguish areas where radio wave experiences different pathloss exponents (Figure 2-3).

As an example, two-ray model (or flat-earth model) which accounts for the specular reflection from the earth surface has one breakpoint. Before that pathloss exponent is 2 and after that due to contribution of the reflected ray from the ground, pathloss exponent changes to 4.

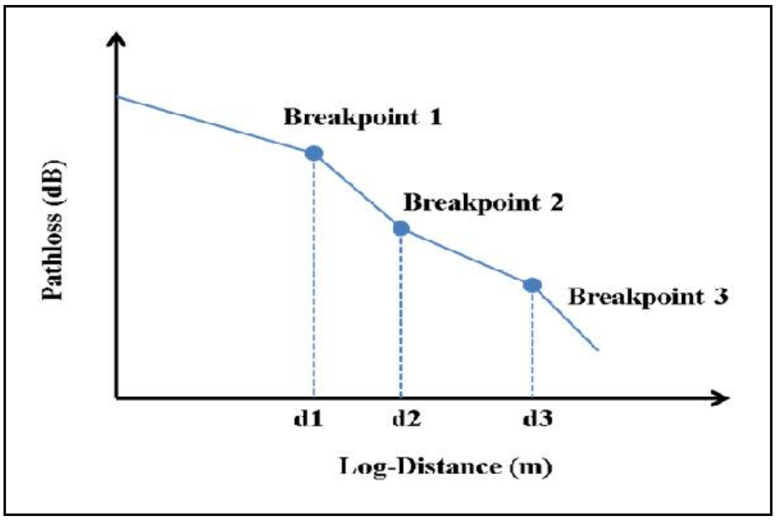

Figure 2-3 A pathloss model with three breakpoints

Tunnel pathloss model has also a breakpoint which separates *far-field* (or far zone) and *near-field* (or near zone) regions. The breakpoint location in a tunnel depends on the largest cross-sectional dimension (width or height) of the tunnel relative to the signal wavelength. It should be noted that far-field and near-field definitions for propagation models in tunnels are not the same as far-field and near-field of an antenna.

The near-field region of a straight tunnel is the region before the breakpoint where signal fluctuation is significant because of the reflections and multipath components coming from different directions, which are comparable to the line-of-sight path. In this region, the pathloss exponent is closer to that of indoor environment ($n \geq 2$). On the other hand, the far-field region of a straight tunnel is the region after the breakpoint where all the paths are received at the Rx from almost the same angle as the direct path, and therefore the received signal is well established and the fluctuation of the signal is not significant. In this region, pathloss exponent is less than that of free space pathloss, *i.e.*, n=2, and so-called *waveguide propagation* occurs.

The *attenuation constant* describes the attenuation of an EM wave propagating through a dielectric medium per unit distance from the source. It is the real part of the propagation constant, measured in Nepers per metre (*Np/m*) and accounts for attenuation due to propagation in a lossy environment. Attenuation constant of vacuum equals to zero because it is a lossless medium. Assuming a transverse-EM (TEM, *i.e.*, E and H are both perpendicular to direction of propagation) plane wave propagating in the z direction can be represented using the phasor expression:

$$E(z,\omega) = E_0 e^{-\gamma z} \tag{3}$$

where ω is the radian frequency and γ is the complex propagation constant given as:

$$\gamma(\omega) = \alpha(\omega) + j\beta(\omega) \tag{4}$$

where α (*Np /m*) is the attenuation constant and β (*rad /m*) denotes the phase constant.

2.3 The Evolution of Wireless Communications in Tunnels and Underground Mines

In this section, the evolution of wireless communications in underground mines is discussed in terms of technologies and applications. Both reveal that the initial motivation for underground mine communications was to increase the safety of miners by implementing man-to-man communications. As underground mine communications have evolved, man-tomachine and machine-to-machine communications have been implemented to meet efficiency and productivity objectives.

2.3.1 Through-The-Earth Communications

Interest in wireless communications for underground mine dates back to the 1920's when the earliest pioneers of radio were interested in the possibilities of TTE wireless transmission. N. Tesla suggested to use ELF signals, and the earth as a transmitting medium to send messages across the world in 1899 [44]. This continued until the late 1940's when techniques such as carrier-current radios and TTE signalling were commercially offered by the U.S. Bureau of Mines for ordinary communications and for emergency operations in mines [28],[29],[34]. TTE communications in mines use huge antennas to transfer ELF or VLF signals through solid rock from the surface into the underground mine. In late 1940's, due to limitations such as low data rate and bulky mobile equipment, early studies of wireless communications in tunnels were terminated [45],[46].

Recent mine regulations have renewed interest in TTE communications because it offers a wider coverage inside the mine compared to modern wireless systems. There are apparent advantages to modern wireless systems in underground tunnels and mines, but they could be quite vulnerable when a major disaster occurs. Disasters such as explosion, flooding, rock burst, or severe roof fall, may damage the relay system or block airways. TTE communications has been proven to be suitable for emergency communications because it accesses every part of the mine by propagating through the rock and requires no cabling between the surface and underground [47]. Two-way communication systems are preferred over one-way systems because in most emergency cases, it is essential for escaping or trapped miners to relay valuable information to the surface.

Until several fatal incidents occurred in the United States in 2006, the number of mining disasters had been following a decreasing trend. The Mine Improvement and New Emergency Response (MINER) Act of 2006 requires that mine operators install wireless two-way communications and tracking systems that will connect surface rescuers to the underground workers [48]. Two commonly used wireless solutions for emergency cases are text messaging based on TTE and tracker tagging.

Personal-emergency-device (PED) is an emergency warning system based on TTE technology [49], which uses VLF/ULF signals to transmit text messages (Figure 2-4). Initially, this product had one-way communication capability, but recent versions are capable of two-way communication via text messaging [49].

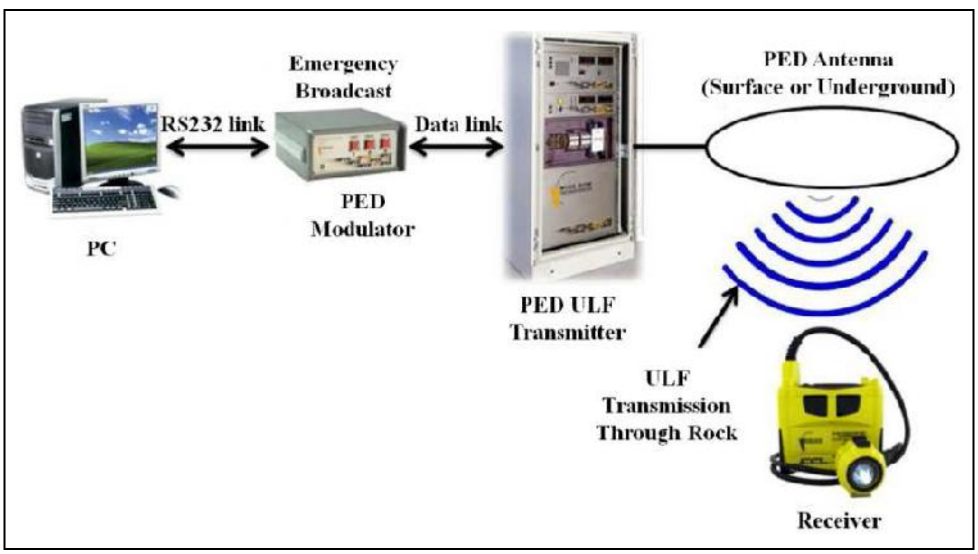

Figure 2-4 Through-the-earth communications

2.3.2 **Through-The-Wire Communications**

In the early history of through-the-wire communications in tunnels and underground mines, implementation of communication systems was based on experimental observations without any theoretical insights or empirical modeling attempts. People working in underground mines found that low frequencies on the order of 10 MHz (cutoff frequency of fundamental modes of most tunnels) could cover distances of less than 30 m in an empty mine [12]. However, they also observed that conductors such as electrical cables, pipes and *etc*., running in most mines, enhance EM propagation with low attenuation, and therefore increase the range [44]. This fact was not immediately understood by experimenters, but it resulted in development of monofilar technique at the end of 1960's. Monofilar system became an introduction for leaky feeder systems which were widely used thereafter.

In general, TTW signals can travel over coaxial, twisted pair, trolley, leaky feeder, and fibre optics from the surface or inside the mine and reach the mobile equipment. Because one side of the system is wired and the other is wireless, it is also called a hybrid or semi-wireless system. During the 1950's and 1960's, leaky feeder systems and other distributed antenna systems were developed in order to extend the coverage of VHF wireless communication systems to the relatively short underground transportation tunnels often found in major urban centres and for providing public safety [33]. In the late 1960's when the safety concerns prompted government regulators and safety boards in both Europe and North America to encourage the mining industry to improve communications with underground workers by deploying wireless systems based upon VHF-FM portable radios and leaky feeder distribution systems [34]. Leaky feeder is the most well-known TTW-based communication system in underground mines. The cable is called 'leaky' as it has gaps or slots in its outer sheath, allowing signal to leak into or out of the cable along its entire length (Figure 2-5). Because of this leakage of signal, line amplifiers must be inserted at regular intervals, typically every 350 to 500 metres. Key disadvantages of leaky feeder system are difficult maintenance, fixed infrastructure, limited capacity and low coverage near the face, *i.e.*, the region of the mine where ore is extracted [34].

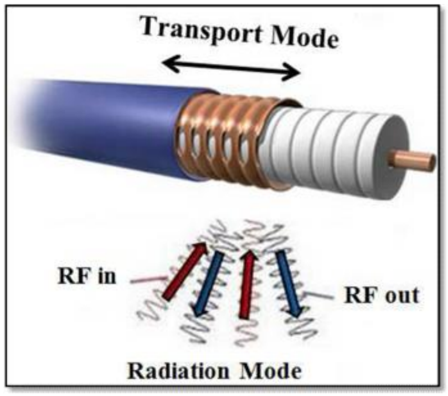

Figure 2-5 Leaky feeder cable

2.3.3 Through-The-Air Communications

TTA is another wireless system for communications in underground mines. It is capable of offering various applications such as two-way voice and data communications, tracking miners and equipment, remote control and sensing, video surveillance and *etc.*

In early 2000's, advances in short-range digital communications to cover hundreds of metres motivated the mining industry to consider WLAN off-the-shelf products to support short-range applications in underground. In the late 2000's, the mining industry was attracted to low data rate technologies such as ZigBee, active-RFID (tens of metres), passive-RFID (about a metre) and high data rate systems, such as UWB systems, because they offer short-range, low power and positioning capabilities. These technologies can support various applications such as dispatch and sensor networks. These applications can be implemented based on WLAN backbone. So far, WLAN mesh networks which are redundant, self-learning and self-healing seems to be the most reliable wireless systems. If any part of the network is destroyed, the remainder continues to function, and therefore it is especially desirable in a dynamic environment where link failures are frequent as in the mine galleries [37],[49]. One of the attractive wireless applications is tracking which can be implemented based on RFID technology using WLAN, fibre optics or leaky feeder backbone (Figure 2-6). This tracking system provides the ability of real-time monitoring the location of personnel, vehicles and equipment underground. Mining equipment such as vehicles, containers, drills and other valuable mobile ore production equipment are constantly moving through large underground areas. Because the equipment does not necessarily follow a pre-defined track and is spread throughout the mine, it is difficult to locate particular assets that are needed in real-time [50],[51].

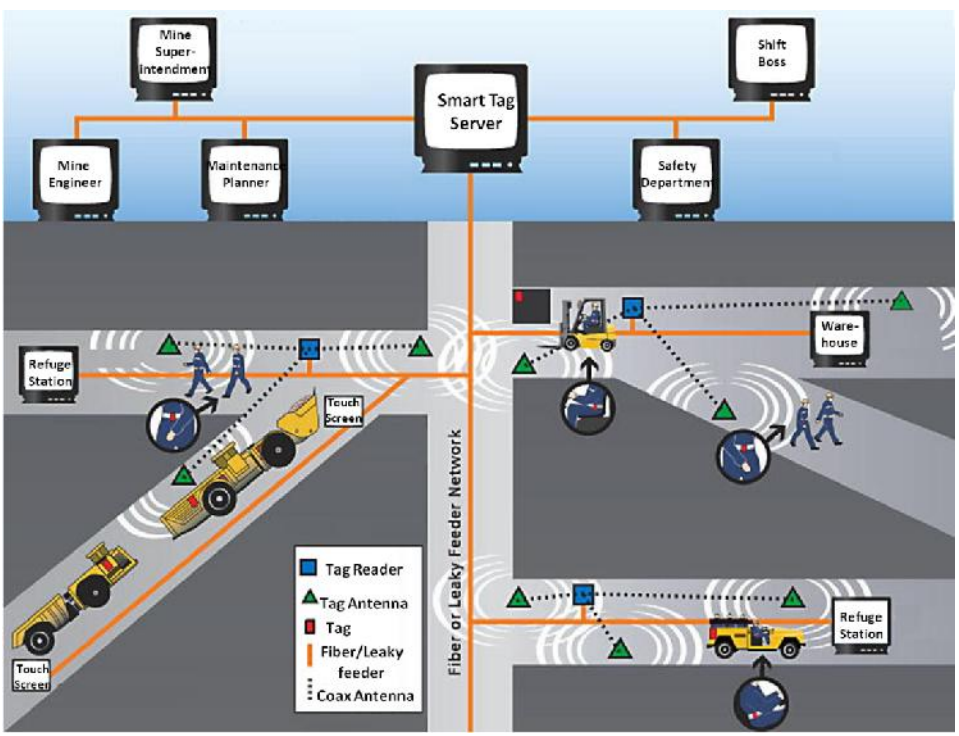

Figure 2-6 Tracking system in an underground mine [52].

A typical RFID-based tracker system is shown in Figure 2-6. This system consists of: (1) active tags to identify personnel/vehicles/assets or store data and histories, (2) tag readers to exchange information with the server and tags, (3) antennas to connect tags and tag readers and provide triangulation information for location finding, (4) a server computer system for control and monitoring, and (5) backbone system which can be fibre optics or leaky feeder to connect tag readers to the server [52].

Another important application of short-range wireless is remote control and sensing. Some of commonly deployed control applications of wireless communication are real-time remote equipment diagnostics, remote monitoring, remote programmable-logic-controller (PLC) programming, *etc*. As an example, a PLC in local control station can wirelessly communicate with the remote automation and sensor devices (such as pull cords, belt misalignments and tilt switches or motion sensors) along a conveyor in a mine site.

Before employing the aforementioned wireless technologies in tunnels and underground mines, careful characterization of the wireless propagation in terms of parameters such as pathloss, delay spread and angular spread, *etc*. is required. This is because wireless propagation in tunnels and underground mines is significantly different from conventional indoor and outdoor environments, and therefore existing channel models developed for conventional surface environments are not applicable. Consequently, it will be necessary to develop new channel models that capture the nature of the relevant impairments and their dependence on the new environment.

A good channel model is abstract, simple, and focuses on those aspects of the channel that affect the performance of a system of interest and ignore the rest. Over-engineering the communications links is needlessly expensive and under-engineering them leads to either insufficient reliability or capacity. Propagation and channel modeling facilitates efficient design and system deployment by answering questions such as “What channel impairments do we need to mitigate? or “What is the optimum frequency, antenna placement/configuration and range?”

2.4 Propagation Analysis and Modeling

In this section, we focus on the different mechanisms by which wireless signals propagate in underground environments. First, TTE (through the earth) and TTW (through the wire) propagation will be briefly explained. Then, as the main focus of this survey is TTA (through the air) communications, we will elaborate more on analytical modeling for this method. As it will be seen, TTE method is similar to geophysical probing, TTW method can be analyzed similar to transmission lines and TTA in underground tunnels can be considered as waveguide propagation.

2.4.1 Propagation Through-The-Earth

In TTE underground communications, the antenna and propagation mechanism are similar to subsurface communications and geophysical probing of the Earth. Both applications require transmission of electromagnetic waves through the earth, and both face the problem of high attenuation. To penetrate the earth to depths of 100 m or more, it is necessary to employ low frequencies (ELF, VLF) [53]. For TTE communications, an extensive loop antenna or a ferrite rod antenna on the order of few kilometers is often used to send/receive the magnetic waves through the rocks (Figure 2-7). The choice of magnetic fields for TTE communications might be due to the fact that the earth attenuates and changes the magnetic fields less than the electric fields. The antenna is deployed either on the surface or underground to communicate with miners under the ground [38]. Broader coverage is achievable by increasing the size of the antenna. Power for the underground transmitter is limited due to permissibility requirements. In this type of communications frequency, geology, noise and depth will influence the probability of successfully communicating with the surface using TTE communications[38].

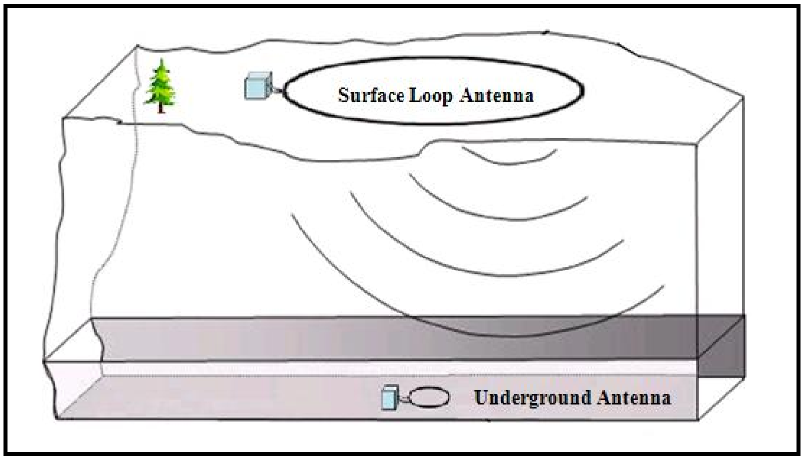

Figure 2-7 Surface antenna for through-the-earth communications.

Based on initial studies, conductivity of the earth's layers was found to be important in VLF ranges. Studies showed the presence of any metallic conductor such as pipes, power cables, rails, *etc*. greatly enhances the transmission of radio waves TTE. Conductivity proved to be a function of the types of rock or soil through which a signal passed as well as a function of the signal frequency [44]. The effect of rock layers on the EM propagation was extensively studied by J. Wait *et al*. [54].Their work underlies later studies on TTE EM probing or signaling. They have addressed continuous-wave and transient problems over a range of conductivity and dielectric values.

Numerous studies of EM noise were also carried out after it was realized that at VLF or ELF ambient noise is a major problem. The source of the background noise was determined to come from the interaction of particles of solar origin with the earth's electric and magnetic fields and from worldwide lightning [45]. References concerned with the problem of EM propagation through-the-earth and other significant accomplishments by J. Wait *et al*. are listed in [54]. Currently, TTE signaling is used for emergency communications in underground mines. Portable, person-worn wireless TTE systems exist and are often used instead of hard-wired systems to establish contact with miners because they offer better resistance to damage from roof falls, fires and explosions.

2.4.2 **Propagation Through-The-Wire**

For propagation through-the-wire, frequency bands higher than ELF were used by stretching a longitudinal conductor along the tunnel. Such a conductor could support a quasi-TEM mode spread between the conductor and the tunnel sidewall (Figure 2-8a), referred to as the 'monofilar' mode and characterized by a zero cutoff frequency. The fields of such a mode are accessible in the whole cross-section of the tunnel at the expense of power loss due to high power absorption by the tunnel wall. In order to reduce such loss, a two (or more) wire transmission-line (TL) system should be used, whereby a new mode that has anti-phased currents in the two wires is created (Figure 2-8b). This mode, which is usually referred to as the 'bifilar mode', has fields that are concentrated in the vicinity of the TL and hence has lower cross-sectional coverage but relatively low loss [55].

Under some simplifying assumptions, a modal equation for the monofilar mode of a single wire in a rectangular tunnel was obtained by Wait *et al*. [56]. They extended their analysis in [56] to derive the modal equations for the monofilar and bifilar modes of a two open wire TL inside the rectangular tunnel and found the attenuation constants of these modes in a wide range of frequencies. They also considered the excitation of monofilar and bifilar modes in a TL in a circular tunnel by a short dipole antenna. Based on their results, the monofilar mode was excited more strongly by an antenna placed in the tunnel, but the bifilar mode showed lower attenuation. The excessive losses in the monofilar or coaxial mode are attributed to the return current flow along the tunnel walls.

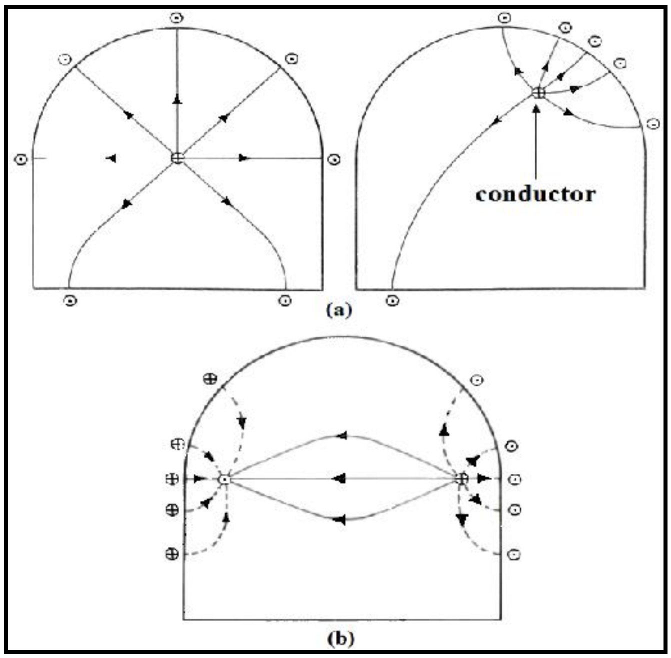

Figure 2-8 a) Current distribution and electric field lines of the monofilar mode (between each wire and the tunnel wall) and b) monofilar mode and bifilar mode (between the wires) [30].

In the bifilar or TL mode the fields are more confined to the region between the wire conductors [55]. Monofilar and bifilar techniques ultimately led to the radiating cables and leaky coaxial feeders which have been widely used for underground mine communications since the 1970’s. Leaky feeder systems can be obtained by introducing periodic discontinuities into the coaxial cable which convert radio frequency energy from a non-radiating bifilar mode to a monofilar mode. The discontinuities are created by the insertion of specially designed mode converters, or radiating devices in the cable at the desired intervals [57].

2.4.3 **Propagation Through-The-Air**

In this section, various analytical and numerical models used to characterize TTA propagation in mine tunnels are discussed. As it will be seen, developing analytical models for extreme environments such as underground mines can be very elaborate unless simplifying approximations regarding the tunnel geometry are made. These approximations have been modified over the years according to applications at higher frequencies, and availability of faster processors. For example, in several models underground tunnels were treated as tunnels with smooth walls. However, as technology has migrated toward higher frequencies, analytical modeling has become more sophisticated. As an example, a single-mode waveguide model [11] proposed about forty years ago could model the propagation loss of lower-UHF band signals in mine tunnels. Today's version has been modified and enhanced to multimode model which is capable of more precisely modeling propagation loss and delay spread in the upper-UHF band.

2.4.3.1 *Modeling Tunnels as Hollow Dielectric Waveguides*

In the UHF-band, a tunnel structure may guide the EM wave through the tunnel, and therefore can be modeled as a waveguide. Inside the waveguides, EM fields can be resolved into the sum of propagation modes given by the solutions of Maxwell's equations subject to the boundary conditions. These solutions include a dominant mode of propagation with the lowest loss and higher order modes with higher loss. Higher order modes travel at larger reflection angles relative to the waveguide axis (Figure 2-9), and therefore experience more reflections per unit distance and higher losses. Propagation modes of a hollow waveguide, in case of perfectly conducting walls are pure transverse-electric (TE, *i.e.*, E_z=0, $H_z \neq 0$) and transverse-magnetic (TM, *i.e.*, $E_z \neq 0$, H_z=0) modes. Different modes of $TE_{m,n}$ or $TM_{m,n}$ may propagate in the waveguide depending on the frequency and cross-sectional dimension of the waveguide.

In case of dielectric walls, propagating waves may be represented by hybrid modes of index *mn*, with all three Cartesian components of the electric and magnetic field present [58]. These modes are lossy modes because any portion of the wave that radiated on a tunnel wall is partially refracted into the surrounding dielectric and partially reflected back into the waveguide. The refracted part propagates away from the waveguide and represents a power loss. By knowing tunnel dimensions and material, Maxwell's equations subject to boundary conditions created by the interfaces between the interior of the tunnels and the wall materials, determine the cutoff frequency, propagation constant and propagation loss for each mode. These are important environmental parameters for wireless designs in tunnels and underground mines.

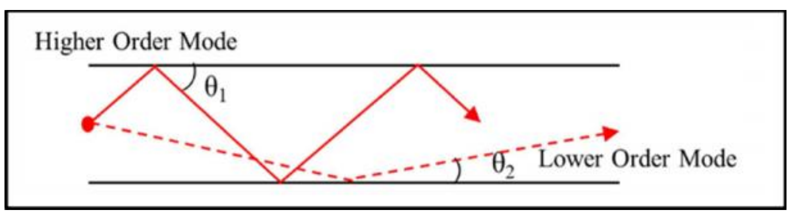

Figure 2-9 Comparison of reflection angles of lower and higher order modes in a waveguide.

Early theoretical work on hollow dielectric waveguides with circular and parallel-plate geometries in a medium of uniform dielectric constant was established by authors such as Marcatili and Schmeltzer [58] and Glaser [59]. Their work became the fundamental basis for later waveguide-based modeling of tunnels and underground mines [11]. Emslie *et al.* extended the previous work on waveguides to tunnels by treating them as oversized lossy dielectric waveguides with rectangular cross-sections and found approximate mode equations based on the simple assumption of uniform dielectric constant for the tunnel [11]. Mahmoud and Wait in [11] and Emslie *et al.* in [11] assumed dielectric constant of the sidewalls was different from that on top and bottom walls. This provides more accuracy than the simple assumption of same dielectric constant for all the walls. In [11], Emslie *et al.* applied waveguide model to tunnels with approximately rectangular cross-section, such as coal mines with considerable degree of roughness, and tunnels with tilted walls. Figure 2-10 shows a map and digital photograph of an underground mine gallery [60].

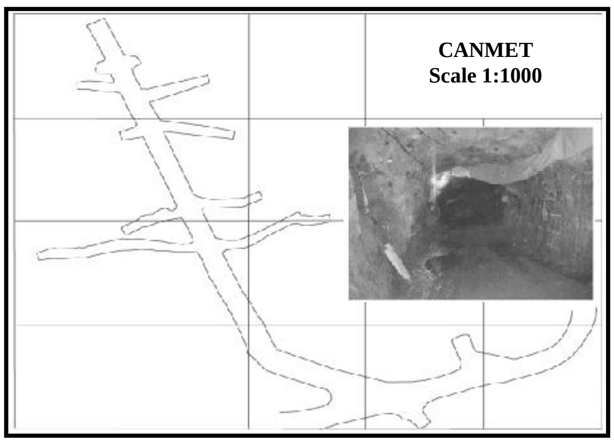

Figure 2-10 Map and digital photograph of an underground gallery [60].

They formulated the overall loss for the dominant mode of (m=1, n=1). Overall loss consists of refraction loss (proportional to f^{-2}), roughness loss (proportional to f^{-1}), sidewalls' tilt loss (proportional to f), and antenna insertion loss or equivalently antenna coupling loss to the dominant mode (proportional to f^{-2}). Antenna coupling loss occurs due to inefficient coupling of dipole antennas to the waveguide mode and decreases rapidly with increasing wavelength [11]. At frequencies of interest (UHF), ohmic loss due to the small conductivity of the surrounding material is found to be negligible compared to loss from refraction through the walls [11]. Refraction loss has been calculated for both horizontal and vertical polarizations of electric field, E_h, E_v, respectively. Depending on whether width or height of the tunnel is larger, one of horizontal or vertical polarizations, respectively dominantly propagate and accordingly only loss of the dominant polarization can be considered. Different losses assuming half-wavelength dipole antennas at both sides in a straight tunnel are given as follows [11]:

$$L_{refraction} = 4.343\lambda^2\left(\frac{\varepsilon_{r1}}{w^3\sqrt{(\varepsilon_{r1}-1)}} + \frac{1}{h^3\sqrt{(\varepsilon_{r2}-1)}}\right)d \quad \text{for } \mathrm{E}_{(1,1)}^{\text{horizontal}} \text{ mode } (\mathrm{m}=\mathrm{n}=1) \tag{5}$$

$$L_{refraction} = 4.343\lambda^2\left(\frac{1}{w^3\sqrt{(\varepsilon_{r1}-1)}} + \frac{\varepsilon_{r2}}{h^3\sqrt{(\varepsilon_{r2}-1)}}\right)d \quad \text{for } \mathrm{E}_{(1,1)}^{\text{vertical}} \text{ mode } (\mathrm{m}=\mathrm{n}=1) \tag{6}$$

$$L_{roughness} = 4.343\pi^2 r^2 \lambda\left(\frac{1}{w^4} + \frac{1}{h^4}\right)d \tag{7}$$

$$L_{tilt} = \frac{4.343\pi^2\theta^2}{\lambda}d \tag{8}$$

$$L_{\frac{\lambda}{2}\text{dipole insertion loss}} = \left[0.5233\frac{\lambda^2}{wh}\cos^2\frac{\pi x_0}{w}\cos^2\frac{\pi y_0}{h}\right] \quad \text{for } \lambda \le \text{tunnel transversal dimensions} \tag{9}$$

where λ, w, h, ε_{r1}, ε_{r2}, r, d, θ, x and y are wavelength, tunnel width, tunnel height, relative permittivity of the rectangular tunnel sidewalls, relative permittivity of the rectangular tunnel floor and ceiling, root-mean-square (RMS) roughness, distance, sidewalls' RMS tilt angle (in radians) about a vertical axis and transversal dimensions (assuming the origin of the rectangular coordinate system is on the middle point of the tunnel cross-section), respectively. As it can be seen from the formulas, some losses increase with frequency, and others decrease, and therefore an optimum frequency can be found in the range 500-1000 MHz (Figure 2-11) for minimum overall loss depending on the desired Tx-Rx distance.

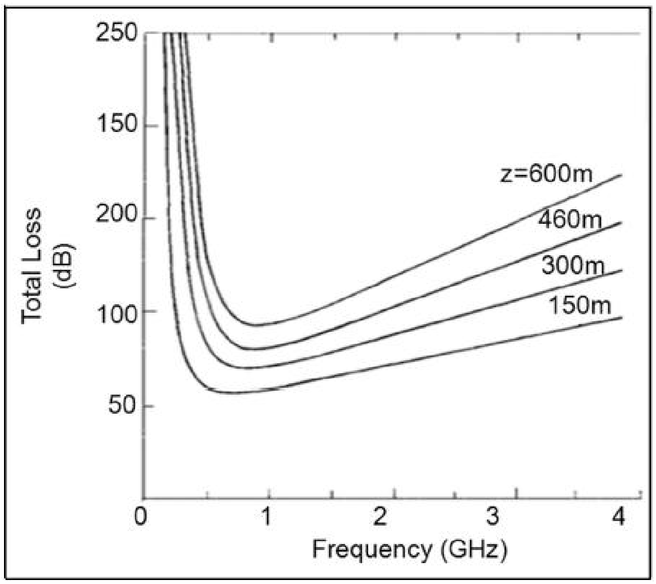

Figure 2-11 Overall loss for various distances along a straight tunnel for half-wave antennas with horizontal polarizations (*z* is Tx-Rx distance) [11].

Tables 2-1 and 2-2 present losses for different Tx-Rx distances and at several UHF frequencies for a straight tunnel, and a tunnel with a corner, respectively [11]. $L_{propagation}$ is total loss from refraction, roughness and tilt of the walls, and also $L_{insertion}$ is the half-wave dipole coupling loss which is noticeably high. In case of using antenna with high directivity, coupling loss (insertion loss) which considerably contributes in the overall loss will be reduced. Overall loss is the summation of propagation loss and insertion loss. As it can be seen in Table 2-2, a corner adds an extra loss directly proportional to the frequency. If the transmitter is outside the tunnel, additional loss due to EM coupling from outside to inside should also be considered which is not shown in these tables [61]. This loss is dependent on the distance of the transmitter to the mouth of the tunnel, angle-of-arrival of the wave into tunnel relative to the tunnel axis, cross-sectional dimension of the tunnel and operation frequency. It should be noted that the results discussed in this part and rest of this chapter are valid under the assumption of omni-directional antennas at transmitter (Tx) and receiver

(Rx). When using antennas with high directivity propagation is more similar to free space propagation rather than waveguide and is predicted to be less sensitive to tunnel's dimensions and frequency because waves have fewer interactions with tunnels' walls.

Table 2-1 Overall loss along a straight path (E_h mode with half-wave antennas) [11].

f	$L_{refraction}$	$L_{roughness}$	L_{tilt}	$L_{propagation}$	$L_{insertion}$	$L_{overall}$ (dB)				
MHz	dB/30m	dB/30m	dB/30m	dB/30m	dB	30m	150m	300m	460m	600m
4,000	0.06	0.05	5.33	5.44	69.90	75	97	124	152	179
3,000	0.10	0.07	3.99	4.16	64.88	69	86	107	127	148
2,000	0.23	0.10	2.66	2.99	57.86	61	73	88	103	118
1,000	0.91	0.21	1.33	2.45	45.82	48	58	70	81	93
415	5.34	0.50	0.55	6.39	30.48	37	62	94	126	158
200	23.00	1.04	0.27	24.31	17.80	42	139	261	383	504
100	92.00	2.08	0.14	94.20	5.80	100	477	948	1419	1890

Table 2-2 Overall loss along a path including one corner (E_h mode with half-wave antennas) [11].

f	E_h Loss per corner	Overall Loss (dB) at different Tx-Rx distances			
MHz	dB	150m	300m	460m	600m
4,000	80.2	177	205	232	259
3,000	77.6	163	184	205	226
2,000	74.1	147	162	177	192
1,000	67.6	126	138	148	161
415	57.7	120	152	184	216
200	47.3	187	308	430	551

For the sake of simplicity, Emslie and other authors neglected the continuity of the boundaries of the corner regions by considering different materials for ceiling/floor, and sidewalls [11]. One of the advantages of such approach is that the modeling of tunnels whose walls have different electrical characteristics is viable [34]. In this model, underground mines were assumed as rectangular waveguides with perfect geometrical shape, but with lossy dielectric characterization. Although this leads to separable Helmholtz wave equation in

Cartesian coordinates, the boundary conditions on the walls necessitate the intrinsically coupling of the basic modes and hence propagation constants are not easy to obtain. As shown by Wait [62], this causes fundamental difficulty in finding the modal eigenvalues and eigenfunctions of rectangular waveguide or any other form than circular. While most previous work on modeling tunnels use rectangular waveguides models, circular waveguide models have been considered for modeling arched road tunnels [63]-[67].

The single-mode waveguide model by Emslie *et al.* became the basis for later waveguide modeling of tunnels. Over time, several researchers tried to enhance the model and make it more accurate. Because this model only considers the dominant mode to predict the propagation loss at lower-UHF frequencies, it is only valid for the far-field region where higher order modes are greatly attenuated and only the dominant mode exists. Therefore, it fails to predict propagation loss in the near-field accurately. As such, for tunnel microcell designs Zhang *et al*. modified tilt and roughness loss formula of Emslie's model so that it became applicable to near-field [68].

The far-field (far-zone) and near-field (near-zone) inside straight tunnels are separated by a breakpoint [69]. The breakpoint will be explained in more details in the next subsection. Near-field waveguide propagation has not been well established but suffers larger loss than far-field propagation. This is because the higher order modes are significant in the near-field and should be included in calculations.

After the breakpoint (in far-field), higher order modes are greatly attenuated and become negligible, while the dominant mode remains significant. Far-field waveguide propagation is stabilized and undergoes smaller loss than near-field propagation [68]. The attenuation rate of the field in the far-zone is linear in dB, with a slope determined by the attenuation constant of the lowest order mode (dominant mode) [13]. At higher frequencies (above- UHF) that are much higher than the cutoff frequency of the tunnels, breakpoint is extended further from the transmitter; in other words, the near-field is prolonged. Therefore, to achieve a model that characterizes the near-zone as well, higher order modes should also be included [13],[70]. For example, in [13] more than 20 waveguide modes have been considered for accurate modeling at 1 GHz in a railroad tunnel. In [70], Sun *et al.* proposed the multimode-waveguide model, which is capable of accurately characterizing fast fluctuations of the channel, and gives analytical expression for the received power and the power-delay-profile (PDP) at any locations in a tunnel. Based on this model, authors studied the effects of various factors, such as size of the tunnel, frequency of operation, electrical properties of the walls, antenna position and polarization.

2.4.3.2 *Two-Slope Pathloss Model*

Based on the single-modewaveguide model, pathloss (in dB) increases nearly linearly with increasing distance in a mine tunnel. However, as shown in Figure 2-12, experimental and theoretical studies confirm that pathloss has two distinct sections that can be separated by a breakpoint for straight tunnels at UHF-band frequencies. Not having taken this breakpoint into consideration, the waveguide model has overestimated the coverage distance [71]. Before this breakpoint, the pathloss shows free space behavior (with free space pathloss exponent,*i.e.*, $n = 2$) and after it shows waveguide behavior (with lower pathloss exponent than free space, *i.e.*, $n \leq 2$) [71]-[73]. Accordingly, in [69],[71], Zhang proposed a ray-optical based hybrid model for tunnels and mines. This model consists of two types of propagation: (1) free-space model for the region close to the transmitter and (2) waveguide model in the region far from the transmitter. This was experimentally validated in [71],[74]. The location of the breakpoint can be obtained by intersecting two pathloss models as suggested in [69]. Breakpoint location depends on the tunnel excitation conditions (transmitter inside or outside the tunnel). In the case of an external base station, it depends on the angular position of the antenna with respect to the tunnel axis [72]. If the base station is inside the tunnel, the breakpoint location depends on the antenna radiation pattern, signal wavelength and size of tunnel cross-section. Assuming an omni-directional antenna such as a dipole at both transmitter and receiver inside the tunnel rbp, the breakpoint location (or critical distance) mainly depends on the tunnel cross-sectional dimensions (w, h) and the wavelength (λ) [73]:

$$r_{bp} = max\left(\frac{w^2}{a}, \frac{h^2}{a}\right) \tag{10}$$

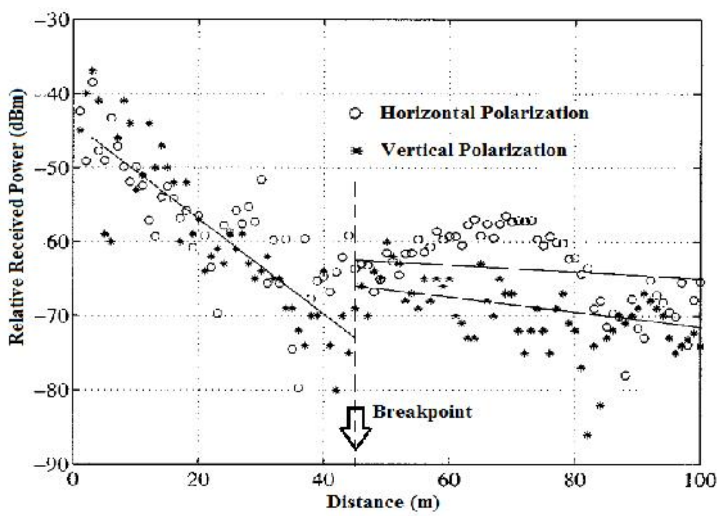

Figure 2-12 Measured data for two polarizations at 900 MHz together with the two-slope regression fits in a coal mine [74].

It should be noted that this simple model is only for pathloss modeling and cannot characterize the small-scale signal fluctuations of the multimode channel in particular in the near-field zone. Moreover, this model may not be applied to some short mine tunnels at high frequencies. For example, in CANMET mine at a 40 m depth for two frequencies of

2.45 GHz and 18 GHz, the value of (w^2 /λ) is 200 m and 1800 m, respectively. Therefore, the tunnel is too short to form a breakpoint and hence no waveguide effect is likely present [75]. Consequently, multimode modeling may be considered for propagation modeling of higher frequencies in short mine tunnels.

2.4.3.3 *Ray-Optical Models*

Ongoing interest in higher frequency (smaller wavelength) applications has motivated researchers in this field to use ray-optical theory for their modeling. Ray-optical models are accurate when the environment dimensions are much larger than the wavelength and this is a condition that is satisfied in underground tunnels at UHF-band frequencies. In these models, EM waves are considered as optical rays, and EM fields are calculated by summing the reflected rays from the tunnel walls. Unlike modal analysis in the waveguide model, which is restricted to simple geometries, ray-optical methods can be applied to more complicated scenarios such as occupied tunnels, tunnels with curvature, coupling between outside and inside of the tunnel, *etc*.

Ray-optical methods based on the classical geometricaloptics (GO) only take into account reflections and not diffractions. Those based on geometrical-theory-of-diffraction (GTD) [76] include both reflections and diffractions, however, the predicted fields at shadow boundaries become infinite, which is impossible in nature and produces a non-uniform solution. On the other hand, in uniform-theory-of-diffraction (UTD) [77], an extension of GTD, diffracted fields remain bounded across the shadow boundaries because of the addition of a transition function into the diffraction coefficient.

In [78], Mahmoud and Wait proposed a GO model for rectangular mine tunnels and compared it with their previous waveguide model for a case of an idealized waveguide with two perfectly reflecting sidewalls. Two models showed a satisfactory agreement. This was a theoretical foundation for further analysis. Thereafter, they included the influence of the wall roughness in their model by using theoretical and experimental results obtained by Beckmann and Spizzichino [79] and Beard [80], respectively. In this simple model, the rough surface is assumed to have a Gaussian distribution and modified Fresnel reflection coefficients are considered for the rough surface. The classical Fresnel reflection coefficient is used for smooth surfaces. In [81], a ray-optical model based on GO was developed to include curved boundaries. Contrary to classical ray-optical methods where one ray representing a local plane wave front is searched and can only treat reflections at the plane of boundaries, this ray-optical method is based on ray-density normalization and requires multiple representatives of each physical EM wave at a time. Therefore, curved boundaries can also be treated.

In [82], authors applied the UTD method to accurately model the coupling between inside and outside of the tunnel. This is a critical issue for short road tunnels, where the transmitter is outside the tunnel and the mobile station is inside with no repeaters between them. This is a case that cannot be easily modeled with waveguide or simple GO based model. A model based on the UTD was also proposed in [83] that allows one to find the effect of tunnel branches and obstructions such as vehicles and trains in a tunnel.

2.4.3.1 *Full-Wave Models*

Full-wave models may also be considered as an alternative method capable of solving Maxwell’s equations with arbitrary boundary conditions using numerical methods, such as finite-difference-time-domain (FDTD). The FDTD method is an accurate model that fully accounts for the effects of reflection, refraction and diffraction, and provides a complete solution for the signal coverage information throughout a defined problem space. Therefore, it is well suited for accurate study of the EM propagation in complex environments. However, the FDTD requires memory to store the basic unit elements of the model and also demands iterations in time in order to update the fields along the propagation direction. Given the large size of tunnels and the high operating frequency (above-UHF), the computational burden of conventional FDTD exceeds well beyond the capacity of existing computers. Consequently, it has recently been attempted to enhance the efficiency of this method for wireless applications in tunnels by employing different approaches to reduce the runtime or computational cost.

In [84], excessive computing times were shown to be alleviated via the compute-unified-device-architecture (CUDA) parallel programming route. Whereas in [85], a cost-effective FDTD method for modeling tunnels with realistic construction profiles is proposed, which is based on the compact-FDTD concept and requires minimal computing resources. In [86], the authors have proposed the modified 2D FDTD method that converts a 3D tunnel model into a realistic 2D FDTD simulation. This removes the computational burden while at the same time preserving the factors that form the wireless propagation characteristics. This method has been used to determine a pathloss model that enables effective wirelesssensor-network (WSN) planning and deployment for monitoring and assessing deformation in curved arched-shaped tunnels for Tx-Rx distances of up to several hundred metres. For such applications, the FDTD method facilitates accurate modelling of near distance pathloss and close-to-wall antenna deployments. For most wireless propagation models of tunnels, the antennas are assumed to be along the central axis of the tunnel. Because this is not representative of most WSN applications where the wireless sensor nodes are mounted on the walls, it is important to accurately capture the performance degradation resulting from the antenna position using accurate full-wave models.

2.4.3.2 *Stochastic and Numerical Models*

In recent studies on modeling EM propagation in underground mines, more details of the environment such as wall roughness are included in order to improve the accuracy. In most theoretical models concerning roughness, statistical solutions based on the Gaussian distribution for random roughness are employed. In [87], stochastic scattering approach is presented to treat rough surface scattering based on a combination of ray-optical and Kirchhoff formulations. Similar to the Kirchhoff modeling, this method is based on a tangential plane approximation of the rough surface, *i.e.*, it is applicable to surfaces with gentle undulation whose horizontal dimensions are large compared to the wavelength of incident waves. However, in contrast to Kirchhoff methods that are only valid for either slightly rough or very rough surfaces, this approach simultaneously includes both.

In this method as shown in Figure 2-13, each local plane wave front is represented by multiple discrete rays instead of one ray, in order to model wall roughness. All of these discrete rays are reflected back from randomly oriented planes (Figure 2-13b) and not from the same boundary plane (Figure 2-13a). In this model, random roughness is characterized by standard deviation of surface height and correlation length, assuming they follow a Gaussian distribution. By applying this stochastic scattering approach, the inclusion of random surface scattering into ray-optical modeling becomes possible.

In [88], a numerical analysis has been used to accurately model roughness and bending in underground mines. In this analysis, the cascade-impedance-method (CIM) and segmental-statistical-method (SSM) are combined. The CIM method assumes the mining tunnel is a transmission line with diffracting and rough walls (Figure 2-14a). Therefore, its behaviour can be considered analogous to a cascade of dielectric impedances with its associated losses (Figure 2-14b). In Figure 2-14a, Z's are the dielectric impedances of the tunnel sidewalls, ceiling and floor. CIM is combined with SSM by dividing the mining tunnel into segments, each segment into sections and each section into multiple cells in the transversal and vertical directions. Variation distribution of the rough surface of each segment is then simulated by a 3D Gaussian function. From the dielectric impedances of the rough walls, equivalent reflection and transmission coefficients of each section in the form of matrix can be obtained. This allows the electric field, magnetic field, cutoff frequency and propagation constant to be determined for each segment of the tunnel.

The limitation of this method is in treating the borders of the grid. If the sections are chosen to be infinitely small, the problems of memory space and runtime arise. Therefore, to simplify the method and overcome these problems, the authors chose to substitute parameters of each section with their average values. As stated by the authors, these types of methods are preferred over modal analysis (waveguide models) for tunnel mines with rough sidewalls. However, for the case of smooth sidewalls, simple modal theory would be more effective.

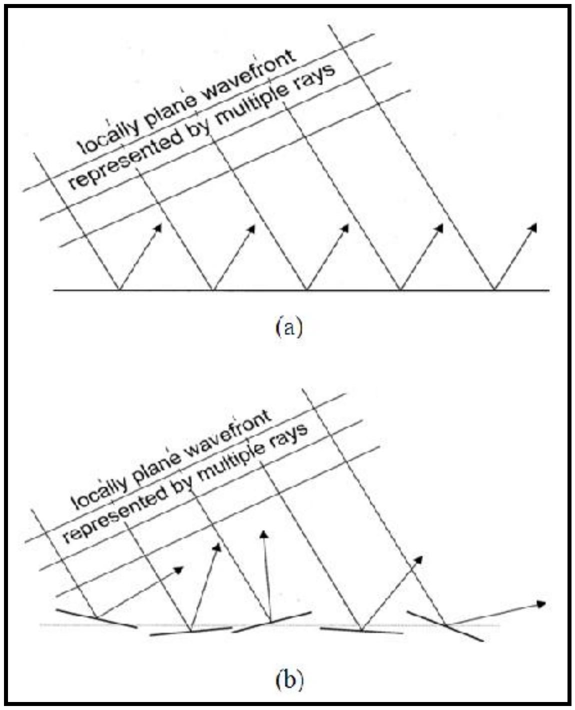

Figure 2-13 Stochastic scattering approach: reflection at randomly oriented tangential planes for each discrete ray (a) same plane for all the rays and (b) randomly oriented planes [87].

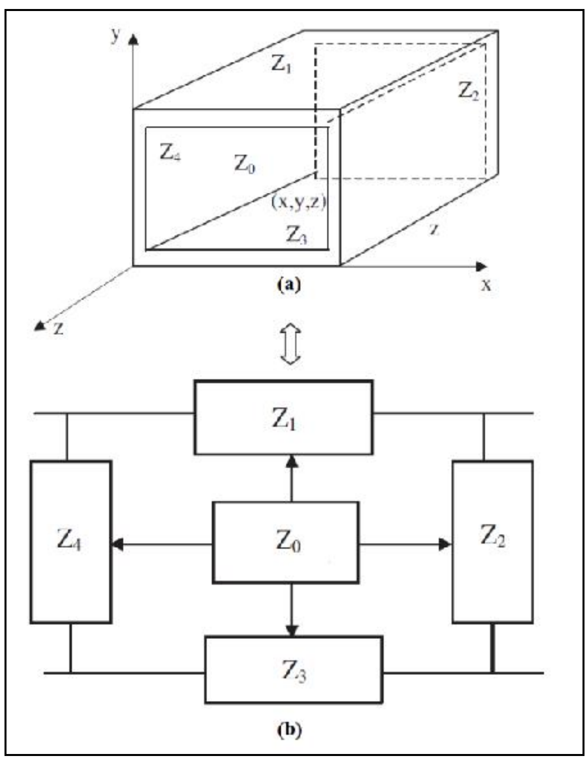

Figure 2-14 (a) A rectangular waveguide and (b) CIM model for the waveguide in Figure (a) [88].

Comparison of Analytical Models

As it was seen in this section, different theoretical models have been developed for characterizing propagation in underground mine tunnels. In Table 2-3, the main advantages and disadvantages of each are presented which helps to compare them based on several criteria such as complexity, range of validity and modeling capabilities.

Table 2-3 Comparison of different analytical models

	Single-mode waveguide model	**Multimode waveguide model**	**Two-slope model**	**Ray-optical models**	**Stochastic & Numerical models**
Advantages	(1) Simple (2) Provides physical insight (3) Basis for most of theoretical modelings	(1) Accurate for different frequencies (2) Accurate for near-zone as well as far-zone (3) Provides physical insight (4) Capable to predict channel parameters such as. RMS delay spread	(1) Simple (2) Same accuracy for near-zone and far-zone (3) Provides physical insight	(1) Simple (2) Capable of modeling tunnel branches (3) Provides physical insight	(1) Similar for different frequencies (2) Same accuracy for near-zone and far-zone (3) Capable of modeling tunnel roughness and branches
Disadvantages	(1) Less-accurate for higher frequencies (2) Only for pathloss predictions (3) Only valid for far-zone of the tunnel (4) Incapable to model tunnel roughness and branches	(1) Complex (2) Incapable to model tunnel roughness and branches	(1) Fails to model cases in which breakpoint does not exist (*e.g.*, when mine tunnel is too short to form breakpoint) (2) Incapable of modeling tunnel roughness and branches	(1) Less-accurate for lower frequencies (2) Computational load increases dramatically as the signal path is prolonged	(1) Complex (2) Provides no physical insight (3) Computationally extensive

As shown in Table 2-3, theoretical models provide valuable physical insights about the EM propagation. However, because most of them are based on non-realistic assumptions, they need to be evaluated experimentally. Although the expense and level of effort for conducting RF measurements increases in complicated environments, the measurement based approach has proven to be useful and productive. It will likely remain the principal method for characterizing wireless channels in most environments for many years to come. As a result of its relevance, the next section is devoted to experimental modeling for underground environments.

2.5 Measurement-Based Modeling

While theoretical models offer physical insights, empirical models are widely used to characterize wireless channels because they: (1) are more realistic, (2) provide results that are of immediate use to designers and developers, and (3) are useful in the validation of results obtained from simulation-based and theoretical methods. Despite the mentioned advantages, due to the difficulties of access to underground mines, safety issues, measurement complexity and expenses, they are not as common in the literature as theoretical studies.

Measurement studies for TTA communications at lower- UHF frequencies began in narrowband form with the motivation of characterizing propagation loss. They have been evolved over time into wideband and ultra-wideband signals with the motivation of characterizing channel-impulseresponse (CIR) and delay spread. As shown in this section, while narrowband pathloss characterization is used to determine coverage area and transmit power, wideband measurements capture the effects of multipath components by characterizing the CIR.

2.5.1 **Narrowband Measurements**

Narrowband measurements mostly focus on modeling fading statistics and propagation loss. In this section, we present key findings on characterizing propagation in underground mines and compare them with their counterparts in conventional surface environments as well as long tunnels.

2.5.1.1 *Fading Statistics*

The distributions, namely, Rayleigh, Rice, Nakagami, Weibull and Lognormal are among the most commonly used in wireless communications. Rice and Rayleigh are used for modeling LOS and NLOS small-scale fading, respectively, while Lognormal is used for large-scale fading above ground. The fading distribution is Ricean (or Rice) when a dominant stationary (non-fading) signal component such as the LOS path is present. As the dominant signal becomes weaker, the fading distribution will follow a Rayleigh distribution. Components of small-scale and large-scale fading can be separated by applying different methods on the NB measured data. For example, the small-scale fading envelope can be extracted from the measured data by normalizing the received signal to its local mean value.

Some experimental studies of straight sections in underground mines have shown they are similar to surface environments; the large-scale fading follows Lognormal distributions [89], the small-scale fading follows Ricean distribution for LOS scenarios and Rayleigh distribution for NLOS scenarios, regardless of frequency [75],[90]. However, some studies such as the recent one in [89], have reported smallscale fading to follow Rayleigh distribution for some LOS cases in underground mines. This can be attributed to the rich multipath environment formed by the high density of scatterers in the mine.

2.5.1.2 *Pathloss Exponent*

Several experimental studies have characterized the pathloss exponent for different LOS and NLOS scenarios in underground mines and compared the findings with other environments. The study reported in [91] shows that at upper-UHF, pathloss exponents in underground mines are larger than their counterparts in indoor environments [91]. This can be explained by the fact that in indoor environments, such as in a corridor or a hallway with smooth walls and clear of obstacles, the pathloss exponent is lower than that of free space due to the constructive contribution of multipath signals. In mines, however, the walls irregularities and roughness are significant, and hence destructively contribute to the signal power resulting in a pathloss exponent similar to that of free space (n = 2) [91].

In another study, LOS and NLOS scenarios for two frequencies (2.4 GHz and 5.8 GHz) have been compared. 2.4 GHz showed a lower pathloss exponent than 5.8 GHz for the LOS scenarios, while 5.8 GHz showed a lower pathloss exponent than 2.4 GHz for the NLOS scenarios [75]. This result shows the difference between propagation in mines and in long straight tunnels (*e.g.*, transportation tunnels) where increase in frequency decreases the pathloss exponent [92]. This confirms that there are substantial differences between underground mines and transportation tunnels, and therefore may not be treated under same category for accurate modeling. Table 2-4 compares and contrasts UHF-band propagation based on theoretical and experimental studies, in underground mines and two similar environments; (1) long straight tunnels and (2) conventional indoor environments.

Table 2-4 Some similarities and differences between underground mines, straight long tunnels and conventional indoor for propagation at UHF-band (*f*: frequency, *n*: pathloss exponent, τ_{rms}: RMS delay spread, $d_{Tx\text{-}Rx}$: Tx and Rx distance, ↑: increase, ↓: decrease)

<table>
<tr><th></th><th></th><th>Straight long tunnel
[70],[92]</th><th>Conventional indoor
[75],[88]</th></tr>
<tr><td rowspan="2">Underground mine (experimental study)
[75]</td><td>Similarities</td><td>Large-scale fading: Lognormal

Small-scale fading: Rice, Rayleigh

$f \uparrow \Rightarrow \tau_{rms}$ (near- region) ↓

Scatterers and obstacles increase τ_{rms}</td><td>Large-scale fading: Lognormal

Small-scale fading for LOS: Rice (Rayleigh has been also reported for some studies in mines)

Small-scale fading for NLOS: Rayleigh

Scatterers and obstacles increase τ_{rms}</td></tr>
<tr><td>Differences</td><td><u>In underground mines:</u>

$f \uparrow \Rightarrow n$ (near-region) ↑

$f \uparrow \Rightarrow \tau_{rms}$(far- region) ↓

No correlation between $d_{Tx\text{-}Rx}$ and τ_{rms}</td><td><u>In underground mines:</u>

No impulse response path arrival clustering effect

Relatively larger pathloss exponent

No correlation between $d_{Tx\text{-}Rx}$ and τ_{rms}</td></tr>
</table>

2.5.2 Wideband/UWB Measurements

Assuming the wireless channel acts as a linear filter, wideband measurements help in characterizing it accurately in the time and frequency domain by determining the CIR [42],[93],[94]. From the CIR, the PDP can be obtained, which determines RMS delay spread, received power, time-of-arrival (TOA) of the first path, *etc.* Providing accurate temporal information, the CIR can also be used for location finding applications in underground mines.

2.5.2.1 *Delay Spread*

In low data rate wireless systems (*i.e.*, when the symbol rate is lower than the coherence bandwidth of the wireless channel), delay spread can be neglected, and hence

Gaussian noise is the dominant factor that causes bit errors. In high data rate systems on the other hand, delay spread, which causes inter-symbol-interference (ISI), is the main reason for bit errors [42]. As a result, it is necessary to model degrading effects of multipath delay as well as fading in modern wireless communication systems with high data rates. By characterizing RMS delay spread, coherence bandwidth that is necessary for optimization of modulation schemes and data rate, can be determined. Accordingly, wideband measurements have been conducted in underground mines and tunnels to characterize the CIR. Similar to surface measurements, many factors such as frequency, wave polarization, height and transversal (*i.e.*, cross-sectional or bi-dimensional) locations of the transmitter and receiver, scatterers and obstacles between transmitter and receiver affect the CIR [71],[75].

For long straight tunnels, the RMS delay spread is found to be: (1) a function of Tx-Rx distance, (2) larger for horizontally polarized waves in tunnels with horizontal aspect-ratio (*i.e*., width is larger than height) and (3) larger for occupied tunnels [70],[92]. However, some of these results have not been achieved for mine tunnels. For example, no correlation between the Tx-Rx distance and the RMS delay spread has been found in mines [75], but has been found to be a function of Tx-Rx distance in both tunnels and indoor environments. The function is an increasing function at first and a decreasing function after a certain point (dual-slope relation) [70]. Some of these similarities and differences between mines and tunnels and conventional indoor environments are listed in Table 2-4.

RMS delay spread in mines has been found to be highly dependent on bidimensional position of the antennas [60] and larger in a mine with more rough walls, branches and obstacles [60],[92]. It has also been compared for different frequencies. In [75], two WLAN frequencies of 2.4 and 5.8 GHz have been compared. This study found the RMS delay spread to be larger for 2.4 GHz and they concluded that the maximum usable data rate with a relatively simple transceiver would be higher at 5.8 GHz in the mine they conducted their measurements.

In Table 2-5, typical values for the pathloss exponent and RMS delay spread of different environments are presented. This allows the reader to compare underground mines with other environments more conveniently. It can be seen that for underground mines, the pathloss exponent and RMS delay spread have been found in the range of 1.8-5.49 and 1.7-60 nsec, respectively. The range of values varies according to the measurement scenario, size of the tunnel and frequency. A more detailed comparison of experimentally determined UWB and fading statistics experimental between mines and different indoor scenarios can be found in [89].

2.5.2.2 *Location Finding*

CIR characterization achieved through WB measurement can also be used to accurately (to within 2 m) locate mobile stations in mines and other confined environments for location tracking applications. As an example, the CIR provides the required information for using the fingerprinting technique, which in conjunction with a neural network can accurately locate the mobile [95]. Each user's information, such as CIR and PDP, is a function of user's location and can be obtained by several offline wideband measurements. These are recorded in a user fingerprint database and subsequently compared to real-time measured fingerprints corresponding to the user's new location [95].

Table 2-5 Pathloss exponent and delay spread assuming omni-directional antennas for several frequencies in different environments.

<table>
<tr><th colspan="2">Type of Environment</th><th>Measurement frequency (GHz)</th><th>Size (width × height × length)</th><th>Mean τ_{ms} (RMS-delay spread) in nsec</th><th>Pathloss exponent (n)</th><th>Reference</th></tr>
<tr><td colspan="2">Free Space</td><td>-------</td><td>-------</td><td>-------</td><td>2</td><td rowspan="5">[42],[93]</td></tr>
<tr><td colspan="2">Urban Area Cellular Radio</td><td rowspan="4">UHF-band</td><td rowspan="2">Hundred metres (an outdoor site)-Several kilometers (San Francisco)</td><td rowspan="2">40-25500</td><td>2.7-3.5</td></tr>
<tr><td colspan="2">Shadowed Urban Area Cellular Radio</td><td>3-5</td></tr>
<tr><td colspan="2">In-Building (LOS)</td><td rowspan="2">Typical office-Open plan factory</td><td rowspan="2">4-130</td><td>1.6-1.8</td></tr>
<tr><td colspan="2">Obstructed In-Building</td><td>4-6</td></tr>
<tr><td rowspan="2">Several Straight Long Tunnels</td><td>Empty</td><td rowspan="2">0.9</td><td rowspan="2">Tunnel1: 3.34×2.6×259
Tunnel2: 7.5×4×2000
Tunnel3: 4.2×3×10,000
Tunnel4: 2.4×2×200
Tunnel5: 7×3.7×120</td><td>Less than 25</td><td rowspan="2">1.87-5.49</td><td rowspan="6">[92]</td></tr>
<tr><td>Occupied</td><td>Less than 103</td></tr>
<tr><td rowspan="2">Straight Long Tunnel</td><td>Empty</td><td rowspan="2">0.9</td><td rowspan="2">3.34×2.6×259</td><td>4.12</td><td rowspan="2">4.2-4.49</td></tr>
<tr><td>Occupied</td><td>21.7</td></tr>
<tr><td rowspan="2">Straight Long Tunnel</td><td>Empty</td><td rowspan="2">1.8</td><td rowspan="2">3.34×2.6×259</td><td>6.03</td><td rowspan="2">2.12-2.46</td></tr>
<tr><td>Occupied</td><td>58.65</td></tr>
<tr><td rowspan="2">Underground Mine (Level 70m)</td><td>LOS (1-10m)</td><td rowspan="2">UWB (3-10)</td><td rowspan="2">(2.5-3)×3×70</td><td>1.72</td><td>1.8</td><td rowspan="2">[94]</td></tr>
<tr><td>NLOS (1-10m)</td><td>3.76</td><td>4.01</td></tr>
<tr><td colspan="2">Underground Mine (Level 40) NLOS & LOS</td><td>2.4</td><td>5×5×75</td><td>Less than 60</td><td>2.13-2.33</td><td>[60]</td></tr>
<tr><td rowspan="2">Underground Mine (Level 70)</td><td>LOS (d=1m)</td><td rowspan="2">2.4</td><td rowspan="4">(2.5-3)×3×70</td><td rowspan="2">6.34</td><td>2.03</td><td rowspan="4">[75]</td></tr>
<tr><td>NLOS (d=23m)</td><td>4.62</td></tr>
<tr><td rowspan="2">Underground Mine (Level 70)</td><td>LOS (d=1m)</td><td rowspan="2">5.8</td><td rowspan="2">5.11</td><td>2.22</td></tr>
<tr><td>NLOS (d=23m)</td><td>3.51</td></tr>
<tr><td rowspan="2">Underground Mine</td><td>LOS (d=40-44m)</td><td rowspan="2">0.4-0.5</td><td rowspan="2">5×6×500</td><td>19</td><td>-------</td><td>[12]</td></tr>
<tr><td>NLOS</td><td>25-42</td><td>-------</td><td>[12]</td></tr>
</table>

The database, however, should be updated due to the fact that mines are dynamic environments [50],[96]. Heavy machinery or moving objects may considerably change the properties of the channel, requiring an update of the database's information (*e.g.*, a new training of the neural network). This channel variation issue can be resolved by using a master neural network [50], [96].

2.5.3 Multiple-Antenna Measurements

In addition to experimental studies of single-antenna systems in underground tunnels, multiple-antenna systems such as multiple-input-multiple-output (MIMO) systems have also been studied. Because there have been no MIMO studies in mines to date, results presented here are from experimental studies in transportation tunnels that are relatively similar to mine tunnels. MIMO measurements for underground tunnels were originally motivated by interest in supplying GSM-Rail service at 900 MHz [21], and most recently for advanced WLAN, worldwide-interoperability-for-microwaveaccess (WiMAX) and long-term-evolution (LTE) service at 2 GHz, in transportation tunnels. It is a well-known fact that performance of a MIMO system is mostly affected by the correlation between fading observed on adjacent antenna elements. This correlation depends on the type and configuration of the antennas and the range of angles over which the signals arrive or depart (quantified by angular spread of transmitter and receiver).

Despite the small angular spread of the direction-of-arrival (DOA) and direction-of-departure (DOD) of the rays in the tunnels, preliminary experimental results have shown that multiplexing gain (or capacity gain) is achievable by employing multi-antenna techniques [21],[24],[97]. However, the channel capacity is strongly dependent on the Tx-Rx distance, tunnel size and geometry. In a MIMO study in [24], correlation distance of antenna elements is found to be an increasing function of the transmitter-receiver separation, and is larger for receiver elements in tunnels of smaller sizes. Correlation distance is the average spacing between two neighboring antenna elements at one end that produces a correlation coefficient smaller or equal to a certain value, typically 0.7. Antenna spacing in a MIMO system should not be less than the correlation distance to achieve acceptable performance. Despite the valuable contributions of MIMO studies in underground tunnels, MIMO performance is still uncertain in underground mines because of physical differences. This gap in the research, along with the promising results from MIMO in transportation tunnel studies, may encourage researchers to consider MIMO in underground mines for their research.

2.5.4 Techniques to Overcome Channel Impairments

In this section, we will discuss required baseband modeling considerations, which should be taken into account while designing underground mine radio receivers. In this regard, the main focus is on combating key channel impairments such as multipath fading (causing fading), delay spread (causing ISI) and Doppler spectrum (causing inter-carrier-interference: ICI). Experimental characterization of channel impairments can be very useful in radio receiver designs.

To eliminate ISI in underground environments, the orthogonal-frequency-division-multiplexing (OFDM) technique that is well-known for high data-rate wireless transmissions and robustness to multipath delays is used [98],[99]. OFDM is intrinsically capable of combating common distortions in the wireless channels without requiring complex receiver algorithms. Compared to conventional single carrier techniques, OFDM-based systems have a low complexity implementation in which instead of a complex equalizer, channel estimation based on the CIR is used to recover the received signal. The vector CIR can be represented by the following formula [100]:

$$h(t) = \sum_{i=1}^{K} A_i(t)\, e^{j\varphi_i(t)} \delta\left(t - \tau_i(t)\right) \tag{11}$$

where i is the number of multipath components, $A_i(t)$ is the amplitude of the i^{th} path, $\tau_i(t)$ is the time delay of the i^{th} path and $\varphi_i(t)$ is the phase shift of the i^{th} path. A wideband experimental characterization in CANMET mine [101] reveals that TOA of paths follow a modified Poisson distribution and their amplitudes undergo Rayleigh or Rice fading with uniformly distributed phase over [0, 2π]. Based on this statistical information and using the above formula, an OFDM channel estimation method is studied for wireless LAN communications in underground mines [99], which employs the pilot-symbol-assisted (PSA) method. Performance of different estimation algorithms and modulation schemes such as 16 quadrature-amplitude-modulation (16QAM) for a 24 Mbps link, quadrature-phase-shift-keying (QPSK) for a 12 Mbps link, and binary-phase-shift-keying (BPSK) for 6 Mbps link, derived from the IEEE-802.1l wireless-LAN standard, are assessed and compared in terms of the bit-error-rate (BER).

To combat multipath fading for WSN applications in underground mines, the chirp-spread-spectrum (CSS) method is proposed [83]. The CSS uses wideband linear frequency modulated chirp pulses to encode information. It is resistant to channel noise, multipath fading even when operating at very low power and Doppler shift for mobile applications. The CSS method is suitable for wireless personal and sensor network communications, which require low power usage and need relatively low data-rates (1 Mbit/s or less).

Rather than combating, multipath components can also be exploited effectively in underground mines for increasing SNR based on diversity combining methods. This can be achieved by combining the energy in various multipath components using a rake receiver. A Rake receiver is not considered feasible in other industrial environments due to the large number of fingers required to combine the many resolved multipath components [102],[103]. In underground mines, however, the energy is concentrated in fewer multipath components, and hence the number of fingers required is far less [104]. Study in [99] shows that the OFDM channel estimation that performs well at low Doppler frequency can efficiently reduce the effect of Doppler shift in underground mines. Nevertheless, due to low vehicle speeds, *i.e.*, typical in underground mines, system performance is less affected by ICI, and therefore ICI can be neglected [99]. Unlike underground mines where Doppler spectrum is negligible, it is one of the key channel impairments for vehicular-to-vehicular (V2V) applications in subway tunnels. This should be considered while designing vehicular wireless communication systems such as intelligenttransportation- systems (ITS). In [105], a V2V wireless channel inside a large subway tunnel has been experimentally characterized. It is shown that the V2V fading process is inherently non-stationary, and based on the estimations, RMS delay and Doppler spreads are log-normally distributed. Their study reveals that the spreads, excess delay, and maximum Doppler dispersion are larger on average when both vehicles are inside the tunnel compared to the “open-air” situation. Satisfying the institute-of-electrical-electronics-engineers 802.11p (IEEE-802.11p) standard requirements, they concluded that this standard will be robust towards inter-symbol-interference (ISI) and ICI inside a tunnel.

As was seen in this section, measurement-based characterization of underground mines provides realistic results that are of immediate use to designers and developers, and therefore has attracted more attention in the last decade. However, before applying the results, one must ensure that measured data is sufficient for any statistical inference about the propagation environment. This can particularly be a concern for underground mines because mine galleries differ from mine to mine, and even from level to level within the same mine [94]. Inconsistent experimental results from different UWB measurements in mines confirm this fact [94]. As a result, more measurement campaigns are required to achieve more general and non-site-specific conclusions about propagation in underground mines and their galleries.

2.6 Implications for Wireless Communication System Design

Designers and developers use channel models to predict and compare the performance of wireless communication systems under realistic conditions and to devise and evaluate methods for mitigating the impairments and distortions that degrade wireless signals. In this section, general conclusions achieved from characterization of wireless propagation in underground environments are presented.We will see how tunnel dimension and geometry, wall material and obstructions affect parameters such as optimum frequency, attenuation, RMS delay spread and angular information that are required in effective design of wireless systems. Additionally, we will see how antenna properties may be affected by underground geometry. This information is particularly valuable when configuring designs for multiple antenna systems.

2.6.1 **Frequency of Operation**

The optimum frequency for TTA communications in underground mines depends on several factors, including tunnel size, tunnel geometry and infrastructure inside the tunnel.

At the frequencies below UHF-band (MF-VHF), signal propagation is enhanced via coupling to conductors that may be in the mine entries, and antenna efficiency is not necessarily compatible with sizes that are portable [31]. At UHF frequencies on the other hand, theoretical studies show that mine tunnels act as relatively low-loss dielectrics with dielectric constants in the range 5-10, and therefore transmission takes the form of waveguide propagation in the tunnel [11]. As it has been shown by Emslie *et al.* in the 500-1000 MHz range, attenuation is relatively low in straight mine entries [11].

In contrast, practical tests have revealed that the MFband (300 kHz-3 MHz) has more desirable coverage with less severe attenuation compared to UHF-band in both coal and metal/non-metal mines [38]. The MF-band has a proven coverage area of 300-460 m in conductor-free areas, and as much as 3200 m in conductor-filled areas where parasitic propagation help the signal travel longer distances [38]. Higher frequencies such as VHF, UHF and SHF propagate in LOS and 300 m down a mine entry. However, it is unlikely that an unaided (*i.e.*, no leaky feeder) VHF or UHF signal would be able to travel around more than about two crosscuts [38].

This contradiction can be explained by noting that attenuation rate of UHF frequencies is lower than MF frequencies assuming that the tunnel has smooth walls, is straight and empty. This is an unlikely situation for most underground mines and as it has been shown that attenuation of UHF frequencies is significantly higher when the signal propagates around a corner or when obstacles such as massive piece of machinery is in the path of propagation [31].

As a result, considering practical tests, and theoretical and experimental results, although high frequencies (UHF and higher) may offer a larger coverage area in straight and unobstructed tunnels, better coverage may be achievable by frequencies lower than UHF (MF-VHF) [30],[38] when corners, crossings and obstacles exist. Regardless, UHFbased technologies are more appealing to the mining industry because low cost, small form factor, scalable and easy to use applications are available off-the-shelf. In addition, their coverage and other propagation issues (*e.g.,* requiring lineof- sight between Tx and Rx) can be resolved by appropriate antenna and wireless network designs.

2.6.2 **Tunnel Geometry**

In this subsection, we discuss how tunnel structure impacts wireless communications in underground mines. In addition to pathloss, extra losses in tunnels are introduced due to tunnels' curvatures, sidewalls' tilt and changes of the cross-sections.

2.6.2.1 *Cross-Sectional Dimension*

Because each tunnel behaves like a waveguide, its cross-sectional dimension determines the cutoff frequency. For tunnels of arbitrary shape, a very rough approximation of the cutoff frequency is determined by the frequency whose free-space wavelength is about or equal to the tunnel perimeter. Well above this cutoff frequency, the number of propagating modes grows by the square of frequency. The cross-section of most tunnels that can accommodate vehicles, has dimensions of a few metres and the cutoff frequencies are consequently of a few tens of megahertz [106].

In addition to cutoff frequency, cross-sectional size also impacts the attenuation constant and small-scale fading statistics, owing to the fact that change in tunnel cross-sectional size is equivalent to change in frequency for TTA propagation. As such, an increase in a tunnel's width and height increases small-scale fading, which is similar to the impact of increasing frequency. For tunnels with larger cross-sectional dimensions compared to the wavelength, multipath becomes more significant, leading to more severe fluctuations and greater fading [11],[31],[71],[107],[108]. In addition, in larger dimension tunnels the attenuation constant is smaller, and therefore the nearfield zone with small-scale and deep fluctuations is prolonged [70]. Severe small-scale fading for larger size tunnels (or higher frequencies) implies to either include fading mitigating techniques for SISO systems or consider MIMO systems to benefit from rich multipaths.

Cross-sectional size also impacts EM polarization loss. Propagation losses for horizontal and vertical polarizations are relatively the same in tunnels with a square cross-section with aspect-ratio of 1 (aspect-ratio: ratio of longer dimension to the shorter one) [92]. However, in rectangular tunnels with larger width than height (horizontal aspect-ratio), horizontal polarization has less attenuation in the region far from the transmitter.

2.6.2.2 *Curvature, Junctions and Tilt*

At the UHF-band, curvature in tunnels introduces additional loss. This loss is dependent on frequency of operation, width of the tunnel, radius of curvature (Figure 2-15) and wave polarization. This loss is inversely proportional to the radius of curvature, and in contrast to straight tunnels, it is linearly proportional to frequency and width of the tunnel [109]. In curved tunnels, because the horizontal electric field is perpendicular to the curved walls, horizontally polarized waves are much more affected by the tunnel curvature than vertically polarized waves [13].

Junctions and bends change wave polarization. Therefore, unlike straight sections, inside the junctions/bends (or around the corners) waves are depolarized, and therefore received power around corners is usually independent of the receiver antenna's orientation [31]. The loss associated with one single corner is given in Table 2-2. As it can be seen, corner loss is smaller for lower frequencies. Additional corners add extra loss and increase the overall loss. Attenuation caused by corners in mine tunnels can be compensated for by adding 90^{o} reflectors to extend wireless propagation beyond the junctions and corners [110]. In most mine tunnels, walls are tilted about a vertical axis (tilt angle), which adds extra loss. Tilt loss becomes more significant as frequency increases [11], and therefore demands more precise analytical modeling at higher frequencies [111]. To precisely model pathloss and large scale fading, this loss should be included in total loss for tunnels with considerable tilt on sidewalls, floor or ceiling.

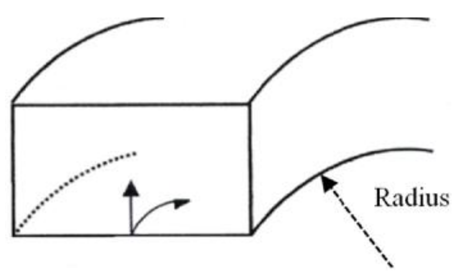

Figure 2-15 Radius of a curvature in a rectangular curved tunnel [13].

2.6.3 Surface Roughness

Underground mine tunnels have wide variations in wall roughness, often on the order of 20 cm [13]. However, unlike tilt and curvature loss in a straight empty tunnel, roughness loss becomes more significant at lower frequencies in tunnels owing to the larger grazing angle and higher number of bounces per unit length [11],[111].Therefore, this loss is insignificant at high frequencies (UHF and above) compared to tilt, curvature, corner and obstacle losses as Table 2-1 indicates.

2.6.4 Material and Infrastructure

Because infrastructure inside the tunnel changes EM properties of the tunnel, it is treated in the same section as the material from which the tunnel is dug.

2.6.4.1 *Material*

Electromagnetic properties of different materials are characterized by parameters such as relative permeability μ_r, dielectric constant ϵ_r and conductivity σ [106]. As shown in [11], Emslie *et al.* formulated the overall loss for UHF frequencies by assuming that the effect of ohmic loss is negligible due to the low conductivity of the surrounding material (coal) in coal mines. Conductivity of the coal at MF-band frequencies is 3×10^{-5}- 4×10^{-5} (S/m) and at 9 GHz is 0.12-0.73 (S/m) [106]. Dielectric constant of the coal at MF-band frequencies is 10-34, and at 9 GHz is 3.4-3.9, respectively [106].

Unlike permeability that for most rocks (except for rocks with a high concentration of metals of the ferromagnetic group) is very close to that of vacuum $\mu_0 = 4\pi \times 10^{-7}$ H/m, the dielectric constant and conductivity of rocks, are highly variable. Dielectric constants range from 2 to 70, but more frequently from 4 to 10 and conductivities range from 10^{-6} to 1 S/m. In general, both σ and ϵ_r increase with the water content and, as a general rule, σ increases and ϵ_r decreases with frequency [106].

In spite of the high variability of dielectric constant and conductivity of rocks, most recent studies such as [13],[70] show that walls' material does not significantly impact wireless propagation inside the mines, and as frequency increases (UHF and above), the material shows weaker impact. For WSN applications [86] however, material has been found to be an important element to consider in tunnel wirelss propagation. This can be due to the small spacing of sensors and tunnel walls. In practical deployments, wireless sensors are often attached to walls with an antenna to wall spacing of less than 10 cm. Nevertheless, compared to antenna position and frequency of operation, this study concludes that material has less impact on wireless propagation in tunnels. Unlike insignificant impact of material at UHF-band for TTA communications, at medium frequency (MF) for TTW and TTE communications, material has significant impact on wireless propagation. In TTE communications, earth is the medium for propagation, and in TTW communications, the skin depth in the mine's wall for the return current of the monofilar mode is the degrading factor. That explains why there are many theoretical and experimental studies on the effect of mine's material on early underground communications.

2.6.4.2 *Infrastructure*

Conductors such as power cables, water pipes, rails, *etc*. inside the tunnels, considerably change the electromagnetic properties of the tunnel, in particular for TTE and TTA communication [106]. Metallic air ducts or heating-ventilating- and-air-conditioning (HVAC) systems that are used to circulate air within the underground mining complex may enhance the wireless propagation. Additionally, ground support infrastructure, such as wire mesh screens, used to prevent rock from falling and the tunnel from caving-in can also affect wireless propagation. At corresponding frequencies, where the mesh netting interval is on the order of 0.1 free-space wavelengths, the attenuation for the dominant propagation mode can be reduced [112].

2.6.5 Vehicles and Other Obstructions

Heavy machinery, trucks, miners and other obstacles increase propagation loss and RMS delay spread in tunnels. This loss is dependent on the dimension of obstacles. Larger dimension vehicles cause additional shadowing loss [108]. In this case, propagation rays may only find their way behind the vehicle through multiple diffractions. This degrades signal power significantly [83]. In addition to power loss, obstacles increase RMS delay spread, and therefore a decrease in data rate can be seen in occupied tunnels. As shown in Table 2-3, in an experimental study, RMS delay spread was found to be less than 25 ns for a vacant tunnel and 103 ns for the same tunnel when occupied [92]. This demonstrates the influence obstructions have on delay spread. These results should be taken into account when deciding on transmit power, symbol rate, *etc*. for wireless transmission inside mines.

2.6.6 Antenna Placement, Gain and Polarization

The pattern and polarization of transmitter and receiver antennas greatly impacts wireless propagation in confined environment such as mines. As can be seen in Table 2-1, antenna insertion loss contributes significantly to the overall propagation loss for all of the studied frequencies. The importance of antenna parameters becomes more evident if multiple antenna systems are being used. In this case, not only the received power but also the decorrelation (or orthogonality) of antenna elements should be considered. Because there are no MIMO experimental studies in underground mines to date, some of the materials presented in this section are extracted from experimental studies of multiple-antennas in underground subway tunnels, which can help in predictions for employing MIMO systems in underground mines.

2.6.6.1 *Antenna Placement*

While the attenuation rate is mostly determined by the tunnel size and operation frequency (and not the location of the antennas), the power distribution among propagation modes is governed by the position of the transmitter antenna [70]. This can be valuable information for determining transmitter antenna position for different wireless systems with different objectives. For example, in single-input-single- output (SISO) systems, higher power can be achieved by positioning the transmitter antenna at the centre of the tunnel, while for MIMO systems, studies have shown that positioning the transmitter off-center of the tunnel crosssection would offer higher capacity [24].

Cross-sectional location of the antenna also impacts the radiation pattern by introducing additional loss [92]. Antennas designed for free-space may not perform well in underground mines because of the large number of strong reflections from the walls, this has been regarded as insertion loss (or coupling loss) that was priorly discussed. This effect is more noticeable for omni-directional antennas, such as dipoles, when they are located off-centered of the tunnel cross-section. In fact, omni-directional antennas perform better (more similar to their behavior in free-space) when they are in the middle of the tunnel.

It is also shown in [21] that alignment of the antenna array in MIMO systems plays a critical role. MIMO configurations perpendicular to the tunnel centerline or along a diagonal line, are found to be better than parallel to the tunnel centerline.

Locating the transmitter outside or inside of the tunnel affects the radiation pattern of the Tx antenna. When the transmitter antenna is inside the tunnel, its radiation pattern becomes sharper than its free-space radiation pattern (*i.e.*, radiation pattern that an antenna would have if it were in free space where there is no reflection, scattering and diffraction). This change does not depend significantly on the transmitter position along the tunnel. Conversely, when the transmitter is outside, the coupling loss between free-space and inside of the tunnel is dependent on the transmitter position. The coupling loss is considerably dependent on the angle of incidence too, if it is greater than 10^{o} with respect to the tunnel axis [82].

2.6.6.2 *Antenna Gain and Polarization*

When an omnidirectional antenna is located inside the tunnel, its effective radiation pattern becomes sharper than its free-space radiation pattern. Results in [110] show that a directional antenna located in the middle of the cross-section of the tunnel is a desirable choice for effectively transmitting power along the tunnel. However, locating the antenna in the middle of the tunnel may not be practical for most cases.

For SISO systems in tunnels, signal-to-noise-ratio (SNR) may be improved by employing a directional antenna and directing the antenna beam parallel to the centerline of the tunnel because it prevents signal scattering in LOS scenarios. However, in NLOS cases where propagation into the branches is dependent on multipath components, directional antenna may not be a good option.

For MIMO systems in which a rich scattering environment is beneficial (due to offering larger angular spread), directional antennas may not be a good alternative unless, as shown in [21] its beam-width is equal to the angular spread. Preliminary measurements in [21] have shown that the average value of the angular spread in a subway tunnel is around 60^o, which can be different in underground mines due to their smaller size, roughed walls and infrastructure. For horizontally polarized antennas, the tunnel width plays a more significant role as the reflection coefficients on the horizontal ceiling/floor are larger than those on the vertical walls. Likewise, the tunnel height is more significant for vertically polarized antennas [70]. In rectangular tunnels with larger width than height (horizontal aspect-ratio), horizontal polarization has less attenuation in the region far from the transmitter. This can be interpreted from Emslie's refraction loss formula for both polarizations, and its experimental verification in [107]. As a result, horizontally polarized antennas are more appropriate in wide but short tunnels, and vertically polarized antennas are more appropriate for tall tunnels [70]. In addition, for a tunnel with horizontal aspect-ratio (width: 4.2 m, height: 3 m) the RMS delay spread is larger for horizontal polarization (13.5 nsec) compared to vertical polarization (5.49 nsec) [71]. Different RMS delay spreads are caused by different attenuation constants for the two polarizations. The lower attenuation of the horizontally polarized signals makes the power-delay-profile spread [71].

As it was seen in this subsection, optimizing antenna performance in tunnels remains an open topic for future studies. Better performance can be accomplished through careful design of customized antennas that are matched to the tunnel environment. In Table 2-6, significant results and implications useful for wireless system design have been presented. This table demonstrates how operation frequency, physical parameters of tunnels and antenna properties affect two main channel impairments; power loss and RMS delay spread. (parts left with ‘NA’ (not-available) representing cases that have not studied to date, or no information was available).

Table 2-6 Key implications for wireless system design at UHF-band in underground mines.

<table>
<tr><th colspan="2"></th><th>Loss / Attenuation</th><th>RMS delay spread</th><th>Reference</th></tr>
<tr><td rowspan="3">Tunnel Geometry</td><td>Cross-sectional size (similar impact as frequency)</td><td>Larger size at a fixed frequency (or higher frequency in a fixed cross-sectional size)
shows higher pathloss exponent in LOS scenario</td><td>Larger size at a fixed frequency (or higher frequency in a fixed cross-sectional size)
shows smaller RMS delay spread</td><td>[75]</td></tr>
<tr><td>Curvature/ corner/ branch</td><td>Increase
(more significant at higher frequencies)</td><td>Increase</td><td>[55],[71]</td></tr>
<tr><td>Wall tilt</td><td>Increase
(more significant at higher frequencies)</td><td>NA</td><td rowspan="2">[11],[55]</td></tr>
<tr><td colspan="2">Wall roughness</td><td>Increase
(more significant at lower frequencies)</td><td>Increase</td></tr>
<tr><td colspan="2">Wall material</td><td>No significant impact</td><td>No significant impact</td><td>[13],[70]</td></tr>
<tr><td colspan="2">Obstructions</td><td>Presence of obstruction results in higher loss</td><td>Presence of obstruction results in larger RMS delay spread</td><td>[71]</td></tr>
<tr><td rowspan="3">Antenna properties</td><td>Cross-sectional placement</td><td>Centre of the tunnel shows lower loss compared to off-centre</td><td>Centre of the tunnel shows larger RMS delay spread compared to off-centre</td><td>[70]</td></tr>
<tr><td>Radiation pattern (gain)</td><td>Directional antenna shows lower coupling loss compared to omni-directional one in LOS</td><td>Directional antenna shows smaller RMS delay spread compared to omni-directional one</td><td>[11],[94]</td></tr>
<tr><td>Polarization</td><td>Mine tunnel with horizontal aspect-ratio shows lower loss for horizontally polarized waves</td><td>Mine tunnels with horizontal aspect-ratio show larger RMS delay spread for horizontally polarized waves</td><td>[12],[50]</td></tr>
</table>

2.7 Conclusions

The need for wireless communication in the underground mining industry has evolved from basic emergency signaling, to person-to-person voice communication and to high speed real-time data transmission. Accordingly, the supporting technologies have emerged from through-the-earth transmission, to radiating cables, to point-to-point and multipoint radios. Applications utilizing these technologies include voice communication, video surveillance, tele-operation of mining equipment (tele-mining), wireless sensors networks, geo-location and tracking of personnel and assets. To develop and evaluate these technologies appropriately, wireless propagation and channel models are essential. Measurement and theoretical approaches to channel modeling are increasingly seen as complementary; many channel modeling studies employ both methods.

Analytical and numerical models based on waveguide theory, geometrical optical ray-tracing and other methods have been developed by many researchers. While the single-mode waveguide model is simpler and requires fewer inputs about the physical environment, it is not very effective in predicting propagation for near-field and too short tunnels with complex geometries at higher frequencies. Ray-optical models on the other hand, provide more detailed prediction for higher frequencies and complex geometries at the price of requiring detailed information about the physical environment, and computational burden which increases significantly if the area under study is prolonged. A recent theoretical model, multimodewaveguide, offers more accurate and realistic model with reasonable runtime, which can also characterize small-scale fading statistics. The main advantage of this model is the ability to accurately characterize both the near-zone and farzone of the tunnel.

Experimental studies on the other hand, provide readily usable parametric values but are site specific and their statistical generalization requires extensive measurement campaigns in the underground mines. Measurement results in different frequency bands (*e.g.*, VHF, UHF and SHF) have been presented by several researchers, mostly covering narrowband transmission. Some limited wideband and UWB studies in UHF and SHF bands have been conducted. With the increasing interest in low-power sensor networks and batterypowered access points, the availability of UWB transmission technologies and the transition towards even higher, millimetre wave frequencies for indoor applications, the need for further theoretical and experimental studies in underground mines is imminent.

Some implications of wireless communication design have been discussed in this article, which are interpreted from the previous studies. Open research areas for future investigation include characterization of frequencies above 10 GHz, incorporation of more complicated mine geometries in existing waveguide and ray-optical models, antenna configuration design and development of channel models for MIMO systems, design of optimum wireless mesh networks, channel modelling for body-area-networks, and *etc*. The results of these studies facilitate the employment of new technologies by the mining industry that ultimately improves work safety, productivity and efficiency in mines.

CHAPTER 3: MIMO EXPERIMENTAL SETUP AND DATA COLLECTION

3.1 Introduction

In this chapter, we describe the channel sounder we have developed and used throughout our experimental study. Both the measurement hardware and software that we used to collect the data and the method that we used to calibrate the setup are presented and explained. This channel sounder is capable of collecting data for both MIMO and UWB measurements.

3.2 Development of a MIMO Channel Sounder

In this section, we briefly describe the UWB-MIMO channel sounder that we developed for our MIMO measurements in the Radio Science Lab (RSL). It includes both the channel sounder hardware and the data acquisition software. Because in parallel to our MIMO study, another project concerning UWB channel modeling in underground mines was underway, this channel sounder was developed so that it can collect both UWB and MIMO data at the same time.

3.2.1 MIMO Channel Sounder Hardware

MIMO channel sounders generally fall into two categories: those based on real arrays and those based on virtual arrays. In a real-array-based channel sounder, all N_{Rx} receiving antennas (and possibly all N_{Tx} transmitting antennas) are present and used simultaneously. In a virtual array-based channel sounder, a single transmitting antenna and a single receiving antenna are moved to each of the locations at which a MIMO antenna element would be installed and individual channel responses are measured sequentially. This has several advantages: (1) mutual coupling between antenna elements is absent and (2) only one RF chain is required. However, the measurement environment should be static. The condition of having a static environment was met in both the service tunnel and the Myra Falls underground mine measurements. Both the service tunnel at UBC and level 23 of the Myra Falls underground mine where we conducted the measurement were vacant, and there was no movement.

For simplicity as well as versatility, we decided to build a virtual array-based MIMO channel sounder. The basic MIMO measurement setup (without fibre-optic cable) can be used for distances of up to 20 m. The principal limitation is the loss and phase distortion introduced by overly long coaxial cables. Possible approaches for extending the channel sounding range are using expensive phase-stable coaxial cables, and/or phase-locked remote signal generators. However, none of these options is easily scalable for ranges varying from tens of metres to a few kilometres.

We extended the measurement range of our channel sounder to a few hundred metres by incorporating a Miteq RF-over-fibre unit into the transmit side. Compared to coaxial cable, fibre optic cable is also much less susceptible to phase distortion due to cable torsion and flexion and incurs far less path loss. A block diagram of the measurement setup and the measurement specifications are given in Figure 3-1 and Table 3-1, respectively.

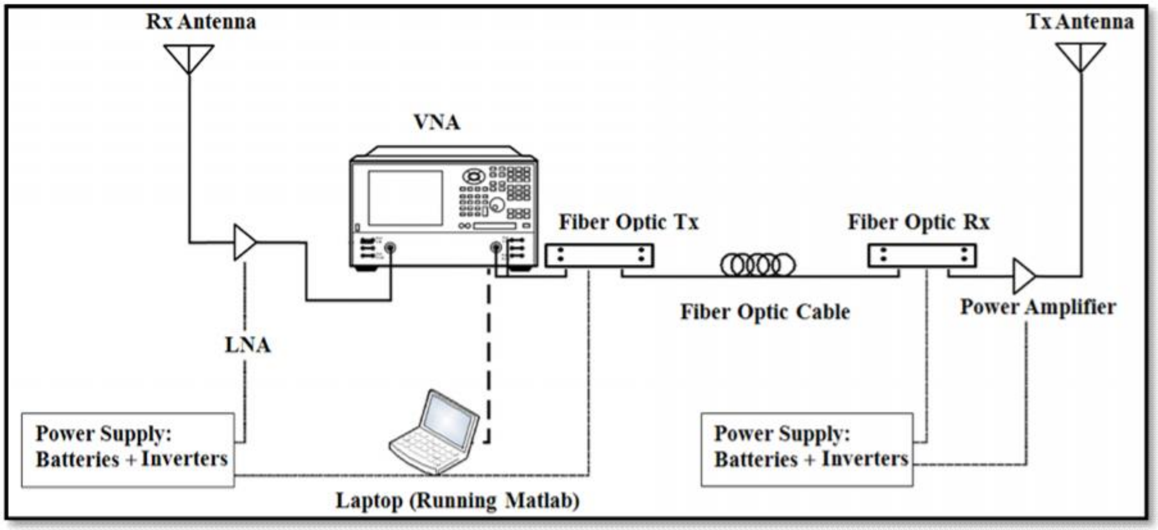

Figure 3-1 Block diagram of the measurement setup.

Table 3-1 Measurement specifications

Unit	Specification
VNA master	Anritsu MS2034A
Frequency band Number of frequency points	2.49 - 4 GHz 551
Antenna	Electrometrics UWB Biconical antennas
Positioner Tx power	Velmex linear xy-positioner 26 dBm
Grid point spacing	2λ at 2.49 GHz
Dynamic range Power amplifier Fibre optics	120 dB Ophir - Model 5303075 Miteq SMCT-100M11G

Measurement setup consists of an Anritsu MS2034A master vector network analyzer, two antennas (Biconical for UWB measurements), coaxial cables, two Velmex bislide xy-positioners with motor controllers, two USB-to-serial adapters, a laptop-based instrument controller running MATLAB and three carts to carry: (1) Rx positioner and VNA, (2) Tx positioner and Fibre Optic spool and (3) power supply (inverters and batteries).

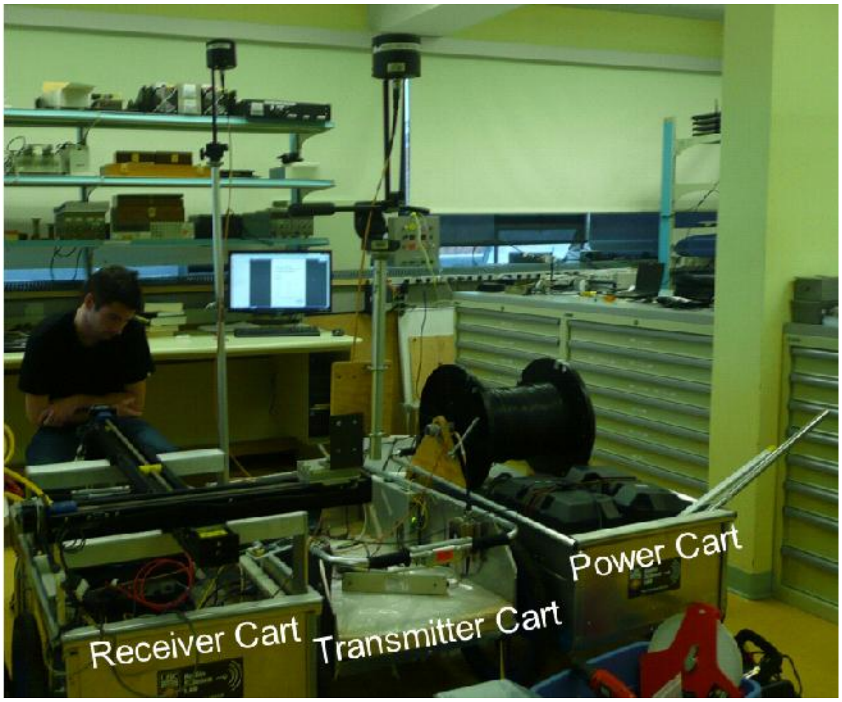

Figure 3-2 MIMO Measurement equipment in RSL.

A MATLAB program is used because of its post processing and peripheral communication abilities. It supports the general-purpose-interface-bus (GPIB) functionality. GPIB is the interface between the laptop and general purpose-network -analyzer (PNA). It is a widely used industrial interface between instruments. Here, it serves as a link between the laptop and PNA for sending and reading data or commands. After the GPIB connection is established, the command that tells PNA what to do needs to be sent. The standard-commands-for-programmable-instruments (SCPI) command format is used here.

In order to make the channel sounder self-contained and easy to transport, we mounted the equipment together with storage batteries and a true-sine-wave inverter in two aluminium carts that are equipped with 0.5 m pneumatic tires. Before conducting our development run in the mine, we calculated the link budget, calibrated the measurement equipment and performed some tests in a hallway of the MacLeod building at UBC in order to ensure that the whole system functions correctly.

For UWB-MIMO measurements in both the UBC service tunnel and the Myra Falls underground mine, we used Biconical antennas which have 3.3 dB gain difference in its pattern for frequencies under the study, 2.49 GHz - 4 GHz (-1.9:1.4 dBi). This gain difference does not impact our narrowband MIMO analysis.

3.2.2 Calibration of the Channel Sounder

In order to cancel the effect of different electrical components such as cables and amplifiers in the circuit, a calibration procedure should be performed. There are different ways to perform the calibration; the most accurate one is full 12-term error correction. Because the RF over fibre link is uni-directional, we cannot perform a full 12-term error correction. Moreover, due to limitations imposed by the VNA firmware, we cannot perform six-term error correction (impedance of port 1 and forward gain). Therefore, we chose frequency response correction for the calibration, as shown in Figure 3-3.

After calibration is finished and saved, cables can be disconnected from the bullet connector, and can be reconnected back to antennas respectively.

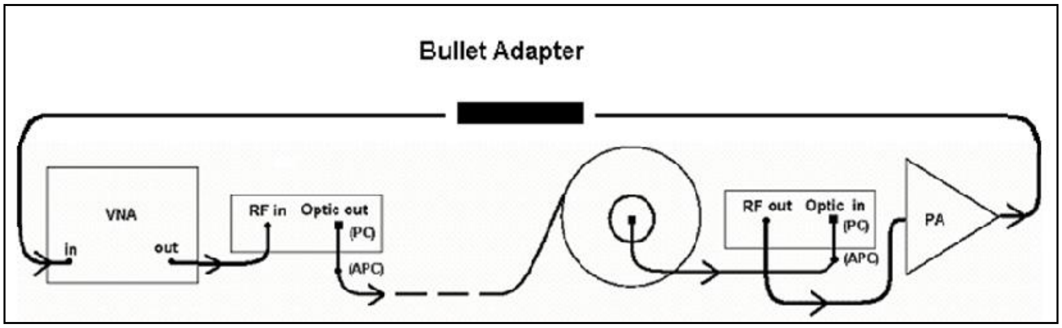

Figure 3-3 Connection diagram for calibration.

3.2.3 MIMO Data Acquisition Software

As aforementioned, a MATLAB script that runs on the laptop-based controller controls the MIMO channel sounder. During a typical measurement, the transmitting antenna is horizontally translated to one of the N_{Tx} transmitting grid points and then channel frequency response data is collected after the receiving antenna is relocated to each of the N_{Rx} receiving grid points. The process is repeated N_{Tx} times.

The complete measurement procedure as shown in Figure 3-4 can be summarized as follows: (1) Set the measurement parameters such as start and stop frequencies, number of sample points, IF frequency and RF transmit power. (2) Initialize the xy-positioners: (a) open a communication link between the computer and positioner, (b) send commands to move the positioner to its starting position which will be used as the origin reference. (3) Initialize the PNA to clear the PNA of its current settings and then load it with new settings. (4) Perform the measurement by: (a) move the positioners and acquiring frequency response data at all of the receiving grid points and (b) send the data from the PNA to the laptop and saving them for future processing. (5) After data has been collected for all possible combinations of transmitting and receiving grid points, end the program, close the PNA and reset the xy-positioner.

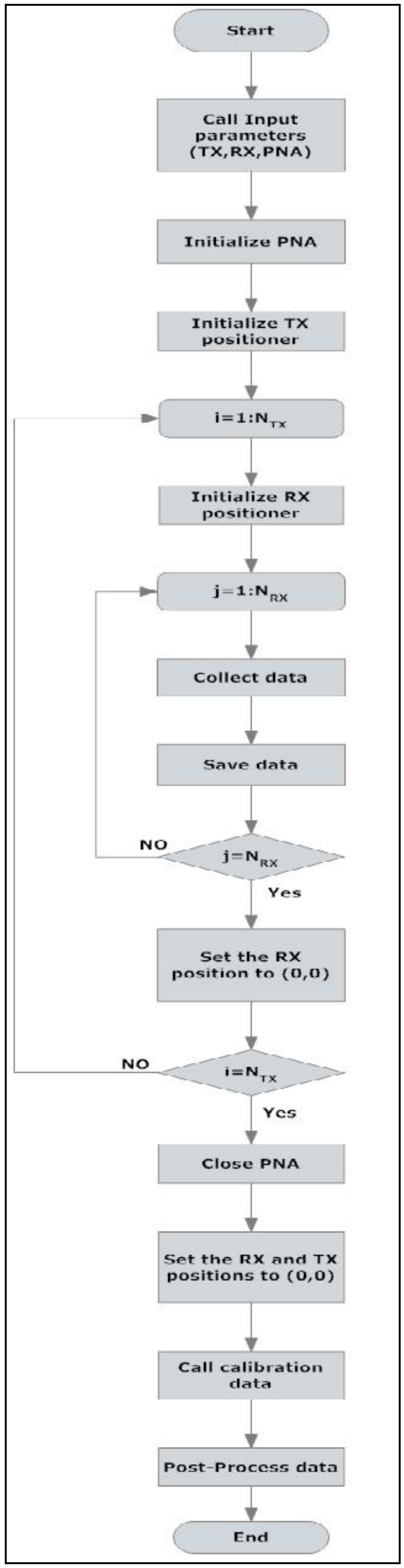

Figure 3-4 Flowchart of the UWB-MIMO channel sounder software

CHAPTER 4: EFFECT OF ANTENNA CONFIGURATION ON MIMO-BASED ACCESS POINTS IN A SHORT TUNNEL

4.1 Introduction

Access-point-to-access point (AP-AP) communication is needed in underground mines to extend wireless coverage to high traffic work areas of the mine such as the face area. The face area is usually where the largest number of miners works and where the greatest demand for wireless communication systems exists in underground mines. In recent years, considerable effort has been devoted to characterizing conventional single-antenna wireless channels in underground mine environments [113],[114]. These efforts have supported replacement of legacy leaky feeder systems that provide basic voice communications by cellular telephony (in the range 0.8 GHz -2.1 GHz) and, most recently, by conventional wireless LAN technology (in the range 2.4 GHz -2.5 GHz) that provide integrated voice and data communications. While the new systems perform well, further improvements in coverage, throughput and reliability are required in order to support future applications such as mine automation and tele-operation of mining equipment.

In this regard, multiple-input-multiple-output (MIMO), a compelling new technology that multiplies data throughput, coverage and reliability without consuming extra transmit power and radio frequency spectrum [6],[115] seems to be a perfect response to this demand. However, the mining industry is hesitant to adopt new wireless technologies such as MIMO, as there are many uncertainties about the performance and deployment strategies. Their concern is valid because standardized off-the-shelf products, such as IEEE-802.11n systems (multiple-antenna technology), are designed and tested for conventional indoor and outdoor environments, and therefore are not necessarily suitable for underground mine tunnels with different propagation behavior. In fact, the performance of such products is highly dependent on the radio channel which includes the surrounding propagation environment and the antenna configurations at both ends. This is even more evident for confined environments where objects are located at closer distances to the antennas.

A large number of experimental and analytical studies have been conducted to determine the best antenna solution for conventional indoor and outdoor environments [18],[116],[117], resulting in various configuration designs for multiple-antenna systems. Conversely, not much research has been conducted on MIMO channel modeling and antenna configuration designs for underground tunnels, such as subways and underground mines, which have distinctive waveguide behavior. There are some theoretical MIMO studies based on modal analysis, and limited number of experimental MIMO studies has also been performed for rectangular [24] and arched [21],[118],[119] long subway tunnels. These studies mainly focus on the 900 MHz frequency band considering practical application of GSM-R standard for railway communications and derived works in Europe. In [21], the authors have studied and compared three array orientations and configurations with fixed spacing for AP to mobile communications, where a mobile antenna is installed on the train windshield. They have shown that in subway tunnels, array orientation impacts MIMO performance, and within a certain distance from the Tx, MIMO capacity growth is achievable in spite of low angular spread imposed by the tunnel geometry [21].

While yielding useful insights about MIMO performance in long and large tunnels, these findings fail to predict the performance of MIMO systems operating in other frequencies and employing with other antenna orientations, configurations and locations that might be more convenient to be used for AP communications inside the underground mine tunnels. More importantly, they cannot directly be applied to underground mine tunnels due to their differences in size, branches, and extensive infrastructure they often have.

A more recent study, which is theoretical and is based on modal analysis, aims to maximize the capacity by optimizing only the number and position of MIMO antennas for underground tunnels [120]. This has been done by allocating MIMO subchannels to high power eigenmodes. The authors however, have not elaborated on practical considerations of antenna array design, deployment and practical implications. The optimum position they found for the antenna is in the middle of the tunnel cross-section, which may not be practical. Moreover, this study is purely theoretical, is only for a straight tunnel, and therefore cannot capture all the detailed geometry of an underground tunnel with extensive infrastructure.

In addition to purely theoretical studies for general cases, we believe more realistic scenarios need to be studied using comprehensive simulation or measurement data that capture details of the propagation environment. Because conducting MIMO measurements for various antenna configuration scenarios is very time consuming and difficult due to limited access to the underground mines, we chose to use ray tracing method to assess various configurations. Ray tracing simulation additionally allows: (1) assessment and comparison of study cases which are difficult to be studied by measurement or theoretical modeling, *e.g.,* the effect of infrastructure, (2) visualizing and obtaining physical insights by observing the rays' interaction with the surrounding environment.

Accordingly, for this study, we chose to carefully simulate an underground service tunnel which has the same size as of a typical mine tunnel with a long section (103.5 m), a branch, and extensive infrastructure. These features can more realistically characterize typical underground mine tunnels while facilitate assessment of the research tool by allowing us to perform both simulation and measurement in an environment, where unlike underground mines, is easy to access. We used Wireless Insite ray tracing software (by Remcom Inc.) to assess the performance of the MIMO antenna configurations. After selecting the best performing configurations by ray tracing method, we have experimentally validated the simulation results by conducting MIMO channel sounding in the service tunnel.

The remainder of this chapter is organized as follows: In Sec. 2, we describe our simulation setup and scenarios. In Sec. 3, multiple antenna analysis that has been used for our study is given. In Sec. 4, we present simulation results and discussions. In Sec. 5, we validate simulation results with measurement. Finally, in Sec. 6, we conclude the chapter by summarizing our key findings and their implications.

4.2 Simulation Setup and Scenarios

In this section, we describe the geometry of the site chosen for the study and also explain how we carefully construct the service tunnel with its detailed structure in a ray-tracing program.

4.2.1 **Chosen Site**

The chosen underground tunnel located underneath the Woodward Instructional Resources Center at University of British Columbia, is a suitable site considering its size, ease of access, long and narrow pathways, and rich infrastructure. The entire structure of the underground tunnel resembles a general cross-shape with a total length of 103.5 m and a width of 55.7 m. The widths of the tunnel substructure vary from 2.7 m (main tunnel) to 6.8 m (branched tunnel) with almost same height of 2.4 m throughout the entire structure (Figure 4-1).

To accurately model this tunnel, a 3D floor plan of the tunnel, the properties of all the structures such as thickness, permittivity, conductivity, reflection, and transmission coefficients needed to be matched to the corresponding prototypes in the physical tunnel. Specifications for the materials used for walls and galvanized pipes are presented in Table 4-1. Sidewalls and ceiling were assumed to have same dielectric material, while metal doors were considered perfect-electric-conductors (PEC).

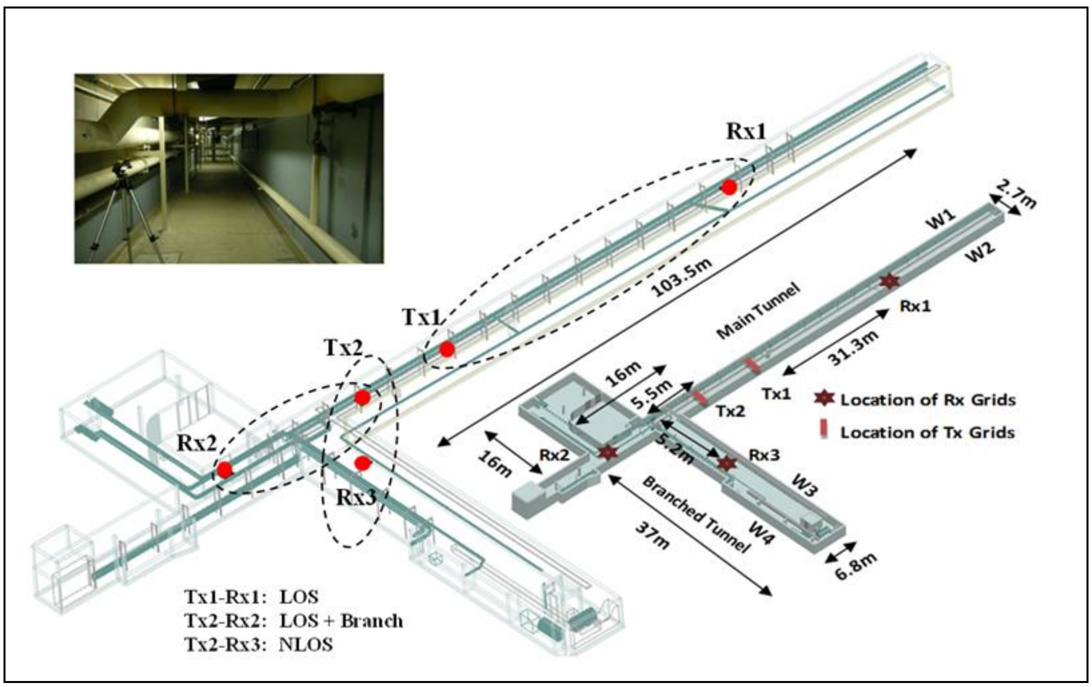

Figure 4-1 UBC Woodward service tunnel constructed in Wireless Insite with its extensive infrastructure and considering 3 propagation scenarios.

Table 4-1 **Specifications of the main structures used in the Wireless Insite simulations.**

	Electrical Properties		
	σ_a (S/m)	ε_r	Thickness (m)
Concrete Walls	0.015	15	0.3
Pipes	16	3.1	0.003

4.2.2 Software and Parameter Restriction

To accurately construct the floor plan with extensive rounded pipes, we found it more convenient to create the floor plan and infrastructure by making the tool file itself rather than importing them from AutoCAD or SolidWorks 3D software into the ray-tracing software. To draw round pipes, we had to draw polygon patterns with the maximum allowable sides to mimic circular shape because WI cannot recognize the circular pattern. Also, to effectively draw the pipes with the appropriate side number, we had to find out the minimum length recognizable by the ray-tracing tool.

As a rule of thumb, the minimum length restriction is the wavelength of operation frequency. Nevertheless, we performed a benchmark testing with different pipe edges to find the exact cutoff geometry length before the infrastructure is not detectable by the ray-tracing tool; it was found to be 4 cm. As a result, all dimensions in the simulation, including the polygon cross-sections of the pipes, were constructed with slightly larger edge length than the cutoff geometry length (4 cm) to closely resemble the original shape of the pipes while remaining visible to the ray-tracing tool. Careful construction of the floor plan and infrastructure made our simulation substantially accurate, however it required large memory and long run time due to large number of facets interacting with the shot rays.

4.2.3 Simulation Scenarios

Based on preliminary results, we found that a 4×4-ULA (*i.e.*, 4-element linear array at the Tx and 4-element linear array at the Rx) configuration offers higher capacity compared to 4×4-square one (*i.e.*, 4-element square array at the Tx and 4-element square array at the Rx). Therefore, 4×4-square MIMO scenario was excluded and for further analysis, study was narrowed down to 4×4-ULA configurations. For our study, we considered typical propagation scenarios which are more common in underground mines such as: (1) pure LOS link between the Tx and Rx inside a long tunnel, (2) LOS link with a branch in the middle, and (3) NLOS link with the Tx in the main tunnel and the Rx in the branched tunnel. These three propagation scenarios are illustrated in Figure 4-1.

Among various antenna configurations and deployments, we have chosen the ones that are practical and convenient to be used in underground mines. Accordingly, MIMO AP antennas are either placed close to the sidewalls or under the ceiling. The distance of the antennas from ceiling and sidewalls were kept more than a wavelength (about 12.5 cm). For each propagation scenario, we have considered several antenna configurations (differing in antenna polarization and array orientation) and deployments, which are summarized in Table 4-2. Antenna radiation pattern is assumed to be omnidirectional at the Tx and Rx.

For array orientation parallel to the tunnel width, "*x*", parallel to the tunnel height, "*y*", and parallel to the tunnel axis, "*long*" (or longitude), have been chosen. For Rx1 and Rx2 grids, "*x*", "*y*", and "*long*" belong to the main tunnel, while for the Rx3 grid they belong to the branched tunnel. For vertical polarization, antennas are placed parallel to the tunnel height, while for horizontal polarization they are placed parallel to the tunnel width.

Except for the deployment scenario 4 that has been considered at Rx1 grid location only, other six scenarios have been studied at all three Rx grid locations (Rx1, Rx2, and Rx3).

Table 4-2 Different antenna configuration and deployment scenarios (*x*: parallel to the tunnel width, *y*: parallel to the tunnel height, *long*: parallel to the tunnel axis, H: horizontal polarization and V: vertical polarization).

	Sc1 (long-V) Tx, Rx: opposite sidewalls	Sc2 (long-H) Tx, Rx: opposite sidewalls	Sc3 (tr-y-V) Tx, Rx: opposite sidewalls	Sc4 (tr-y-$H_{smaewall}$) Tx, Rx: same wall only at Rx1	Sc5 (tr-y-H) Tx, Rx: opposite sidewalls	Sc6 (tr-x-V) Tx, Rx: under ceiling	Sc7 (tr-x-H) Tx, Rx: under ceiling
Tx antenna polarization	V	H	V	H	H	V	H
Rx antenna polarization	V	H	V	H	H	V	H
Tx Array orientation	*long*	*long*	*y*	*y*	*y*	*x*	*x*
Rx Array orientation	*long*	*long*	*y*	*y*	*y*	*x*	*x*

To make it easier to visualize the antenna scenarios, Figure 4-2 is presented. In all cases, there is a grid of antennas at the Tx (5×3) and a grid of antennas at the Rx (5×5). Depending on the scenario under study, different Tx and Rx array orientations from the grids have been chosen during the post processing. From the output files of ray tracing simulations, we have constructed sixty 4×4-**H** matrices for each antenna configuration.

Due to interference from wireless LAN transmissions from upper floors, the 2.4-2.483 GHz frequency band could not be used for the MIMO measurement in the service tunnel, therefore, 2.49 GHz was considered. We set the transmit power to 0 dBm and number of received rays by each antenna element at receiver to 50. The upper limit number of reflections and diffractions in each propagation path is set to 30 (maximum value) and 0, respectively. Number of diffractions was set to zero because our preliminary results showed that including diffraction does not significantly change the results, while dramatically increases the computation time.

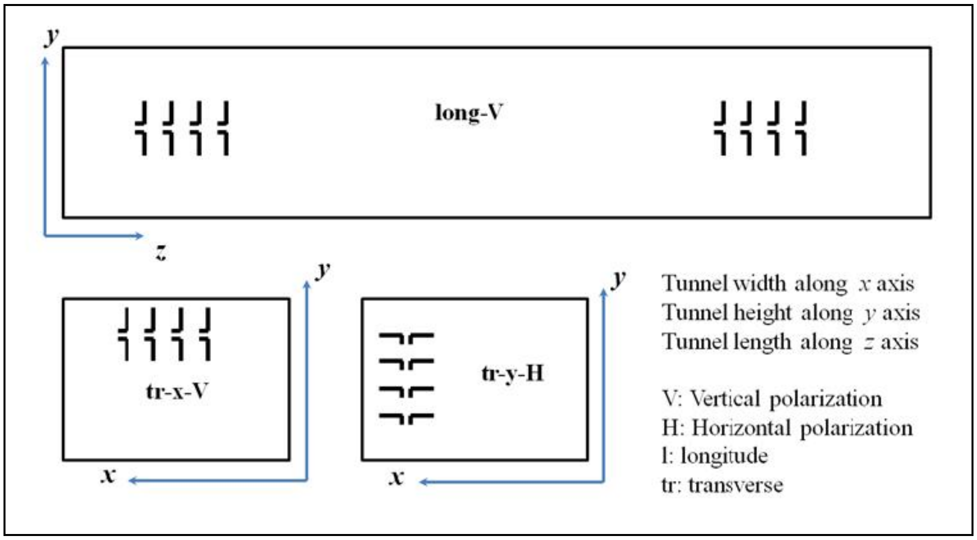

Figure 4-2 Antenna configuration scenarios used in this study (V: vertical, H: horizontal).

4.3 Multiple Antenna Analysis

In this section, formulas and analysis that have been used for the multiple antenna study are presented.

4.3.1 Minimum Interelement Separation

To determine suitable interelement separation, the correlation coefficient of neighboring elements at the Rx was studied. Because the highest correlations correspond to successive elements, we chose Pearson's correlation coefficient of successive elements (m, n) at Rx grids for every Tx element (p) as follows:

$$\rho_{hmp,hnp} = Corr\left(h_{mp}, h_{np}\right) = \frac{E\left[\left(h_{mp} - \mu_{hmp}\right)\left(h_{np} - \mu_{hnp}\right)\right]}{\sigma_{hmp}\sigma_{hnp}} \qquad (1)$$

where h_{mp} and h_{np} are channel gain matrix entries corresponding to *mp* and *np* subchannels, and also μ and σ represent mean and standard deviations, respectively.

4.3.2 Normalization Factor

While working on MIMO systems, one of the difficulties is that channel capacity depends on the scaling of the **H**-matrix. Because in design of MIMO antennas or coding schemes absolute value of the scaling factor is not necessary, common practice is to normalize **H**-matrices so that the average SNR at the receiver elements is set to a fixed value and can be adjusted as a parameter. In order to perform a fair comparison of different systems or schemes, it is required to consider the same normalization factor sometimes. Here, two normalization factors are considered to compare performance of the antenna configurations, depending on whether the objective is to study: (1) the effect of subchannels' correlation only, or (2) both correlation and power impact on the capacity. For normalization 1, every **H**-matrix is normalized by its own Frobenius norm which is the RMS value of the elements of a matrix and calculated as follows [6]:

$$\begin{aligned} \mathbf{H}_{\text{nor}} &= \mathbf{H}\sqrt{\frac{N_{Tx}N_{Rx}}{\|\mathbf{H}\|_F^2}} \\ \|\mathbf{H}\|_F &= \sqrt{\sum_{i=1}^{N_{Rx}}\sum_{j=1}^{N_{Tx}}|h_{ij}|^2} \end{aligned} \tag{2}$$

where $\mathbf{H}$, N_{Rx}, N_{Tx} and h_{ij} are channel coefficient matrix, number of Rx antennas, number of Tx antennas, and channel matrix entries, respectively. Normalized **H**-matrices obtained by this method are only affected by the level of correlation experienced at the antennas.

Normalization 2 is often used for fair comparison of different MIMO antenna configurations [24],[121]. This normalization method, which is also called global channel normalization [122] not only includes subchannels' correlation but also their power contribution, which is different for each antenna configuration. For this normalization method, a common normalization factor is considered for all scenarios under comparison, which is calculated based on averaging Frobenius norms of **H**-matrices of all cases being compared. Considering K total channel realizations at each transmitter location, this normalization can be calculated as follows:

$$\mathbf{H}_{\text{nor}} = \mathbf{H}\sqrt{\frac{KN_{Tx}N_{Rx}}{\|\mathbf{H}\|^2}}$$
$$\|\mathbf{H}\| = \sqrt{\sum_{k=1}^{K}\sum_{i=1}^{N_{Rx}}\sum_{j=1}^{N_{Tx}}\left|h_{ij}\right|^2} \tag{3}$$

After finding normalized **H**-matrices, capacity C (in bit/s/Hz) of a MIMO system with N_{Tx} transmitting antennas and N_{Rx} receive antennas can be calculated by [6]:

$$C = \log_2\left[\det\left(\mathbf{I}_{N_{Rx}} + \frac{SNR}{N_{Tx}}\mathbf{H}_{\mathbf{nor}}\mathbf{H}^{*}_{\mathbf{nor}}\right)\right] \tag{4}$$

where $*$ denotes the transpose-conjugate, $\mathbf{H}_{\mathbf{nor}}$ is the $N_{Rx}\times N_{Tx}$ normalized channel matrix, SNR is average signal to noise ratio and **I** is identity matrix. It is assumed that the N_{Tx} sources have equal power and are uncorrelated. CDFs of channel capacity for different scenarios have been obtained assuming average SNR=20 dB.

4.4 Simulation Results and Discussions

In this section, simulation results are presented, discussed, and accompanied by physical interpretation. Based on the results, antenna interelement separation and antenna configurations that offer high performance are identified. To study the impact of tunnel infrastructure, the results are compared for the tunnel with and without the infrastructure. The outcome of this section can be useful in developing guidelines to design and deploy MIMO array configurations in underground mines.

4.4.1 **Antenna Interelement Separation**

To quantify the correlation among the MIMO subchannels, which determines suitable interelement separation, we computed the correlation coefficient of successive elements based on equation (1) for different interelement separations at the Rx for different scenarios (with and without infrastructure). We have tabulated the result for horizontal array with vertically polarized antenna in Table 4-3.

From Table 4-3, we can see: (1) $\lambda/2$ separation which is a typical antenna separation for most MIMO off-the-shelf products shows high correlation and (2) correlation between successive elements is higher for with infrastructure case compared to without infrastructure case. Observation (2) is relatively unexpected, because one might expect to see decrease in the level of subchannels' correlation after including the infrastructure. Our simulations have shown that although infrastructure inside a tunnel may increase the number of multipaths, it increases correlation of neighboring elements, and degrades channel capacity (as we will see in the following section).

Both ray tracing and waveguide modelings can explain this result. Considering the ray tracing modeling, this can be due to the fact that key rays between Tx and Rx, which contribute in forming decorrelated subchannels have been blocked by the infrastructure. On the other hand, considering the waveguide theory this result can be attributed to the waveguide mode suppression that has occurred due to the presence of the infrastructure. This decreases decorrelation of orthogonal waveguide modes present in an empty rectangular tunnel. Based on Table 4-3, by choosing antenna separation of 2λ, correlation of less than 0.5 can be achieved for both cases of the tunnel with and without infrastructure, and therefore, for further analysis we chose 2λ interelement separation.

4.4.2 Array Orientation and Antenna Polarization

In this section, the objective is to assess and compare the antenna configurations with different array orientations and antenna polarizations for different propagation scenarios in the tunnel with and without infrastructure, and also to select two antenna configurations which show closest capacity CDF to that of an i.i.d. Rayleigh fading channel. Here, to obtain and compare channel capacity for different scenarios, power impact of each antenna configuration is included. This has been performed by normalizing all the **H**-matrices at each Rx grid location with a common normalization factor (global normalization).

Table 4-3 Correlation coefficient of neighboring elements at Rx with different interelement separations (V: vertical, H: horizontal polarizations).

			λ/2	λ	3λ/2	2λ
With Infrastructure	LOS	V	0.69	0.35	0.23	0.24
		H	0.83	0.58	0.34	0.13
	NLOS	V	0.80	0.63	0.57	0.49
		H	0.76	0.55	0.45	0.39
Without Infrastructure	LOS	V	0.47	-0.09	-0.22	-0.19
		H	0.82	0.51	0.14	-0.18
	NLOS	V	0.51	0.09	0.03	0.13
		H	0.40	0.01	0.04	0.10

4.4.2.1 *Tunnel without Infrastructure*

Figure 4-3 compares the antenna configurations for different propagation scenarios in the empty service tunnel. As the results show, the antenna configurations perform very differently, confirming significance of antenna configuration design in linear confined spaces. The different performance is particularly more evident in Rx1 scenario where arriving rays are more concentrated compared to the other scenarios (Rx2 and Rx3).

As can be seen from Figure 4-3, the tr-x-V and tr-y-H configurations at Rx1, and tr-x-V configurations at Rx2 and Rx3 shows the closest capacity CDF to that of an i.i.d. Rayleigh fading channel. It is interesting to note that based on the waveguide theory, these two antenna configuration would be equivalent if: (1) the tunnel aspect ratio is equal to one (*i.e.*, width and height have the same size), (2) the material of all the walls is the same, and (3) the distance of the arrays from the wall (or ceiling) is equal for each scenario (tr-y-H and tr-x-V). In our study, however, tunnel width is larger than the tunnel height, and also arrays' distance from the wall (or ceiling) is not the same. Due to practical constraints, array distance from the ceiling in tr-x-V scenario is larger than array distance from the sidewall in tr-y-H scenario.

Higher performance of tr-x-V configuration compared to tr-y-H configuration can be due to two main reasons. First, the tr-x-V array is placed closer to the center of the cross-sectional plane. When the antenna is placed closer to the center of the cross-sectional plane, energy coupling from the antenna to the waveguide will be stronger. Therefore, tr-x-V configuration has higher power compared to tr-y-H configuration. Second, tr-x-V configuration has larger angular span (in azimuth plane, φ-plane) compared to tr-y-H configuration (in elevation plane, θ-plane), because the tunnel width is larger than the tunnel height. This can result in lower correlation among the MIMO subchannels in tr-x-V configuration.

Comparing tr-y-H$_{(same\ wall)}$ and tr-y-H (or tr-y-H$_{(oppwall)}$) deployments at Rx1 show that although strongest rays in tr-y-H$_{(same\ wall)}$ scenario has higher power compared to the tr-y-H, as can be seen from Figure 4-3, tr-y-H configuration shows higher capacity. Observation of the rays explains this result by showing that the Tx and Rx arrays in tr-y-H scenario are more exposed to each other and the walls (due to their relative position), and thus larger number of rays can be generated between the Tx and Rx in tr-y-H5$_{(oppwall)}$. Back walls and in some cases infrastructure can also increase the Tx and Rx interaction.

At Rx2, tr-x-V shows significantly better performance compared to the tr-y-H configuration, which is not what one may expect considering the impact of the branch in the middle of the transmitter and Rx2. The branch allows some of the propagation rays in the main tunnel to escape into the branch tunnel. This can be even more severe for configurations with vertically polarized antennas that mainly use sidewalls to propagate. Results at Rx3 confirm this fact by showing higher channel capacity for the tr-x-V configuration and two other configurations with vertically polarized antennas (long-V and tr-y-V).

The reason for high capacity at Rx2 found to be the positive impact of the sidewalls' indentions at Rx2 location as can be seen in Figure 4-4. The sidewalls' indentions work in favour of the tr-x-V configuration by causing waveguide mode conversion, which improves the channel capacity. Figure 4-4 compares propagation rays for the tr-x-V and tr-y-H configurations at Rx2. As it illustrates for the tr-y-H configuration, multiple reflections formed by the back wall are not sufficiently strong (due to the large distance between the Rx and the back wall) to be able to compete with the tr-x-V configuration.

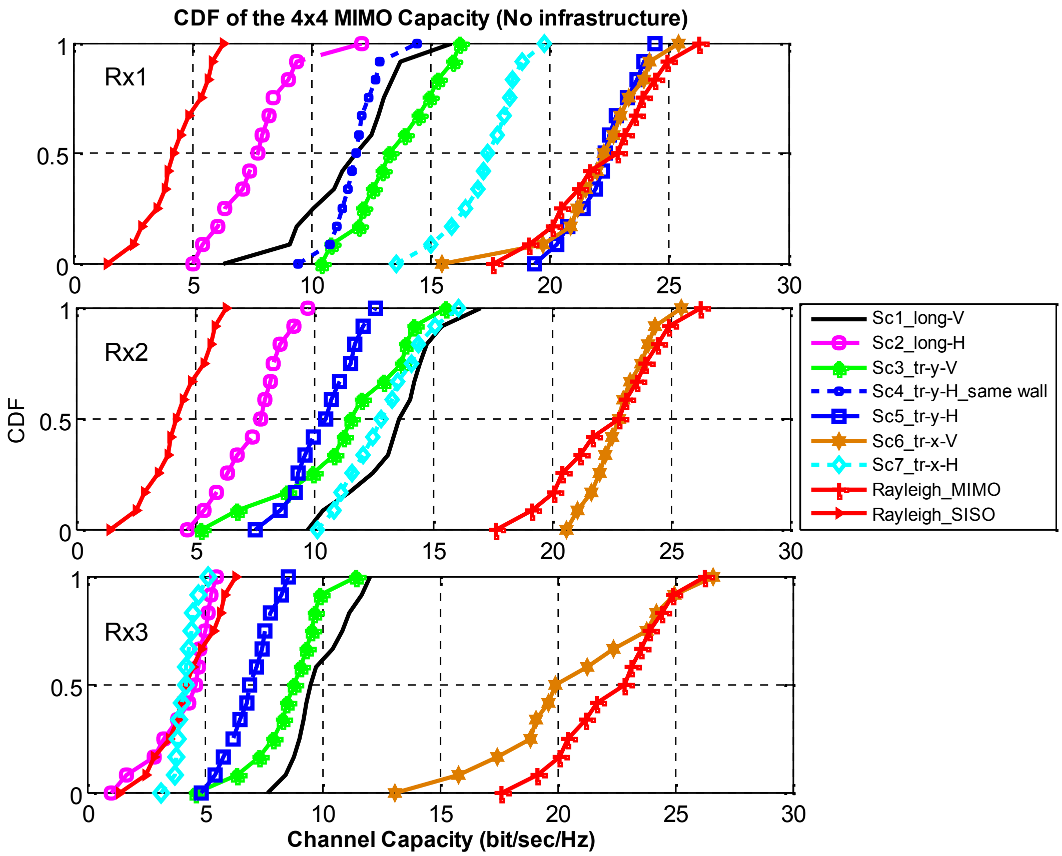

Figure 4-3 Comparison of different antenna configurations for the tunnel without infrastructure.

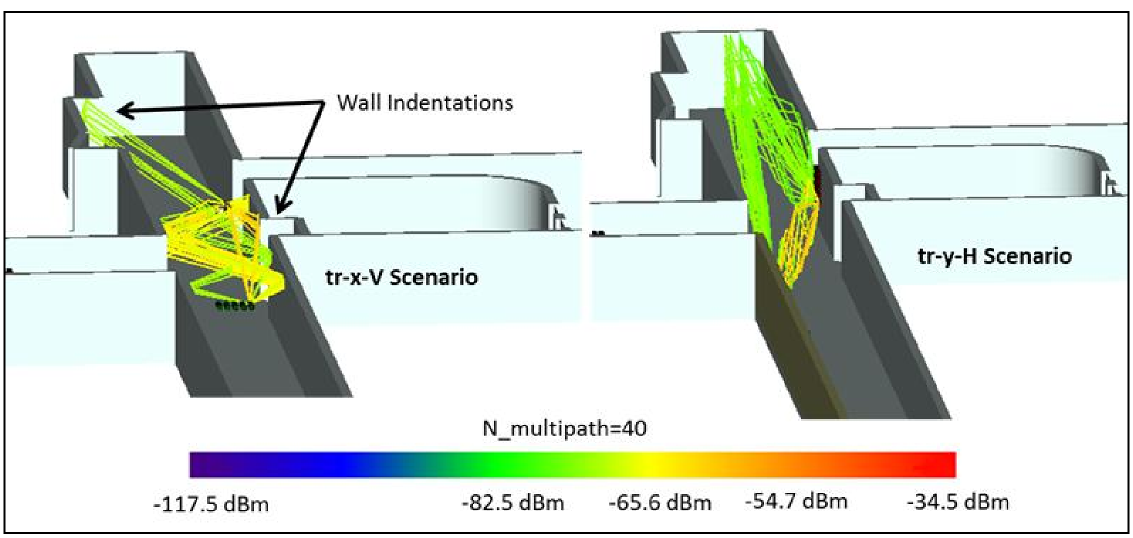

Figure 4-4 Comparison of the performance of tr-x-V and tr-y-H antenna configurations at Rx2.

4.4.2.2 *Tunnel with Infrastructure*

Figure 4-5 compares the antenna configurations for different propagation scenarios in the service tunnel including the infrastructure. The results suggest that infrastructure impacts the performance of each antenna configuration differently. For most cases, the infrastructure acts as a waveguide mode suppressor and degrades the channel capacity by blocking the key rays between the Tx and Rx. The worst impact can be seen on the tr-x-V configuration. The configuration that we found to be the best performing one for the tunnel without infrastructure shows the worst performance for the tunnel with the extensive infrastructure. On the other hand, the tr-y-H configuration offers the best performance and the closest capacity CDF to that of an i.i.d. Rayleigh fading channel for all three propagation scenarios.

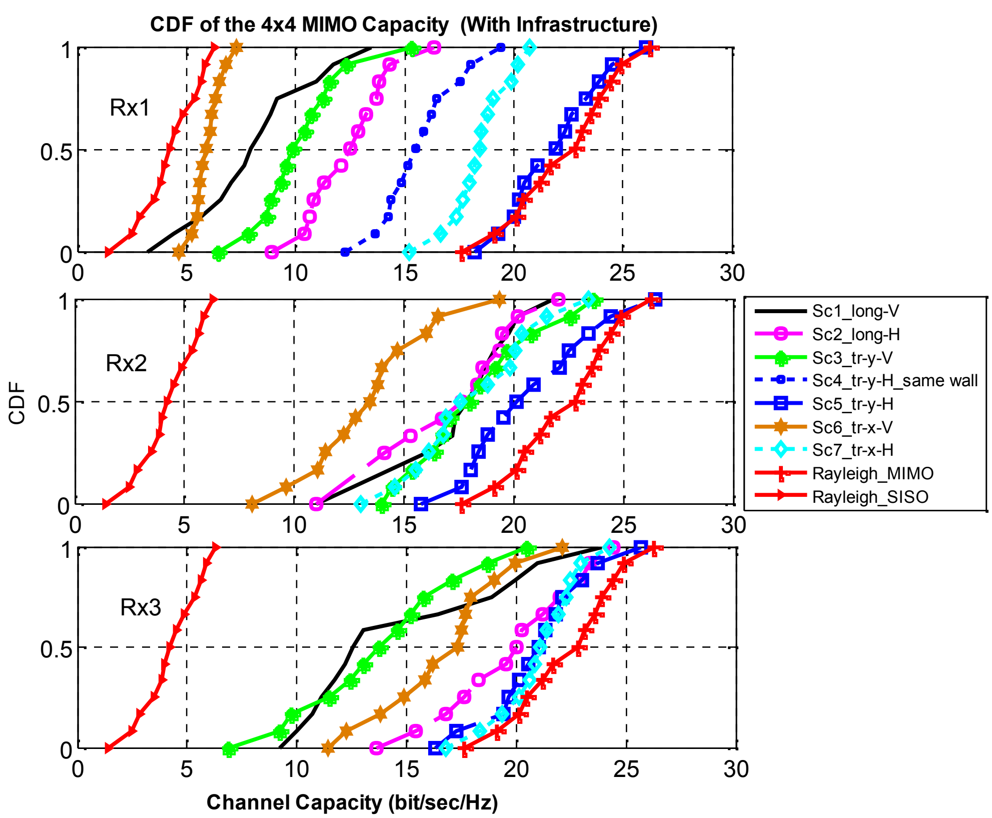

Figure 4-5 Comparison of different antenna configurations for the tunnel with infrastructure.

We can also see degradation for the configurations with vertically polarized antennas due to particular impact of infrastructure on vertically polarized rays. In an empty tunnel, we observed that vertically polarized waves reflected from the sidewalls are much stronger than the ones reflected from the ceiling/floor (unlike horizontally polarized waves). This can be explained by considering the fact that vertically polarized waves undergo lower attenuation when reflecting from vertical walls (*i.e.*, sidewalls) in an oversized dielectric waveguide [123]. Additionally, the null of the antenna radiation pattern is towards the ceiling/floor while its maximum is toward the sidewalls. The infrastructure in the service tunnel, however, does not allow formation of strong specular reflections from the sidewalls.

As can be seen in Figure 4-6, in the Tx1-Rx1 propagation scenario where so many masts are located close to one of the sidewalls (Figure 4-6), antenna configurations such as tr-x-V with vertically polarized antennas do not perform as suitable as horizontally polarized ones. This is the main reason why the tr-x-V configuration which performs best in the empty tunnel shows the worst performance at Rx1. Figure 4-6 clearly indicates the impact of infrastructure on its performance. From Figure 4-6, we can see that when the tunnel is empty, several strong rays that are comparable to the LOS path travel to the Rx. However, when the infrastructure exists only direct path (if it exists) is strong while the ones that undergone multiple reflections from the infrastructure are very weak (*i.e.*, lower order mode suppression). This can result in two effects which both degrade the capacity: (1) lower received power and (2) large LOS path compared to other multipaths generated mostly by multiple reflections from the infrastructure.

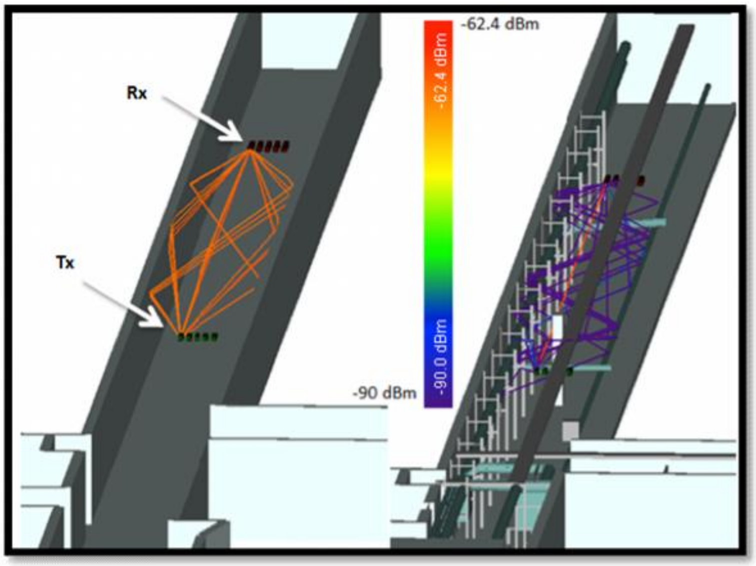

Figure 4-6 Impact of infrastructure on performance of tr-x-V-Sc6 antenna configuration.

Because the tr-x-V, tr-x-H, and tr-y-H configurations are the better performing configurations in different scenarios, we chose them for further analysis and comparison of their power. Table 4-4 is presented to show the effect of infrastructure on each of them. Depending on the MIMO array configuration and Rx location in the tunnel, the infrastructure impacts pathloss differently. Unlike all other cases, in the tr-y-H case at Rx2, the infrastructure showed positive impact which can be due to the additional reflections formed by the infrastructure between the Tx and Rx. Table 4-4 also reveals that tr-y-H configuration offers the highest and tr-x-V the lowest power level in the service tunnel with extensive infrastructure.

Based on both Table 4-3 and Table 4-4, for most scenarios infrastructure increases both the correlation and the power loss of the subchannels, which consequently degrades the MIMO channel capacity. As it can be seen, in spite of the extensive infrastructure for most cases pathloss is less than free-space-path-loss (FSPL).

Table 4-4 **Average pathloss at 2.49 GHz.**

		Without Infrastructure	With Infrastructure	Free Space Pathloss (2.49 GHz)
		PL_{ave} (dB)	PL_{ave} (dB)	FSPL (dB)
Rx1 $d_{Tx\text{-}Rx}$=31.3 m	**Sc4 (tr-y-H-same wall)**	62	64	70
	Sc5 (tr-y-H)	54	58	70
	Sc6 (tr-x-V)	54	71	70
	Sc7 (tr-x-H)	57	60	70
Rx2 $d_{Tx\text{-}Rx}$=16 m	**Sc5 (tr-y-H)**	57	54	64
	Sc6 (tr-x-V)	46	58	64
	Sc7 (tr-x-H)	50	54	64
Rx3 $d_{Tx\text{-}Rx}$=7.6 m	**Sc5 (tr-y-H)**	65	74	58
	Sc6 (tr-x-V)	52	78	58
	Sc7 (tr-x-H)	62	76	58

4.4.3 Main Observations and Conclusions from Ray Tracing Simulations

Although the results obtained from assessing the antenna configurations based on the ray tracing simulations may seem to be site-specific, they provide physical insight for deployment strategies. Main conclusions of this study can be summarized as follows:

- Three waveguide mechanisms can be considered which govern the propagation in the tunnel as an oversized dielectric waveguide: a) mode coupling from the antenna to the tunnel (depending on the antenna location in the cross-sectional plane and the antenna polarization), b) mode coupling between waveguide modes (may be caused by branch, back walls, walls' indentions, *etc*.), and c) waveguide mode suppression (may be caused by infrastructure, curvature, *etc*.).
- Array configuration and antenna polarization can significantly impact MIMO system performance in short underground tunnels.

- Interelement spacing of 2λ between antenna elements at both ends (Tx and Rx) provides sufficient decorrelation.
- As the simulation results reveal, LOS deployments of MIMO antenna configurations offer more desirable performance in the short tunnel, particularly when the infrastructure is extensive, which results in additional power loss. Therefore, deployments which ensure LOS link as well as larger interactions between the Tx and Rx are preferred.
- However, in the LOS cases, MIMO capacity seems to be more affected by the choice of antenna configuration and deployment compared to the NLOS case. Therefore, antenna configuration requires more careful design in LOS cases than in NLOS cases.
- Because rays are more concentrated for scenarios at Rx1(where Tx and Rx are located in the long section of the tunnel) than the ones at Rx2 and Rx3, antenna configuration design requires more attention.
- Two antenna configurations of tr-x-V and tr-y-H have been identified as the best performing antenna configurations for the empty tunnel and the tunnel with infrastructure, respectively. While tr-x-V configuration remarkably outperforms all other configurations in the empty tunnel, it shows very poor performance in the case of extensive infrastructure.
- While infrastructure was found to be a degrading factor for most cases, some geometrical properties of tunnel such as sidewalls' indentions show positive impact on the MIMO system performance.

4.5 Experimental Validation

From results obtained by the ray tracing simulations, two better performing MIMO array configurations were chosen for experimental validation. Employing the MIMO channel sounder, we experimentally validated their performance predictions. More detail about the MIMO channel sounder we used is given in Table 4-5. We placed the Tx and Rx grids in the exact same locations as we had in the ray tracing simulations. At the Rx side, an xy-positioner (3×5 points) was used whereas at the Tx a single antenna was being moved at six points.

Table 4-5 Measurement specifications

Unit	Specification
VNA master	Anritsu MS2034A
Frequency band	2.49 - 4 GHz
Number of frequency points	551
Antenna	Electrometrics UWB Biconical antennas
Positioner	Velmex linear xy-positioner
Tx power	26 dBm
Grid point spacing	2λ at 2.49 GHz
Dynamic range	120 dB
Power amplifier	Ophir - Model 5303075
Fibre optics	Miteq SMCT-100M11G

Experimental and simulation results of capacity statistics for tr-x-V and tr-y-H configurations are presented in Table 4-6. Global normalization factors at each Rx grid location for with and without infrastructure have been used (in total six normalization factors). Six normalization factors are calculated so that fair comparison can be performed between different antenna configurations at each Rx grid. Measured **H**-matrices have also their normalization factors at each Rx grid location (three normalization factors for three Rxs). As can be seen from Table 4-6, simulation and the measurement results show good agreement (except for the tr-x-V configuration at Rx1). In addition to tabular presentation, simulation and measurement results for two antenna configurations of tr-x-V and tr-y-H are compared in Figure 4-7. Similarly, the experimental results show good agreement with earlier simulation results and confirm higher performance of tr-y-H configuration compared to tr-x-V configuration for the tunnel with extensive infrastructure.

Table 4-6 Capacity statistics at 2.49 GHz and SNR=20 dB to compare MIMO capacity of different antenna configurations (with power-impact)

		With Infrastructure			Measurement (With Infrastructure)		
		C_{ave}	σ	$C_{outage\%10}$	C_{ave}	σ	$C_{outage\%10}$
Rx1	**Sc4 (tr-y-H-same wall)**	15.68	1.66	13.82	16.20	1.62	14.11
	Sc5 (tr-y-H)	21.86	1.92	19.7	22.93	2.03	19.99
	Sc6 (tr-x-V)	5.96	0.59	5.34	11.59	1.32	10.01
Rx2	**Sc5 (tr-y-H)**	20.67	2.69	17.66	21.28	1.98	18.86
	Sc6 (tr-x-V)	13.36	2.43	10.63	16.40	1.62	14.36
Rx3	**Sc5 (tr-y-H)**	21.03	2.08	18.67	21.98	2.16	19.15
	Sc6 (tr-x-V)	16.68	2.52	13.03	17.96	1.76	15.59

Although this figure shows a relatively good agreement between the simulation and measurement, it indicates that the ray tracing simulation underestimates the capacity for both antenna configurations. This underestimation is more noticeable for tr-x-V configuration in the pure LOS scenario (Rx1) where rays are more concentrated compared to other scenarios (Rx2 and Rx3). This implies that the accuracy of the ray tracing method is not consistent for different scenarios (*i.e.*, Rx grid locations). At low capacities which can be associated to highly concentrated rays, achieving same results from both measurement and simulation is less likely due to higher sensitivity of the results to small errors in the modeling. For example, the results of ray tracing may be very sensitive to the array locations, and a slight difference between exact array locations in the measurement and simulation may result in significant errors.

As can be seen from Figure 4-7, the deviation of simulation and measurement is less for Rx2 and Rx3 scenarios where rays are more spread. This implies that ray tracing modeling for the tunnels might not be as accurate as it is for conventional indoor environments, therefore further enhancement for modeling the tunnels is required. This issue may be resolved by increasing the ray resolution (by allocating larger number of rays per angle unit) for the study areas with highly concentrated rays. But in the case of extensive infrastructure, runtime will substantially increase.

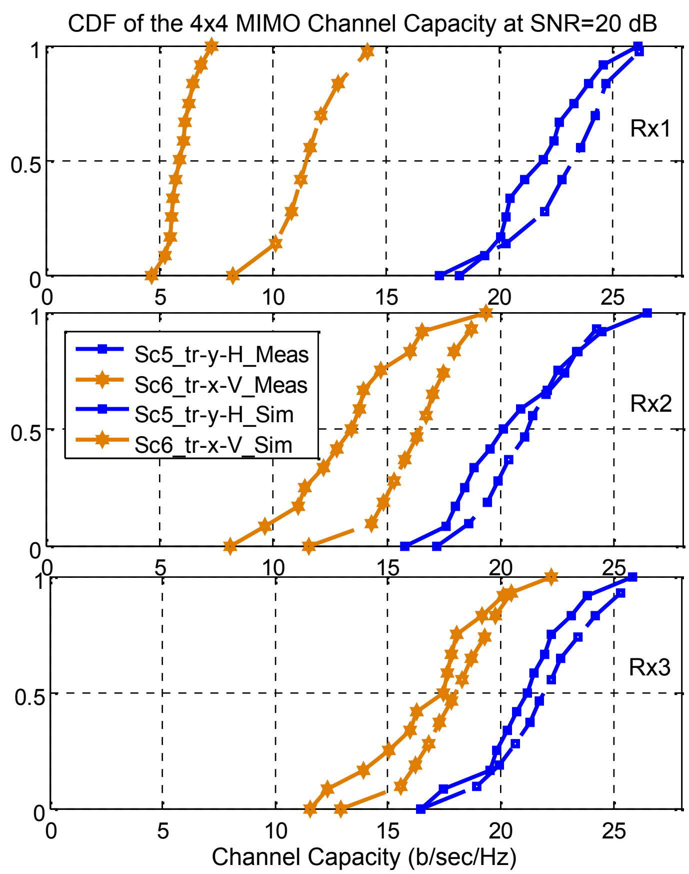

Figure 4-7 Comparison of simulated (with infrastructure) and measured MIMO capacity CDFs.

The MIMO measurements in the service tunnel allowed us to obtain more accurate results, however it did not provide any physical insights. Whereas by conducting ray tracing simulations, we could observe and trace the propagation rays, and obtain physical insights, but it failed to offer consistent accuracy for different scenarios.

4.6 Conclusions

In this study, we have shown that in spite of low angular spread in underground mines, careful design of antenna configuration allows benefiting from MIMO technology for AP-AP communications. Our results reveal that array orientation, antenna separation, and polarization significantly influence performance of multiple-antenna systems in underground tunnels. Consequently, capacity can be improved by careful antenna configuration design in underground mines.

We have determined sufficient interelement separation, antenna polarization, and array orientation. Antenna separation of $\lambda/2$ that is common in most of the off-the-shelf products, does not show high performance. Our study showed MIMO antenna separation required to be 4 times longer than in conventional indoor environment with rich multipath (*i.e.*, 2λ).

We compared different configurations based on their capacity, sensitivity to typical locations in a mine and sensitivity to the infrastructure. In this study, we also examined the effect of geometry of the tunnel such as indentations of the walls and infrastructure. Infrastructure found to be a degrading factor on capacity for most cases due to blockages it causes.

We have identified two practical MIMO access point configurations which show better capacity (bit/sec/Hz) for a 4×4-MIMO system inside an underground service tunnel: horizontal array with vertically polarized antennas (tr-x-V) and vertical array with horizontally polarized antennas (tr-y-H). While the tr-x-V configuration performs remarkably better in different propagation scenarios in the tunnel with little or no infrastructure, if extensive infrastructure exists, the tr-y-H configuration which was found to be less affected by the infrastructure, performs significantly better than tr-x-V configuration. As a result, infrastructure density should be considered as an important factor while designing MIMO antenna configuration for deployment in linear confined spaces such as underground tunnels.

CHAPTER 5: EFFECT OF ARRAY PROPERTIES ON MIMO SYSTEM PERFORMANCE IN AN UNDERGROUND MINE

5.1 Introduction

MIMO systems are a well-proven wireless technology for use in surface environments where they offer higher data rates, greater coverage and increased reliability for line-of-sight (LOS) and non-line-of-sight (NLOS) scenarios compared to older technology. Nevertheless, their performance is uncertain in confined spaces such as underground mines. The rapid growth of MIMO-based technologies (*e.g.*, reconfigurable antennas, advanced space-time coding schemes, multi-user MIMO) in the past decade, has made it more crucial to resolve physical layer limitations when deploying MIMO systems into new environments to maximize performance.

Currently, most underground mines are equipped with legacy communication systems such as leaky feeders that suffer from limited coverage, low data rates, and require an LOS path. These limitations make MIMO technology an attractive solution for wireless communications inside mines because MIMO has overcome these problems in surface environments. However, MIMO-based systems are highly dependent on the surrounding physical environment. Therefore, conventional MIMO-based wireless devices that work well in surface environments do not necessarily work well in underground mine tunnels where propagating signals are characterized by a low angular spread.

Unlike the extensive MIMO studies conducted for indoor and outdoor environments, only a few experimental studies have been conducted for underground environment such as subway tunnels [21]- [24] and underground mines [124]. In [124], as the only experimental MIMO study in underground mines, performance of a 2×2-MIMO system for two types of antenna radiation patterns has been compared in a very short underground mine (25 m). However, further investigation of antenna properties and the effect of the mine structure (*e.g.*, curvature) on the channel capacity are required. Relevant studies for subway tunnels have focused on access-point (AP) to mobile communications at 900 MHz [21], in which transmitter antennas are on the platform and receiver antennas are located on the train windshield. While previous studies confirm that MIMO can be a promising technology for AP-to-mobile applications in underground environments, too many uncertainties still remain. For example, there is no performance prediction, array design, deployment strategy or channel prediction available for MIMO-based AP communications inside underground mines. In addition, due to geometric dissimilarities between mines and subway tunnels, the applicability of the results obtained for tunnels to mines, is questionable.

In response to these uncertainties, we have conducted both theoretical and experimental MIMO performance analysis for underground mines. We have evaluated MIMO-based AP communications and answered some of the questions left in the literature. We have also shown how antenna properties (*e.g.*, antenna spacing, polarization and height) impact wireless performance, and thus should be carefully considered in array configuration designs and deployments inside mines.

We have experimentally evaluated the MIMO system performance in an actual mine site, and study the impact of other antenna properties, such as height and polarization. By employing different normalization methods on the channel coefficient matrix (**H**-matrix), we have differentiated the ways that antenna properties impact the capacity (the spatial structure or the power). We have also studied the effect of mine curvature on the MIMO channel capacity.

We have compared the experimental results in the mine tunnel with a theoretical model based on the waveguide theory (multimode waveguide model) [70], which was developed for underground tunnels and claims to be applicable to underground mine tunnels. Our experimental work matches well with this model, and confirms its applicability to underground mine tunnels. We have used this model to achieve physical insights and explain our experimental results. Additionally, this model allows us to evaluate the channel capacity of several antenna spacings and accordingly determine the proper antenna spacing for MIMO-based systems.

Finally, we conclude this study by providing results that can be useful in developing guidelines for MIMO system deployments in underground mines. The remainder of this chapter is organized as follows. In Sec. 2, we describe the measurement site, our setup and measurement scenarios. In Sec. 3, the multiple antenna analysis used in this study is presented. In Sec. 4, results and impact of antenna properties, which can be used in MIMO system deployment in underground mines are discussed. Finally, in Sec. 5, we conclude the chapter by presenting key findings and their implications.

5.2 MIMO Measurement in an Underground Mine

5.2.1 Measurement Site and Equipment

We performed a MIMO measurement campaign at Myra-Falls underground mine located in Strathcona Park on Vancouver Island, B.C., Canada (Figure 5-1). The mine gallery was 1900 ft (579 m) below the surface. The cross-sectional shape of the tunnel was rectangular. The width and height of the tunnels varied from 5m to 5.7 m and from 3.5 m to 4.2 m, respectively. The mine's floor was covered in mud, and the only infrastructure was leaky feeder cables, wires and pipes installed along the ceiling. The sidewalls were not perfectly straight, and had several protrusions, but their roughness was insignificant. We had the opportunity to conduct static measurements because the mine-level was closed and nobody was working there. Photography of MIMO measurement setup at Myra Falls is given in Figure 5-2. More details on our measurement setup and calibration of the equipment have been described in Chapter 3.

For this study, we used our MIMO ultra-wide-band (UWB) channel sounder system. It uses the virtual array method, in which mutual coupling effect of the antenna elements is not included in the channel characterization. Although this channel sounder performs UWB measurements, the results and analysis presented in this work focuses on MIMO characterization at frequencies near the 2.4 GHz, industrial-scientific-medical (ISM) band. We used an Anritsu MS2034A vector-network-analyser (VNA) to send and receive frequency span of 2.49 GHz - 4 GHz with 551 frequency points. Two UWB Biconical antennas were used, one at the transmitter and one at the receiver. The transmitter antenna was manually moved across the tunnel and was connected to the VNA using an RF-over-fibre range extender. The receiver antenna was automatically moved on a fixed xy-positioner

(1 m × 0.5 m). Locations of the receiver (Rx) grid and transmitting (Tx) array in the mine are demonstrated in Figure 5-1. For each transmitter position, the frequency dependent transfer function between the transmitter antenna and all 15 virtual receivers was measured.

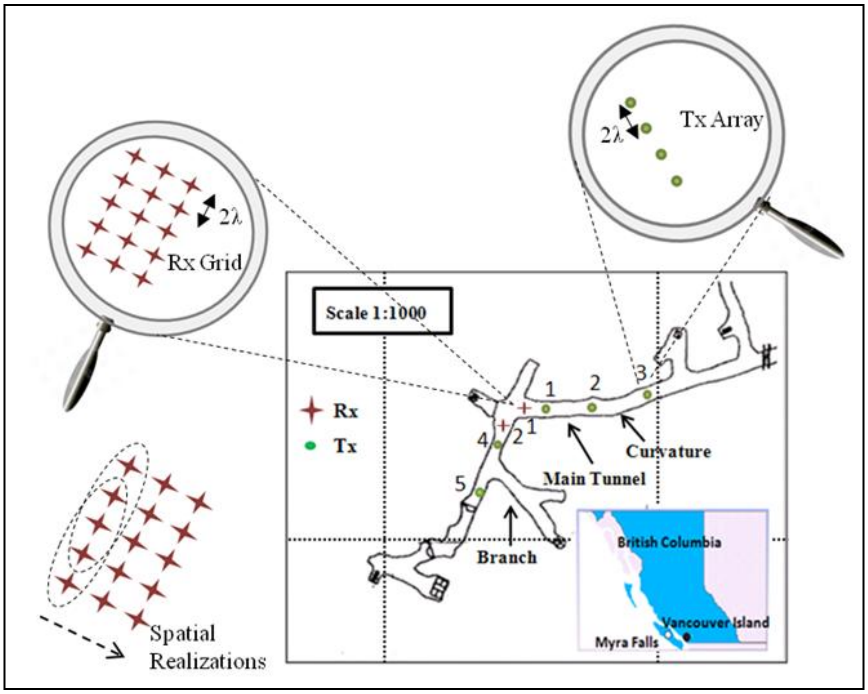

Figure 5-1 Map of the Myra-Falls mine in B.C., Canada and the transmitting (Tx) array and receiver (Rx) grid locations (5 Tx array locations and 2 Rx grid locations).

Figure 5-2 Photography of RF equipment in Myra Falls mine.

5.2.2 Measurement Scenarios

In spite of time constraints in the mine, spatial samples were collected from various parts of the tunnel. Measurement scenarios for different propagation scenarios, such as LOS, NLOS after a curvature, *etc.* are as follows: short-distance LOS (10 m, Tx1-Rx1), long-distance LOS (27 m, Tx2-Rx1), curve shaped NLOS (49 m, Tx3-Rx1), NLOS in a branch (12 m, Tx4-Rx1) and LOS with a branch in the middle (21 m, Tx5-Rx2). All of these measurements can be considered as typical scenarios in underground mines. As shown in Figure 5-1 and Table 5-1, five sets of measurements were taken: four Tx locations (Tx1-Tx4) for Rx1 and one Tx location (Tx5) for Rx2. At the Tx locations, 4 antenna positions with a separation of 2 wavelengths (2λ) (at 2.49 GHz) were considered in the middle of the tunnel cross-section. At the Rx locations, the virtual array was implemented by using a xy-positioner with 15 evenly spaced points. Location Rx1 was used for all but one of the scenarios, in which a branch was located in the middle of the direct Tx-to-Rx path.

5.2.3 Measurement Design

Because no previous work has determined the sufficient spacing required for multiple antenna measurements in underground mines, we investigated previous studies on similar linear confined spaces to select the minimum separation. Several studies in hallways show that the coherence distance is larger than λ [125],[19], and thus the common separation of λ/2 for conventional indoor environments is not sufficient. In addition to hallways, we considered the results of our earlier ray-tracing study and development runs in a mid-size service tunnel (width=2.7 m, height=2.4 m, length=103.5 m). A transmitter and a receiver grid with vertically polarized antennas were located about 35 m apart and in the middle of the tunnel. Because the highest correlations correspond to successive elements, we chose

Pearson's correlation coefficient of successive elements (*m, n*) at the Rx grid for Tx antenna as follows:

$$\rho_{hm,hn} = Corr(h_m, h_n) = \frac{E[(h_m - \mu_{hm})(h_n - \mu_{hn})]}{\sigma_{hm}\sigma_{hn}} \quad (1)$$

where h_m and h_n are channel coefficients corresponding to *m* and *n* channels, and also μ and σ represent mean and standard deviations, respectively. The envelope correlation coefficients for two separations of λ/2 and 2λ were found to be 0.82 and 0.18, respectively. Based on this result and previous work in hallways, we chose 2λ spacing between antenna elements for the Tx array and the Rx grid.

To see the impact of array height, we considered two heights of under the ceiling (2.7 m above ground) and medium height (1.7 m above ground), and to study the impact of antenna polarization, for both vertical and horizontal antenna polarizations, measurements were performed at medium height. In summary, we collected data for three antenna scenarios: (1) ceiling height with vertically polarized antennas (CV configuration), (2) medium height for vertically polarized antennas (MV configuration), and (3) medium height for horizontally polarized antennas (MH configuration). For all the Rx grid points, we performed frequency domain measurement and collected amplitude and phase of the channel gain over the frequency range of 2.49 GHz - 4 GHz. Measurement scenarios are summarized in Table 5-1.

To select the suitable array orientation, Pearson's correlation of successive antenna elements was found for two orientations, one perpendicular and one parallel to the tunnel axis. Figure 5-3 shows how successive antenna elements are chosen for each array orientation. Results of envelope correlation coefficients for all measurement scenarios are summarized in Table 5-2. Correlation coefficient values consider all four Tx antennas (*i.e.*, Tx array) for each measurement scenario.

Table 5-1 MIMO measurement scenarios in the Myra Falls underground mine.

	Tx1 Array at Loc.1	**Tx2 Array at Loc.2**	**Tx3 Array at Loc.3**	**Tx4 Array at Loc.4**	**Tx5 Array at Loc.5**
Rx1 Grid	LOS (10 m) MV	LOS (27 m) (before a curve) MH,MV,CV	NLOS (49 m) (after a curve) MH,MV,CV	NLOS (12 m) (in a branch) MH,MV,CV	----------
Rx2 Grid	----------	----------	----------	----------	LOS (21 m) (a branch in the middle) CV

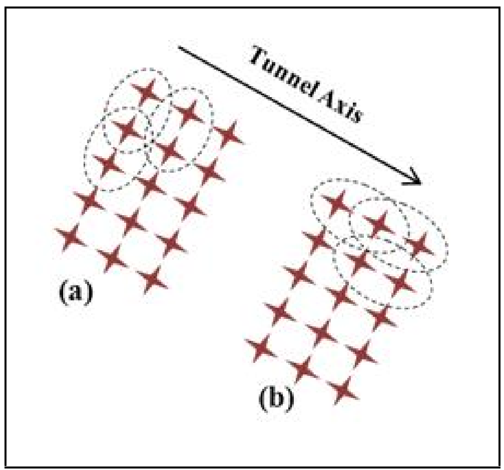

Figure 5-3 Spatial correlation analysis on the successive antenna elements on the Rx grid for two different array orientations: (a) perpendicular to the tunnel axis and (b) parallel to the tunnel axis.

As it can be seen in Table 5-2, array orientation perpendicular to the tunnel axis offers much lower correlation compared to the array orientation parallel to the tunnel axis. Choosing array orientation to be perpendicular to the tunnel axis with its elements separated by 2λ provides a sufficient degree of decorrelation (less than 0.7) regardless of the antenna polarization, height, and propagation scenario. Intuitively, this orientation provides suitable decorrelation as it occupies the largest space orthogonal to the arriving signals. Therefore, we chose this array orientation with element separation of 2λ for constructing 4×4-MIMO **H**-matrices. While such considerations for array design have not been evaluated for underground mines, the results of capacity analysis will determine whether this design is appropriate or not.

Table 5-2 Envelope correlation coefficients of Rx grid antennas for different measurement scenarios (*f*=2.49 GHz).

	Rx Array Orientation Perpendicular to the Tunnel's Axis			Rx Array Orientation Parallel the Tunnel's Axis		
	MH	**MV**	**CV**	**MH**	**MV**	**CV**
Loc. 1 LOS (10 m)	----------	0.24	----------	----------	0.40	----------
Loc. 2 LOS (27 m) Before Curvature	0.21	0.10	0.63	0.67	0.75	0.86
Loc.3 NLOS (49 m) After Curvature	0.30	0.46	0.07	0.83	0.76	0.80
Loc.4 NLOS (12 m)	0.40	0.07	0.27	0.47	0.54	0.59
Loc.5 LOS (21 m) Branch-Middle	----------	----------	0.45	----------	----------	0.91

5.3 Multiple Antenna Analysis

5.3.1 Constructing Channel Coefficient Matrices

We started MIMO analysis, after ensuring the absence of large-scale fading across the chosen Tx array. This was examined by averaging the channel power over all the frequencies and Rx grid points on the positioner for each Tx location and comparing them all. Then, as shown in Figure 5-1, six 4×4-MIMO spatial realizations based on uniform-linear-arrays (ULA) oriented perpendicular to the tunnel axis, are constructed (from the 4-element Tx array and 3×5-element Rx grid). In addition to spatial realizations, 551 frequency samples over range of 2.49-4 GHz and separated by 2.74 MHz were collected.

For our analysis, we consider a bandwidth of 96 MHz (35 frequency samples). However, because frequency samples within one coherence-bandwidth (*BWc*) are correlated, all 35 samples cannot be treated as independent. Adding frequency samples to our spatial ones requires them to be independent, which implies separation of at least one *BWc* between them [121]. Coherence bandwidth was found to be 4 MHz from the channel-frequency-response. Therefore, only half (17 samples) of the 35 frequency samples (with separation of 2.74 MHz) can be considered independent. As a result, 102 (17×6) 4×4-MIMO **H**-matrices were constructed at each location.

5.3.2 H-Matrix Normalization and Channel Capacity

It is a common practice in MIMO antenna design to normalize **H**-matrices so that the average SNR at the receiver elements is set to a fixed value and can be adjusted as a parameter. Depending on the objective of MIMO analysis, different methods can be used to calculate normalization factor. In order to perform a fair comparison of different systems or schemes, it is required to consider one normalization factor for all scenarios under the study. Here, two the normalization factors are considered for performance comparison of different antenna scenarios. The choice of normalization factor depends on whether the objective is to study the effects of: (1) subchannels' correlation only, or (2) both correlation and power, on the capacity.

For normalization (1), every **H**-matrix is normalized by its own Frobenius norm, which is the RMS value of the elements of a matrix and calculated as follows [6]:

$$
\begin{aligned}
\mathbf{H}_{\text{nor}} &= \mathbf{H}\sqrt{\frac{N_{Tx}N_{Rx}}{\|\mathbf{H}\|_F^2}} \\
\|\mathbf{H}\|_F &= \sqrt{\sum_{i=1}^{N_{Rx}}\sum_{j=1}^{N_{Tx}}\left|h_{ij}\right|^2}
\end{aligned} \tag{2}
$$

where $\|.\|_{\mathbf{F}}$ denotes Frobenius norm and **H**, N_{Rx}, N_{Tx}, and h_{ij} are channel coefficient matrix, number of Rx antennas, number of Tx antennas, and channel matrix entries, respectively. Normalized **H**-matrices obtained by this method are only affected by the level of correlation experienced by the antennas.

Normalization (2) is often used for fair comparison between different MIMO scenarios (antenna polarization, array height, *etc.*) or to study the effect of something (*e.g.*, curvature) on the MIMO performance [24],[121]. This normalization method, which is also called global channel normalization [122], not only includes subchannels' correlation but also power contribution of each case. For this normalization method, a common normalization factor is considered for all scenarios under comparison, which is calculated based on averaging Frobenius norms of **H**-matrices of all cases being compared. Considering K total channel realizations at each transmitter location, this normalization can be calculated as follows:

$$
\begin{aligned}
\mathbf{H}_{\text{nor}} &= \mathbf{H}\sqrt{\frac{KN_{Tx}N_{Rx}}{\|\mathbf{H}\|^2}} \\
\|\mathbf{H}\| &= \sqrt{\sum_{k=1}^{K}\sum_{i=1}^{N_{Rx}}\sum_{j=1}^{N_{Tx}}\left|h_{ij}\right|^2}
\end{aligned} \tag{3}
$$

Note that in both methods, the effect of the antenna gain (Biconical at 2.49 GHz) and the pathloss between the transmitter and receiver have been excluded. After finding normalized **H**-matrices, capacity C (bit/s/Hz) of a MIMO system with N_{Tx} transmitting antennas and N_{Rx} receive antennas can be calculated by [6]:

$$C = \log_2\left[\det\left(\mathbf{I}_{N_{Rx}} + \frac{SNR}{N_{Tx}}\mathbf{H}_{\mathbf{nor}}\mathbf{H}^{*}_{\mathbf{nor}}\right)\right] \tag{4}$$

where * denotes the transpose-conjugate, $\mathbf{H}_{\mathbf{nor}}$ is the $N_{Rx}\times N_{Tx}$ normalized channel matrix, SNR is average signal to noise ratio and **I** is identity matrix. It is assumed that the N_{Tx} sources have equal power and are uncorrelated.

5.4 Measurement Results and Discussions

5.4.1 Performance Comparison of MIMO Antenna Scenarios

Channel capacity which is the main performance measure of MIMO systems, is influenced by two factors: subchannels' power and the level of spatial correlation among subchannels. Therefore, to study the effect of array properties on the MIMO channel capacity, we chose to determine how each array property impacts these two factors. First, we assess them based on their impact on spatial correlation without considering their contribution in power, and afterwards we include the power aspect too. This can be done by applying different normalization methods to the **H**-matrices.

5.4.1.1 *Channel Capacity Without Power Considerations*

In this section, channel capacity CDFs have been found for different measurement scenarios and the pathloss between the centres of the Tx array and Rx grid is calculated, while the antenna element gain and array's power impact (differences due to the array height and antenna polarization) at each Rx grid are excluded. Therefore, the degree of subchannels' decorrelation is the only factor that controls the capacity. This has been done by normalizing every **H**-matrix by its own Frobenius norm (normalization (1)). Figure 5-4 presents the capacity CDFs of measured channels alongside the CDF of an i.i.d. Rayleigh fading channel to compare the measured channels to an ideal channel, in terms of MIMO performance.

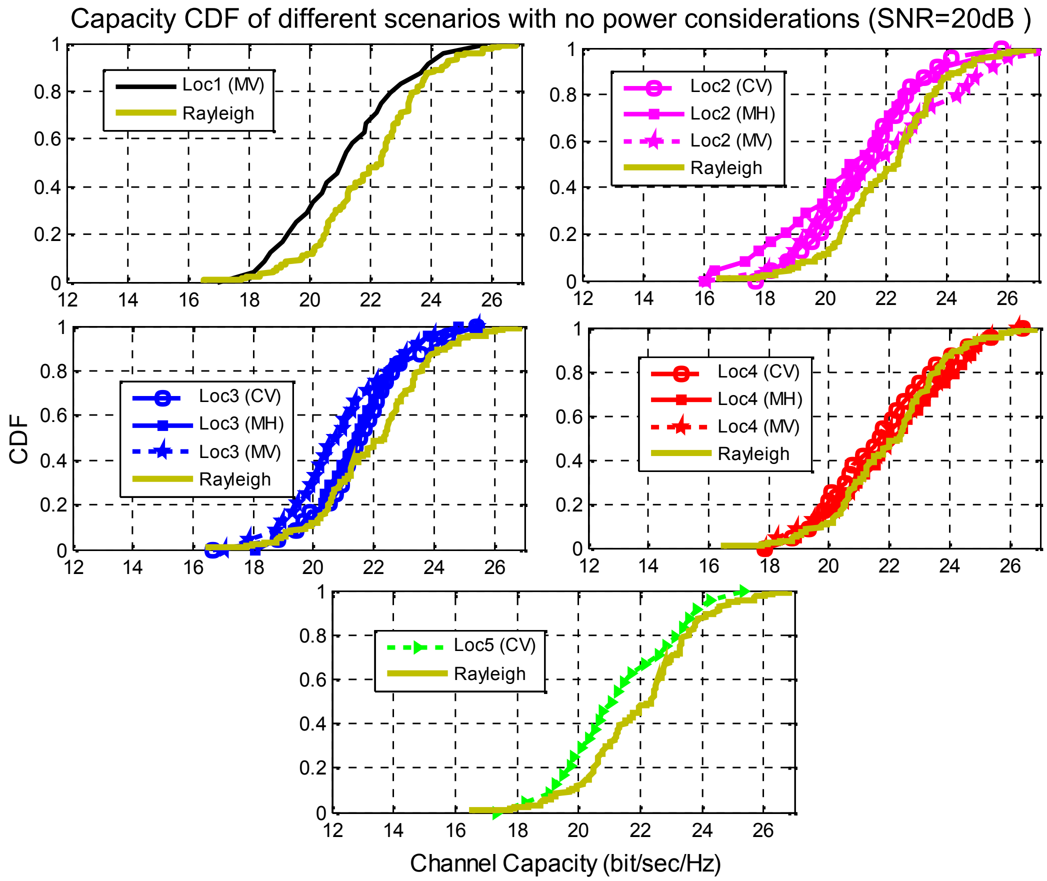

Figure 5-4 CDFs of 4×4-MIMO capacity without power considerations (based on the measurement).

As Figure 5-4 shows, the capacity CDFs for different antenna heights and polarizations are similar and close to that of an i.i.d. Rayleigh fading channel. This implies that sufficient spacing and properly chosen array orientation provide a sufficient degree of decorrelation regardless of the antenna polarization and height. However, further analysis is required to see whether they impact subchannels' power. We can also see that the spatial decorrelation achieved by the proposed array is not sensitive to the propagation scenario in the mine.

Another way of analysing the spatial structure of MIMO subchannels is to study singular values of the **H**-matrices. Average singular values corresponding to different measurement scenarios in the mine are presented in Table 5-3. All singular values are normalized to the largest singular value. Table 5-3 also confirms that spatial structure of the wireless channel is very close to that of an i.i.d. Rayleigh fading channel (rich-multipath channel), and provides required decorrelation among the subchannels. Therefore, the spatial structure of the wireless channel is suitable and has the potential for achieving multiplexing gain. The rich-multipath for close Tx-Rx distances has also been reported in other studies [126],[127]. In [127], several amplitude distributions, such as Nakagami, Gamma, Rice, Rayleigh and Lognormal, are tested to model small-scale fading. Using a Kolmogorov-Smirnov's (KS) goodness-of-fit test, the authors have shown that the measured LOS scenario (1 m-12 m) can be modeled by both Nakagami and Rayleigh distributions.

To provide a physical explanation and justification for observing decorrelated MIMO subchannels in the short underground mine tunnel, we have employed the multimode waveguide model, which has been developed and used by Sun *et al*. [70] to characterize wireless propagation in underground tunnels. In this model, a tunnel is considered to be an oversized dielectric waveguide and the modes obtained by the waveguide theory are all possible solutions of Maxwell's equations that can exist in the tunnel. We also used this model for MIMO channel characterization and evaluation of our experimental results in the underground mine tunnel. More detail, including the mathematical expressions of this model for tunnels with rectangular cross-sectional shape, can be found in [70].

Table 5-3 Singular values of measured H-matrices and i.i.d. Rayleigh H-matrices (all singular values are normalized to the largest one).

		Average Singular Values			
		σ_1	σ_2	σ_3	σ_4
i.i.d. Rayleigh fading channel		**1**	**0.69**	**0.40**	**0.14**
Loc. 1 (10 m)	**MV**	1	0.71	0.39	0.14
Loc. 2 (27 m)	**CV**	1	0.55	0.34	0.15
	MH	1	0.67	0.39	0.15
	MV	1	0.63	0.33	0.11
Loc. 3 (49 m)	**CV**	1	0.70	0.38	0.14
	MH	1	0.67	0.39	0.16
	MV	1	0.55	0.30	0.10
Loc. 4 (12 m)	**CV**	1	0.67	0.36	0.13
	MH	1	0.69	0.40	0.14
	MV	1	0.70	0.44	0.15
Loc. 5 (21 m)	**CV**	1	0.61	0.32	0.12

Angular spread is a key indicator that shows whether a wireless propagation environment has the potential of offering spatially decorrelated subchannels or not. Larger angular spread offers higher spatial decorrelation (or equivalently lower correlation) among the multiple antennas. To characterize the angular spread, we applied the multimode waveguide model to an equivalent rectangular tunnel with the same cross-section as the Myra Falls mine (width: 5.5 m and height: 4 m). Angular spread in a tunnel can be found as follows [128]:

$$\varphi_{rms} = \sqrt{\frac{\int_{-\pi/2}^{+\pi/2} (\varphi - \bar{\varphi})^2 A(\varphi) d\varphi}{\int_{-\pi/2}^{+\pi/2} A(\varphi) d\varphi}} \qquad \bar{\varphi} = \frac{\int_{-\pi/2}^{+\pi/2} \varphi \, A(\varphi) d\varphi}{\int_{-\pi/2}^{+\pi/2} A(\varphi) d\varphi} \qquad (5)$$

where φ_{rms} and $A(\varphi)$ are the azimuth angular spread and power azimuth spectrum, respectively. Figure 5-5 shows that the angular spread of the near zone area (including 10 m distance) is quite large. This large angular spread in the near zone is the result of strong reflections from the walls. For further distances (more than about 200 m), angular spread becomes very low (about 4^o) due to high attenuation of higher order waveguide modes [70]. To improve spatial decorrelation among subchannels at further distances, antenna separation may need to be increased (more than 2λ).

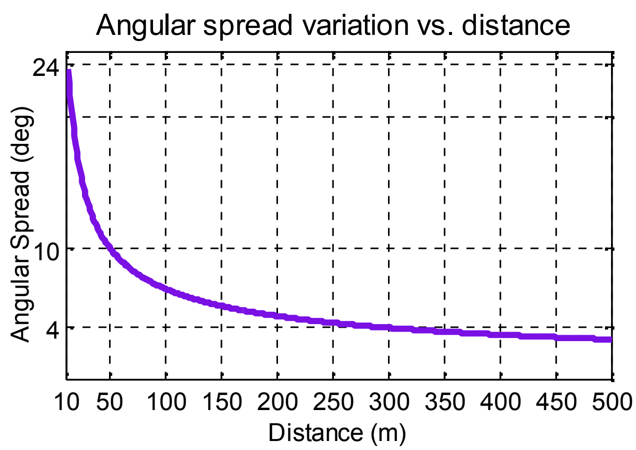

Figure 5-5 Angular spread variation versus distance (based on multimode waveguide model).

To exploit the potential of the spatial decorrelation offered by the surrounding environment and achieve the multiplexing gain, interelement spacing of the antenna array should be chosen properly. Figure 5-6 (a) shows the capacity as a function of distance, and Figure 5-6 (b) shows capacity CDFs for different antenna separations obtained by using the multimode waveguide model. As can be seen from both figures, the common antenna spacing of the off-the-shelf products (λ/2) is not sufficient, and does not offer consistent performance over Tx-Rx distance. On the other hand, 2λ separation shows suitable and consistent performance (capacity), and spacing the antennas further than that (*e.g.*, 6λ) does not achieve higher capacity. This confirms our measurement results. For very large Tx-Rx distances however, the element spacing may require to be increased. The capacity CDF for 2λ spacing also matches well with the capacity results measured in the mine.

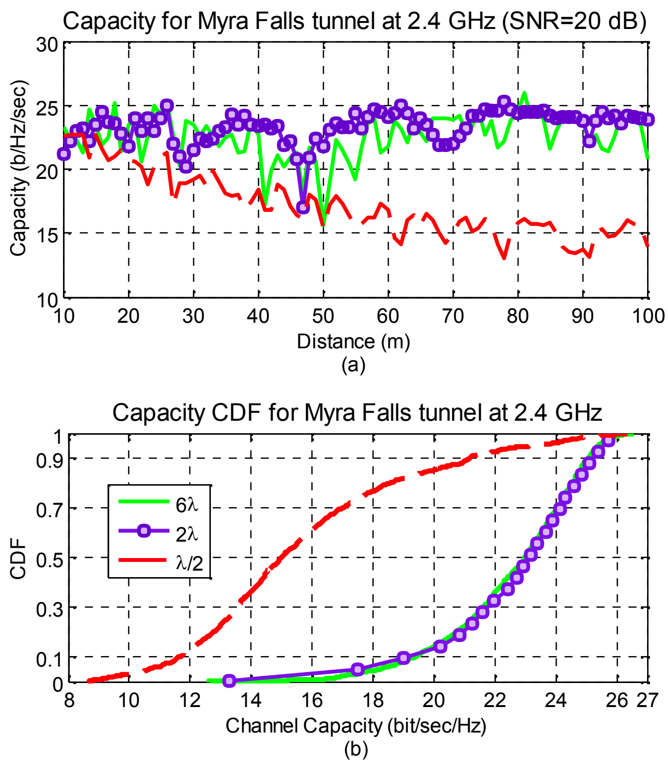

Figure 5-6 Capacity of 4×4-MIMO system for different antenna spacings (based on the multimode waveguide model).

5.4.1.2 *Channel Capacity With Power Considerations*

To include the power impact of array height and antenna polarization, Tx-Rx pathloss and antenna element gain have been removed from the **H**-matrices by considering a common normalization factor, normalization (2), for all the configurations at each Rx grid. In this way, capacity is calculated so that it includes the impact of antenna polarization and array height on both subchannels' decorrelation and power. Figure 5-7 shows capacity CDFs for different antenna scenarios at different measurement locations. At Loc. 1 and Loc. 5, one antenna configuration was considered while for the rest of locations three configurations were measured. Comparing all the figures, the largest difference among CDFs of antenna configurations is about 5 bit/sec/Hz in after the curvature scenario and between MH/CV with MV configuration.

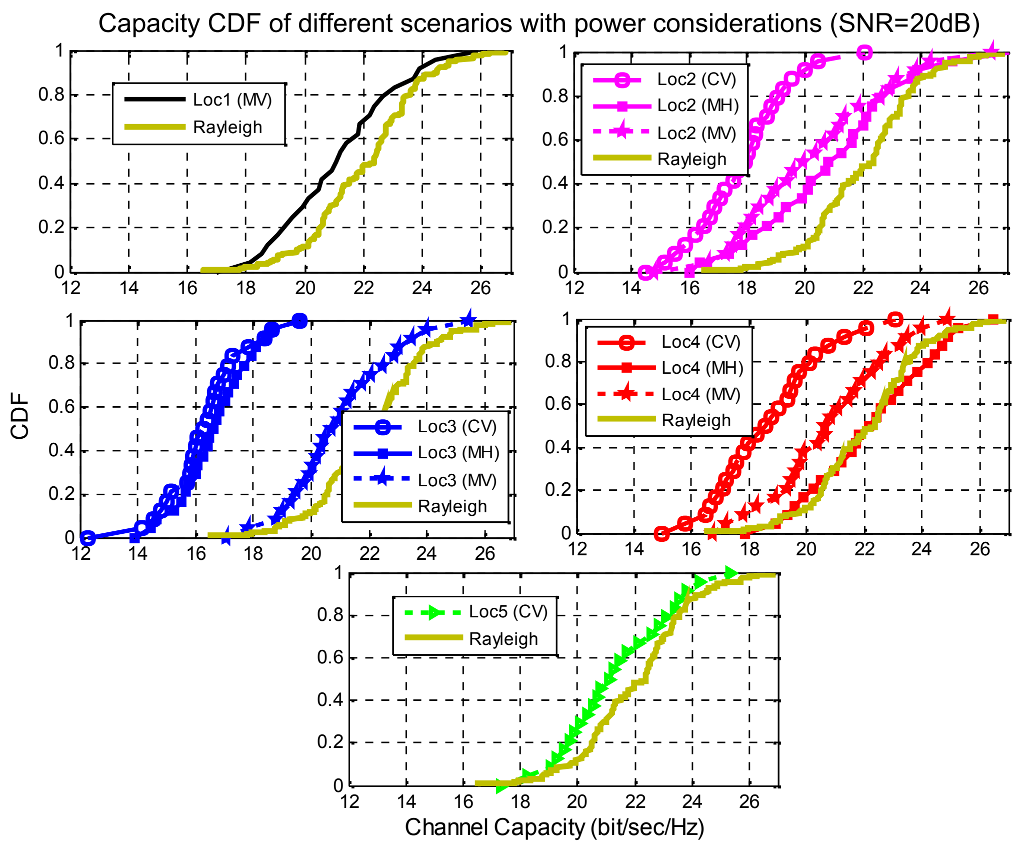

Figure 5-7 CDFs of 4×4-MIMO capacity with power considerations (based on the measurement).

5.4.2 Impact of Antenna Polarization

Figure 5-7 shows similar performance for MH and MV scenarios, however, The MH scenario has a slightly better capacity CDF (about 1 bit/sec/Hz) for both Loc. 2 (LOS) and

Loc. 4 (NLOS). This similar performance of two polarizations is likely due to the high depolarization in the near zone of the tunnel. However, because the aspect ratio of the tunnel is horizontal (*i.e.*, tunnel width is larger than tunnel height), horizontal polarization shows a bit lower attenuation in the near zone. Based on our results, this is only valid for the straight part of the tunnel. In Loc. 3, where a curvature exists between the transmitter and the receiver, MV shows the best performance by a large margin (5 bit/sec/Hz) for both MH and CV cases. Poor performance of MH in this case, can be attributed to the fact that horizontally polarized waves are attenuated more than vertical ones by the curvature, and thus the degradation of capacity can be due to the power loss.

Similar behaviour has been reported for horizontally polarized waves propagating in a subway tunnel, which is substantially larger than a typical underground mine [13]. Assume a rectangular tunnel as shown in Figure 5-8. Equations (6) and (7) give the attenuation of $\mathbf{EH}_{mn}$ mode (α_{mn}) in this tunnel for *y*-polarization (vertical polarization) and *x*-polarization (horizontal polarization), respectively [13],[123]:

$$\alpha_{mn}^{y} = \frac{2}{w}\left(\frac{m\lambda}{2w}\right)^2 \mathrm{Re}\left[\frac{1}{\sqrt{\varepsilon_w - 1}}\right] + \frac{2}{h}\left(\frac{n\lambda}{2h}\right)^2 \mathrm{Re}\left[\frac{\varepsilon_h}{\sqrt{\varepsilon_h - 1}}\right] \quad (6)$$

$$\alpha_{mn}^{x} = \frac{2}{w}\left(\frac{m\lambda}{2w}\right)^2 \mathrm{Re}\left[\frac{\varepsilon_w}{\sqrt{\varepsilon_w - 1}}\right] + \frac{2}{h}\left(\frac{n\lambda}{2h}\right)^2 \mathrm{Re}\left[\frac{1}{\sqrt{\varepsilon_h - 1}}\right] \quad (7)$$

where w, h, λ, ε_w and ε_h are tunnel width, tunnel height, wavelength, relative permittivity of vertical walls (sidewalls) and relative permittivity of horizontal walls (ceiling/floor), respectively. As can be seen from (7), vertical walls (sidewalls) on which horizontally polarized **E** is perpendicular to, contribute to most of the attenuation [123]. In [123], it is shown that if **E** is perpendicular to the curved walls, more attenuation occurs due to additional loss caused by the curvature. In fact, curvature of the sidewalls can be considered as a polarization filter that passes only vertically polarized waves, and its level of filtering is inversely proportional to the radius of the curvature.

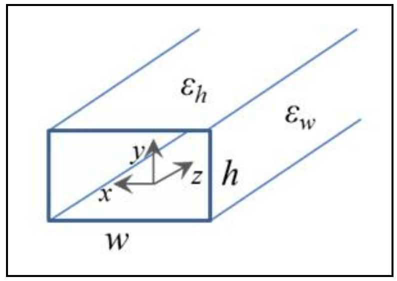

Figure 5-8 A tunnel with rectangular cross-section.

5.4.3 **Impact of Array Height**

For all the Rx locations with CV scenario, we can see that the ceiling height shows lower capacity compared to the middle height. Capacity median is found to be 2-5 bit/sec/Hz less at the ceiling height compared to the middle one (MV). Based on the waveguide theory, antenna located in the middle of the tunnel can couple higher power to the tunnel due to excitation and reception of the dominant propagation mode. Although it may not be practical to place the antenna array in the middle of the tunnel, this result suggests placing the antenna further from the ceiling for short underground tunnels. If this is not possible due to practical considerations, reduction on capacity should be taken into account while designing MIMO systems. This result may not necessarily be valid for very long Tx-Rx distances. Over very long distances (several hundred metres or more), only a limited number of waveguide propagation modes exist because the higher order modes are significantly attenuated. Higher order modes, acting like multipath components are an important factor to construct spatially decorrelated MIMO subchannels. Therefore, to excite higher order modes with sufficient energy to remain active for long distances, off-centered position of Tx and Rx arrays in the transverse plane may be preferred over centered position, as described in [24]. This implies that at far distances a trade-off may be required between subchannels' power and decorrelation.

To evaluate the results obtained in this section, Table 5-4 compares the mean pathloss between each Tx antenna and Rx grid for each measurement scenario. Free space pathloss which is calculated considering a longitudinal distance between the center of the transmitter array and center of the Rx grid, is also given. As it can be seen, MH shows the lowest pathloss at Loc. 2 and Loc. 4, while showing the highest one at Loc. 3 (after the curvature). We can also see relatively similar performance for both polarizations at Loc. 2 and Loc. 4, and better performance for the middle height compared to the ceiling height. These results match the results obtained from Figure 5-5, and thus confirm previous discussion on different power contribution of different array configurations.

Experimental results of capacity predictions with power considerations are compared with results from the multimode waveguide model for two LOS cases at 10 m and 27 m in the straight part of the mine. Figure 5-9 (a) and Figure 5-9 (b)-(d) compare capacity CDFs obtained by measurement and multimode model for Loc. 1 and Loc. 2, respectively. In Figure 5-9 (b)-(d), capacity CDFs from the multimode waveguide model for different heights and polarizations are obtained based on normalization (2). The experimental results match well with the theoretical results obtained for both locations, heights, and polarizations. This indicates that the multimode waveguide model can be considered as a simulation tool to effectively design and deploy advanced systems such as MIMO-based devices in mine tunnels.

Table 5-4 Mean pathloss measured at each Rx grid location in Myra-Falls mine (at 2.49 GHz).

		Mean Pathloss (dB)			Free Space Pathloss (dB)
Loc.1 LOS (10 m) MV	**Tx1_antenna1**	-62.31			-60.36
	Tx1_antenna2	-60.42			
	Tx1_antenna3	-59.64			
	Tx1_antenna4	-60.52			
		CV	**MV**	**MH**	
Loc.2 LOS (27 m) Before Curvature CV,MH,MV	**Tx2_antenna1**	-69.84	-68.19	-67.71	-69.00
	Tx2_antenna2	-69.71	-68.46	-68.54	
	Tx2_antenna3	-71.43	-69.89	-68.85	
	Tx2_antenna4	-71.24	-70.51	-68.73	
Loc.3 NLOS (49 m) After Curvature CV,MH,MV	**Tx3_antenna1**	-83.19	-78.62	-83.56	-74.17
	Tx3_antenna2	-81.66	-79.67	-82.04	
	Tx3_antenna3	-82.14	-77.59	-81.02	
	Tx3_antenna4	-83.08	-76.93	-82.00	
Loc.4 NLOS (12 m) CV,MH,MV	**Tx4_antenna1**	-80.30	-78.18	-77.79	-62.00
	Tx4_antenna2	-80.54	-78.63	-76.75	
	Tx4_antenna3	-80.05	-78.34	-77.64	
	Tx4_antenna4	-80.22	-79.57	-78.44	
Loc.5 LOS (21 m) Branch-Middle CV	**Tx5_antenna1**	-72.65			-66.82
	Tx5_antenna2	-70.97			
	Tx5_antenna3	-71.55			
	Tx5_antenna4	-68.08			

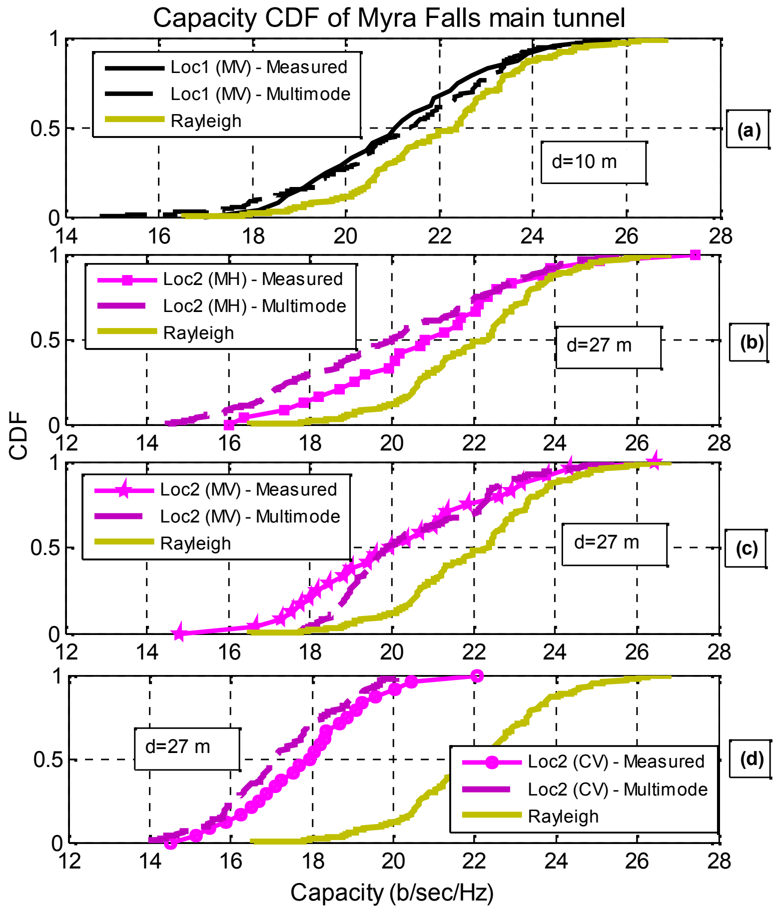

Figure 5-9 CDFs of 4×4-MIMO capacity with power considerations (based on measurement and multimode waveguide model at *f*=2.49 GHz, SNR=20 dB).

5.5 Conclusions

By this study, we showed that antenna array properties such as array orientation, height, antenna spacing, and polarization greatly impact the performance of MIMO systems in underground mines. Our experimental and theoretical analysis revealed that deploying 4-element ULAs with element separation of 2λ, horizontal orientation, and placed perpendicular to the tunnel axis provides a sufficient degree of decorrelation among subchannels to achieve a suitable MIMO capacity (close to that of an i.i.d. Rayleigh fading channel) in several propagation scenarios studied in a short underground mine tunnel.

We showed that if MIMO antenna arrays are deployed based on the proposed array orientation and interelement separation, array height and antenna polarization will mainly impact the power of the MIMO subchannels without significantly changing their spatial structure. This implies that by employing the proposed array design, one can choose other antenna properties (*e.g.*, antenna polarization, height) while devoting main focus on power aspects (similar to SISO systems) rather than concerning about the spatial correlation among the MIMO subchannels.

We also confirmed previous studies by showing that the mine geometry is a key factor that should be taken into account while designing wireless systems for underground tunnels. As an example, although in mines with a horizontal aspect ratio, horizontally polarized antennas show lower attenuation, and thus are more desirable, if a curvature exists between the transmitter and receiver, vertical polarization is preferred as it is much less affected by the curvature loss.

In spite of the dissimilarities between underground mines and tunnels, some of our results confirm and support results obtained in subway tunnels. Nevertheless, because underground mines are geometrically diverse, more measurement campaigns in various mines are required to reconfirm previous findings and reveal new physical trends or principles.

CHAPTER 6: CHARACTERIZATION OF ANGULAR SPREAD IN UNDERGROUND TUNNELS BASED ON A MULTIMODE WAVEGUIDE MODEL

6.1 Introduction

Research on wireless channel modeling allows the underground mining industry to save time in their wireless system deployments. Underground tunnels and mines have been intensively studied, both theoretically and experimentally, since the late 1970's. The main focus has been on the pathloss and delay spread, which are parameters of interest in single-input single-output (SISO) systems. For characterization of MIMO channels, however, the spatial domain becomes as important as the temporal domain. Similar to the power-delay-profile (PDP), the power-azimuth-spectrum (PAS) has been defined, which determines the spatial distribution of the received power in azimuth. Consequently, angular-spread (AS) is defined as the standard deviation of PAS, being equivalent to the root-mean-square (RMS) delay-spread of PDP [8]. AS is found to predict many properties of MIMO-based systems, *e.g.,* singular value and capacity distributions [9].

Because the AS is expected to be very different in mine tunnels compared to conventional indoor and outdoor environments, employing off-the-shelf MIMO products that are primarily designed for conventional environments may lead to poor performance in underground tunnels. As a result, conducting MIMO channel modeling and characterizing

AS allow suitable guidelines for designing MIMO antenna configurations customized for underground tunnels to be developed. Accordingly, deployment parameters such as separation of the antenna elements, antenna polarization, array arrangement, and transverse position can be determined.

For surface environments, AS and antenna configuration designs have been extensively studied for more than a decade. However, MIMO research, and in particular, antenna configuration design and characterization of angular spread for wireless propagation in tunnels and mines, is sparse, and related work in literature is limited. Recently, AS was experimentally studied in [128] for a large arched subway tunnel (8.6 m×6.1 m) with slightly rough walls (*i.e.,* roughness is less than 2 cm). However, no further investigations on angular spread characterization, such as finding a distribution fit for PAS inside a tunnel has been performed in previous studies.

In our study, we have used a theoretical model, multimode waveguide [70] and performed more comprehensive angular spread characterization. This theoretical model was chosen due to its accuracy and capability to model the near zone of tunnels. As previous studies [70],[75] show, for upper ultra-high-frequency (UHF) frequencies in tunnels, the multimode waveguide model is more accurate than its counterparts such as the single-mode waveguide model proposed by Emslie *et al*. [11], and dual-slope pathloss models (or breakpoint model) proposed by Zhang [114]. Additionally, unlike the single-mode waveguide model, multimode models includes higher order modes, and is therefore capable of characterizing both near and far zones of a tunnel.

Employing this model, we characterized the PAS, AS, and correlation coefficient observed by antenna elements within different zones in a tunnel, including close distances

(10 m- 50 m). These angular properties are found to be dependent on both the tunnel size and the tunnel zone, *i.e.*, the transmitter-receiver separation. We studied and compared them for two tunnel sizes and three zones inside the tunnel. Without loss of generality, we focused on short tunnels (less than 500 m) in this chapter. The same methodology can be applied to longer tunnels. The results of AS characterization can be used to extend the IEEE-802.11n MIMO channel model to underground mines or as the basis for other correlation-based MIMO channel models for underground tunnels. In addition to angular properties, we have characterized channel capacity for different interelement spacings and tunnel zones in order to evaluate the improvement in multiplexing gain that can be achieved in such confined spaces. We compared and validated our findings to experimental work presented in [128], and also to simulations using a ray-tracing based software (Wireless InSite from Remcom Inc.) [129].

The remainder of this chapter is organized as follows. In Sec. 2, the multimode model is introduced. In Sec. 3, assessment of angular properties and channel capacity based on the multimode waveguide model is presented. In Sec. 4, results and model validation are discussed. Finally, in Sec. 5 we summarize our key findings and contributions.

6.2 A Multimode Waveguide Model

Multimode modeling has been developed and used by Sun *et al.* [70] to characterize wireless propagation in tunnels. In this model, a tunnel is considered to be an oversized dielectric waveguide. Here, we assume that the *x*-axis is along the tunnel's width, the *y*-axis is along its height and the *z*-axis is along its length. Considering a *y*-directed (vertically polarized) dipole as a source of excitation, the field distribution of *y*-polarized hybrid modes at any position (x, y, z) inside the tunnel, can be found by solving Maxwell's equations for the specified cross-sectional dimensions and the material of the tunnel in terms of eigenfunctions as follows [70],[130]:

$$E_{m,n}^{eigen}(x, y) = \cos\left(\frac{m\pi}{w} x + \varphi_x\right)\sin\left(\frac{n\pi}{h} y + \varphi_y\right) \tag{1}$$

where w and h are width and height of the tunnel, respectively, and φ_x and φ_y are parity designations that take values of 0 or π/2 depending on whether the integer values of m and n are even or odd [130]. It is assumed that the co-polarized field components play a dominant role and the cross-polarized components can be ignored. The intensity of each mode depends on the excitation, which can be found by applying a geometrical-optical (GO) model in the excitation plane (transmitting plane), *i.e.*, the cross-sectional plane that contains the transmitting (Tx) antenna. The electromagnetic (EM) field distribution in the transmitting plane is, in fact, the weighted sum of the field of all modes. The mode intensities are then estimated by a mode matching technique as given in (2) [70] assuming that transmitter is vertically polarized (y-polarized) and located at (x_0, y_0, z_0).

$$E^{Rx}(x, y, z) = \sum_{m=1}^{\infty}\sum_{n=1}^{\infty} C_{mn}(x_0, y_0)\, E_{m,n}^{eigen}(x, y)\, e^{-(\alpha_{mn} + j\beta_{mn})|z - z_0|} \tag{2}$$

where C_{mn}, α_{mn} and β_{mn} are the mode intensity on the excitation plane (which depends on the transmitter location), attenuation coefficient and phase shift coefficient, respectively.

We have employed this model in our characterization of the angular properties and MIMO channel capacity in underground tunnels. Verification of the multimode model with experimental work performed in [13] is given in Figure 6-1. For this verification, both antennas were vertically polarized and placed at a height of 2-m at the same horizontal location at a distance 1/4 of the tunnel width from the tunnel sidewall.

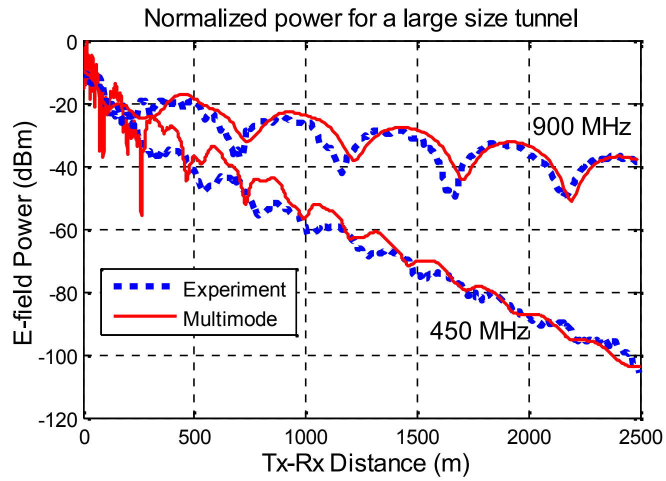

Figure 6-1 Comparison of multimode model with experimental work obtained from [13].

6.3 Angular Spread and Capacity Characterization Based on a Multimode Waveguide Model

6.3.1 Angular Spread Characterization Based on a Multimode Waveguide Model

In this section, we use the multimode waveguide model to characterize angular spread in a rectangular tunnel. We calculate the azimuth angle of the propagating rays inside a tunnel. Then, we find the PAS and determine the correlation coefficient of antenna elements in a uniform-linear-array (ULA).

6.3.1.1 *Power Angular Spectrum*

To find the distribution of received signal strength versus angle-of-arrival (AOA) in both the azimuthal and elevation planes, we use equations for a rectangular waveguide.

Azimuth AOA (AOA-φ) and elevation AOA (AOA-θ) of each propagation mode (m, n) can be calculated using the following equations [131]:

$$\begin{cases} \sin(\varphi_m) = \dfrac{m\lambda}{2w} \\ \sin(\theta_n) = \dfrac{n\lambda}{2h} \end{cases} \tag{3}$$

where φ, θ, λ are the azimuth angle, elevation angle and wavelength, respectively. Azimuth angles of two waveguide modes that use sidewalls to propagate are illustrated in Figure 6-2. Angle (φ or θ) is a function of mode index (m or n), transverse dimension of the tunnel (w or h) and operation frequency. Their power is additionally dependent on the positions of transmitter and receiver, and can be found from $\left|E^{Rx}\right|^2$, using (2) at each receiver point (x,y,z).

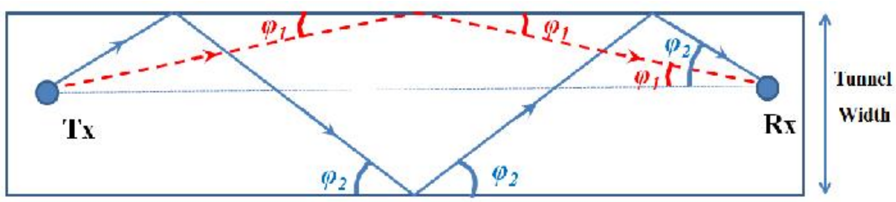

Figure 6-2 Reflection angles of lower and higher order modes from sidewalls in a waveguide (φ_1 is the angle for the lower order and φ_2 is for the higher order mode).

6.3.1.2 *Correlation Coefficient of Antenna Elements*

Space selective fading caused by AS makes signal amplitude dependent on the location of the antenna [10]. The parameter that characterizes space selective fading is the coherence-distance (D_C) that is inversely proportional to the AS. It is defined here as the spatial separation for which the autocorrelation coefficient of the spatial fading drops to 0.7. In general, for a ULA with d separation between antenna elements, Pearson's correlation can be obtained as follows [132],[133]:

$$\rho = R_{XX}(D) + jR_{XY}(D) \qquad D = \frac{2\pi d}{\lambda}$$

$$\begin{cases} R_{XX}(D) = \int_{-\pi}^{\pi} \cos(D \sin \varphi) PAS(\varphi)\, d\varphi \\ R_{XY}(D) = \int_{-\pi}^{\pi} \sin(D \sin \varphi) PAS(\varphi)\, d\varphi \end{cases} \tag{4}$$

where λ, ρ, φ, and PAS are the wavelength, correlation coefficient, angle of arrival, and power-azimuth-spectrum, respectively. Using (4), the envelope correlation $|\rho|$ vs. antenna element separation (d/λ) can be plotted, which provides useful information for antenna array design.

6.3.2 H-Matrix and MIMO Channel Capacity

To construct MIMO matrices (**H**), formula (1) was substituted into (2) to find the channel coefficients as follows:

$$h_{ij} = \frac{\sqrt{G_{Tx} G_{Rx}}}{2k} \sum_{m=1}^{\infty} \sum_{n=1}^{\infty} C_{mn}^{j}(x_j, y_j) E_{m,n}^{eigen}(x_i, y_i) e^{-(\alpha_{mn} + j\beta_{mn})|z_i - z_j|} \tag{5}$$

where i is receiver index, j is transmitter index, h_{ij} is complex channel gain between i^{th} receiver and j^{th} transmitter, G_{Tx} and G_{Rx} are transmitter and receiver antenna gains, k is the wave number, C_{mn}^{j} is the mode intensity of j^{th} transmitter and $E_{m,n}^{eigen}(x_i, y_i)$ is the value of (m, n) mode eigenfunction at i^{th} receiver. After constructing **H**-matrices, capacity (in bit/sec/Hz) that is a fundamental property of MIMO-based systems can be calculated as follows [6]:

$$C = \log_2\left[\det\left(\mathbf{I}_{N_{Rx}} + \frac{SNR}{N_{Tx}} \mathbf{H}\mathbf{H}^*\right)\right] \quad \text{bit/sec/Hz} \tag{6}$$

where * denotes conjugate transpose, N_{Tx} is the number of transmitter antennas, N_{Rx} is the number of receiver antennas, **H**, h_{ij} and **I** are the normalized channel coefficient matrix, channel matrix entries and identity matrix, respectively. **H**-matrices are normalized by their own Frobenius norms, and therefore, are only affected by the level of correlation experienced at the antennas. This formula is used to find the channel capacity distribution and variation of capacity vs. distance.

6.4 Results and Validation of Multimode Modeling

6.4.1 **Simulation Scenarios**

In our simulation setups, we considered omni-directional antennas with vertical polarization for both transmitter and receiver, which are located in the middle of the tunnel under study. While most results are obtained for a small tunnel with a typical cross-sectional size of underground mines, we have also considered a larger tunnel size (subway tunnel) both with the same length of 500 m. Two tunnel sizes were considered to: 1) compare our work with a previously published work in which wireless propagation in a subway tunnel was studied, and 2) study the impact of the tunnel size on the angular properties.

The two tunnels have following dimensions: 1) a small rectangular mine tunnel with 3.8 m height and 5.1 m width (dimensions of an underground mine at Myra Falls on Vancouver Island), and 2) a large subway tunnel with semi-circular cross-section that is experimentally studied in [128]. As shown in Figure 6-3, the diameter of the cylindrical part of the subway tunnel is 8.6 m, the maximum height is 6.1 m at the centre of the tunnel and the roughness of the walls is quite low, in the order of less than 2 cm (0.16λ). A rectangular equivalent of this tunnel is shown in Figure 6-3. To validate our angular spread characterization based on the multimode model, we compared our results to results obtained using a ray-tracing tool [129] and to experimental work presented in [128].

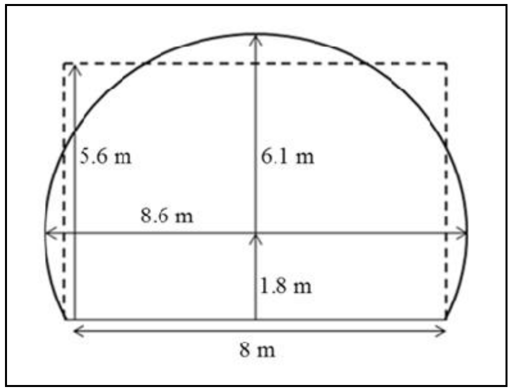

Figure 6-3 The cross-section of the subway tunnel and its equivalent rectangle.

6.4.2 Characterization of PAS and AS

6.4.2.1 *Simulation Setup*

To find the PAS in a tunnel, first based on the tunnel size and operating frequency (2.4 GHz), propagating modes and their corresponding angles can be found. Then, the power of modes, which is dependent on the Tx and Rx locations should be found. Therefore, a transmitter and a grid of receivers are located at the middle height (y=0). The transmitter is located at (0,0,0) and the receiver grid is considered over the area of $x \in \left[-\frac{w}{4} : 2^{a} : \frac{w}{4}\right]$, $z \in [10m : 1m : 500m]$. To find the PAS at each receiver point, the power of each propagating mode has been calculated. To plot the AS at each longitudinal distance (along the z-axis), the AS was averaged over the tunnel width (along the x-axis).

After finding the power of corresponding azimuth angles, by using an iterative least-mean-square (LMS) distribution fitting, the PAS for different zones has been estimated and modeled by a Gaussian function as follows:

$$p(\varphi) = \frac{1}{\sigma_\varphi \sqrt{2\pi}} e^{-\frac{1}{2}\left(\frac{\varphi - \mu_\varphi}{\sigma_\varphi}\right)^2} \quad (7)$$

where φ, σ_φ and μ_φ are azimuth angle, azimuth AS and mean AOA, respectively. By finding the standard deviation (*i.e.*, AS) and mean of the Gaussian function, the Gaussian fit can be plotted. Figure 6-4 shows Gaussian distribution fitted to PAS obtained by multimode simulation for the small tunnel.

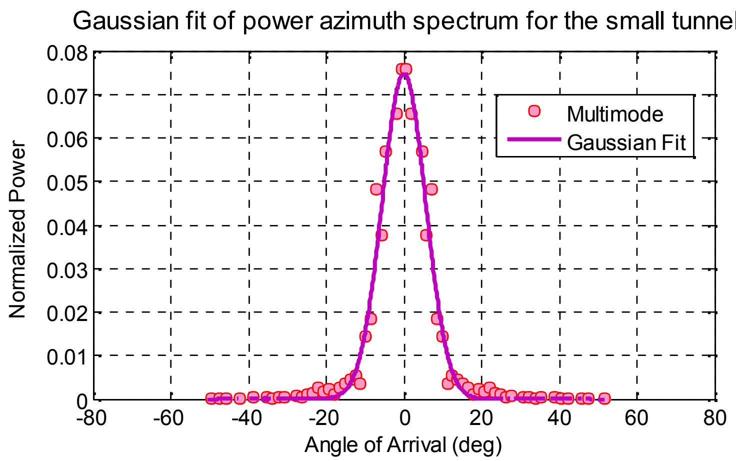

Figure 6-4 Zero-mean Gaussian fit of the PAS for the small tunnel (multimode waveguide model).

Graphs in Figure 6-5 show Gaussian fits to the PAS for different zones of the small and large tunnels. The Gaussian fits have zero-means, because the direct path between the transmitter and the receiver is taken as the reference. Similar trends can be seen for both tunnels and their corresponding zones; the further the distance, the smaller the AS. The largest difference can be seen in the near zone, and the smallest is observed in the far zone. For the tunnel with larger cross-section, AS is larger, however, in the far zone impact of the cross-section is less, and both tunnels show very similar AS. Larger AS in the near zone is due to the fact that more higher order modes are active in this region.

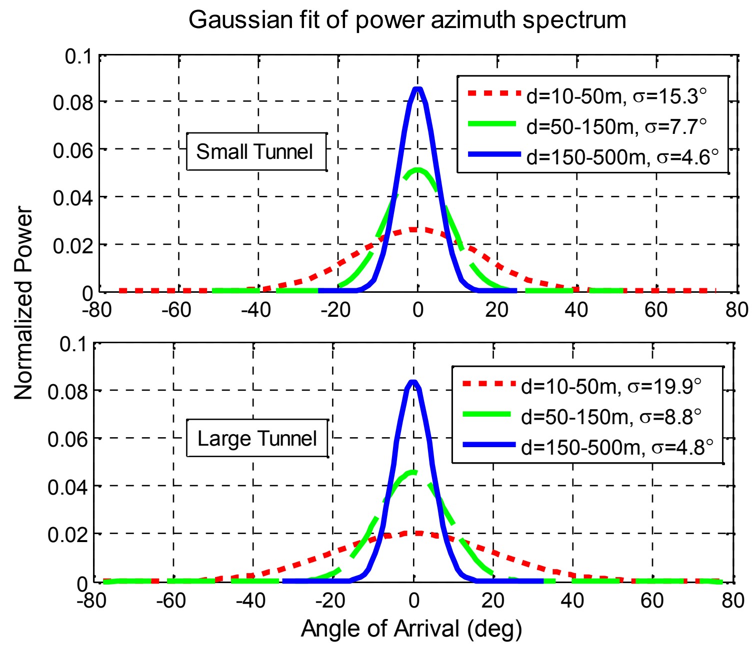

Figure 6-5 Zero-mean Gaussian fit of the PAS for different zones of two tunnel sizes (multimode waveguide model).

6.4.2.2 *Validation by the Ray-Tracing Method*

Using the ray-tracing tool, similar results and same trend have been observed for the scenarios studied by the multimode model. Figure 6-6 compares the PAS for the entire small tunnel obtained by both methods. As can be seen from this figure, two curves match quite well but the angular spreads are slightly different. More detailed results are summarized and compared in Table 6-1. Both methods show similar values in different tunnel zones; however, angular spreads obtained by the ray-tracing method are slightly larger than the ones obtained by the multimode model. Based on these results, PAS can be modeled by a truncated-Gaussian function with zero-mean and AS between 4.5^{o} and 23^{o}, depending on the tunnel zone and transverse dimension.

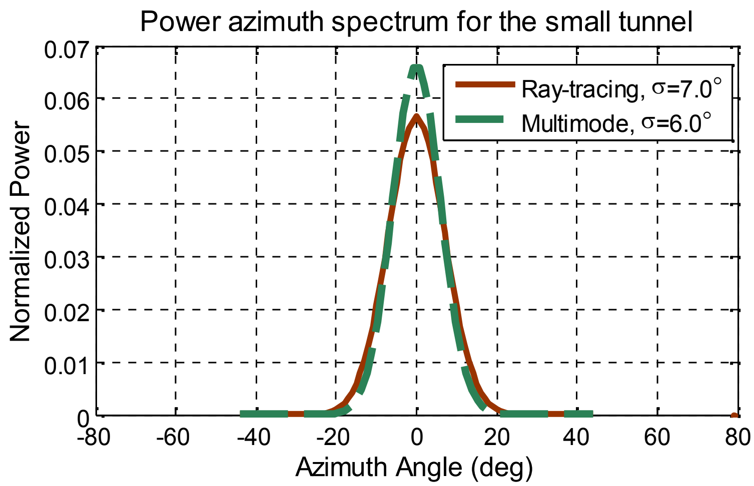

Figure 6-6 **Comparison of PAS obtained by multimode and ray-tracing for the small tunnel (whole tunnel).**

Table 6-1 **Angular spreads (deg) for different zones of the large and small tunnel obtained by multimode and ray-tracing methods.**

	Large Tunnel (Subway)		**Small Tunnel (Underground mine)**	
	Multimode	**Ray-tracing**	**Multimode**	**Ray-tracing**
Close Distance 10 m-50 m	19.9^o	22.3^o	15.3^o	16.6^o
Middle Distance 50 m-150 m	8.8^o	9.7^o	7.7^o	7.6^o
Far Distance 150 m-500 m	4.8^o	6.9^o	4.6^o	6.0^o
Whole Tunnel 10 m-500 m	6.9^o	7.7^o	6.0^o	7.0^o

6.4.3 Characterization of AS vs. Distance

Figure 6-7 shows AS vs. Tx-Rx distance for the small and large tunnels. As can be seen in the near zone of both tunnels, AS is a decreasing function of distance, and in the far zone, it remains constant at a small value (4^o). Unlike lower order modes that arrive with grazing angles, higher order modes undergo large number of bounces and are greatly attenuated, thus they do not contribute much in AS at long distances. Therefore, AS decreases as distance increases. This small AS, which is much smaller than AS of conventional indoor environments (*i.e.*, 12°-40°) [132],[134] requires different MIMO antenna configuration design for underground tunnels than are used in conventional environments.

Higher order modes are stronger in the near zone of larger tunnels, and therefore, their AS is expected to be larger in that area. This is confirmed by the results presented in Figure 6-7. Over the span 10 m-150 m, the impact of tunnel size on the AS is large. But after about 150 m, it gradually becomes insignificant and both tunnels show almost the same AS, and finally, it becomes independent of the tunnel transverse dimension.

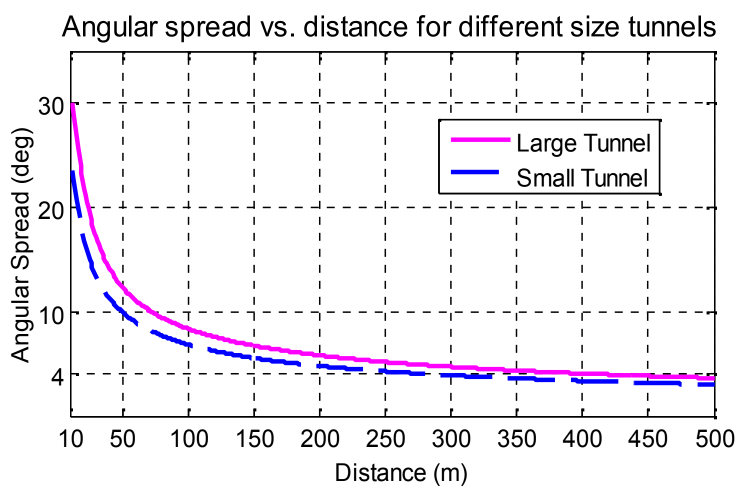

Figure 6-7 AS variation over distance for two tunnel sizes (multimode waveguide model).

6.4.3.1 *Validation of AS vs. Distance by Ray-Tracing Method*

Figure 6-8 compares three methods for characterizing AS vs. Tx-Rx distance for the large subway tunnel (8 m×5.6 m). As it can be seen, all methods similarly show the same trend of rapid decrease before the breakpoint and slow decrease afterwards. Unlike the experimental result, which captures constructive and destructive interactions among the rays, both multimode and ray-tracing models characterize AS as a monotonically decreasing function of distance. In addition, both slightly overestimate the AS for a measured channel in an arched tunnel [128]. This deviation from the experimental results can be attributed to the shape of the actual tunnel (*i.e.*, not being rectangular) and its walls (*i.e.*, not being entirely smooth). The antenna directivity can also be another impacting factor. In fact, the accuracy of measurement-based characterization of angular properties is highly dependent on the antenna directivity.

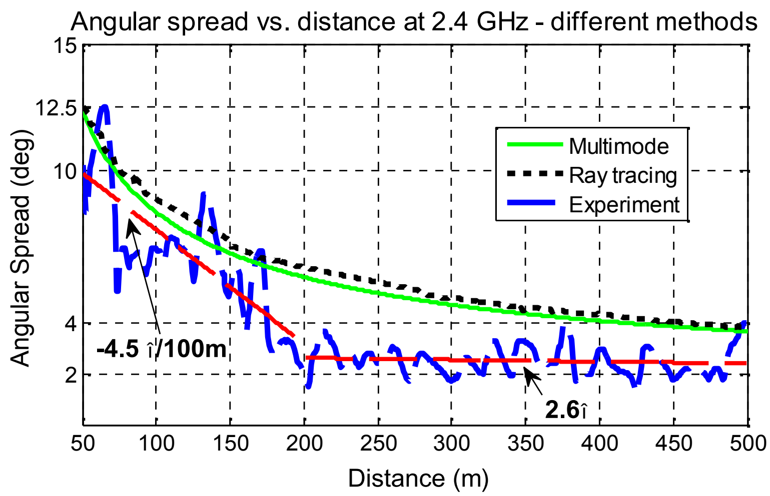

Figure 6-8 **Comparison of three methods for characterizing AS in a large tunnel (ray-tracing and experiment graphs are obtained from [128]).**

In Figure 6-8, we can also identify a breakpoint at a distance of about 200 m from transmitter, which distinguishes two zones of the tunnel. The first zone can be modeled by a regression line with a slope of 4.5^{o}/100 m, and the second zone by a regression line with a zero slope at 2.6^{o} (mean value of AS) that remains constant for the entire region. By including the near zone of 10 m-50 m in multimode and ray-tracing simulations, a more complete picture of angular properties can be obtained compared to previous study presented in Figure 6-8. Based on both methods, in this zone, AS is large and close to that of rich scattering indoor environments, however, as the distance increases it dramatically drops with a much sharper slope compared to other zones. Therefore, three zones can be identified for this tunnel: (1) 10 m- 50 m, with very sharp decrease of AS, (2) 50 m-150 m, with medium decrease of AS, and (3) 150 m-500 m, with constant AS.

6.4.3.2 *Comparison with Other Environments*

As was shown in Figures 6-8 and 6-9, AS is found to be a decreasing function of distance in tunnels based on different methods employed in our study and in [128]. Unlike this consistent results, showing AS dependency on the distance in tunnels, for outdoor environments conflicting results have been reported on distance-dependency of AS [8],[135],[136]. Based on the literature, PAS has been characterized and modeled as uniform, truncated-Gaussian and truncated-Laplacian distributions [8],[136]-[138] for different indoor and outdoor scenarios. Local features that can vary by antenna height [8], and also distribution of scatterers around the receiver and transmitter have been found to be key factors in determining angular properties of a propagation environment.

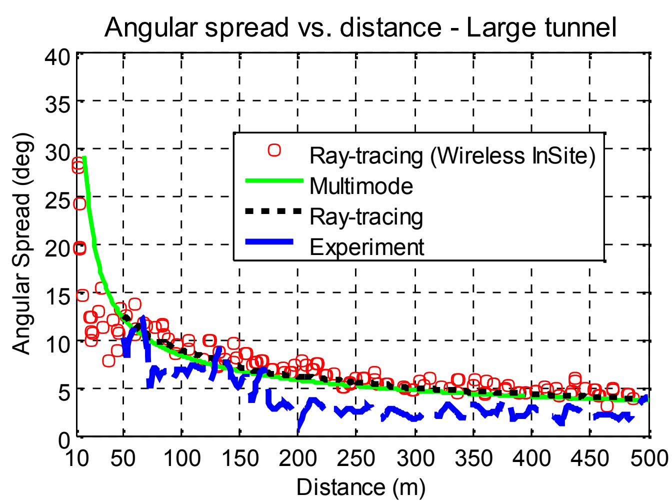

Figure 6-9 Comparison of different methods for characterizing AS in a large tunnel, including 10 m-50 m zone (ray-tracing and experiment graphs are obtained from [128]).

In Table 6-2, the angular properties of several environments are summarized for comparison purposes. For outdoor environments, in most scenarios of both urban and rural, measured PAS has been fitted to a Laplacian function [8] for some cases Gaussian distribution has also been obtained [8],[138]. For rural areas, AS at the base station is very small and about 2^o. In macro-cellular urban situations, depending on the antenna height, median AS varies between 5^o to 10^o (larger for shorter height) [8]. For indoor environments, PAS can be modeled by Laplacian or Gaussian distribution with AS=12^o in line-of-sight (LOS) scenarios, and a uniform distribution in non-LOS scenarios (if distribution of scatterers is uniform) [8]. Although, tunnels are confined spaces and have small AS, our results show larger AS compared to macro-cellular base stations in rural areas (AS=2^o), in particular in near zone. In near zone, AS is close to that of indoor but in the far zone, it is far less than typical AS in indoor environments.

Table 6-2 Comparison of AS for different environments.

	PAS	AS	Ref.
Indoor	Uniform, Gaussian, Laplacian	12^o-40^o	[137]
Urban	Mostly Laplacian (some cases: Uniform and Gaussian)	5^o-10^o	[8],[136], [139]
Rural	Laplacian	2^o	[7]
Tunnels	Gaussian	Near zone=15^o-23^o Far zone=4.5^o-5^o	Our study

For any PAS model chosen for a wireless propagation environment, a physical justification can be given. For example, physical explanation for a Laplacian distribution modeling the PAS of a LOS indoor scenario is given in [139]. Reflections from distant scatterers located further around the transmitter and away from the receiver arrive primarily from one direction with a narrow AS, while reflections of the local scatterers give rise to a large AS. This phenomenon results in a Laplacian distribution with high occupancies at the central angle and lower ones at the larger angles [139]. In tunnels, on the other hand, due to the presence of walls between the transmitter and the receiver, there is more than one strong ray about 0^{o}, the direct path between the transmitter and the receiver, as well as reflections from the sidewalls, which can give rise to a Gaussian distribution. Depending on the location of the receiver respect to the transmitter (or tunnel zone), the standard deviation of the corresponding Gaussian distribution is different. In the near zone, AS is large because of strong reflections coming from various angles, while in the far zone, it is small because of grazing incidence phenomenon, causing rays to arrive with angles very close to that of the direct path, *i.e.*, 0^{o}.

6.4.4 Antenna Interelement Spacing

Pearson's correlation coefficient can be obtained from (4). In Figure 6-10, correlation coefficient of the ULA antenna elements for different zones of two tunnels has been obtained. For each zone, the zero-mean Gaussian fit of the corresponding PAS (with different standard deviations) has been considered. The results are compared for two tunnel transverse sizes (5.1 m×3.8 m and 8 m ×5.6 m). As it can be seen, the largest difference between the two tunnels in terms of correlation coefficient is in the near zone, where higher order modes, which are dependent on the tunnel transverse size, are active and significantly impact the AS. On the other hand, in the far zone, where only lower order modes are active, for the same antenna interelement separation, the correlation coefficient in both tunnels is very similar.

For each zone, different interelement separation can be determined as the PAS for each is different. From Figure 6-10, it is clear that $\lambda/2$ separation, which is a common spacing for IEEE-802.11n-based off-the-shelf products, does not provide decorrelated MIMO subchannels for most parts of both tunnels, and therefore, may not offer desirable capacity (close to that of an i.i.d. Rayleigh fading channel). This fact will be confirmed in the following sections. By increasing the separation, lower correlation coefficient can be achieved. Capacity results presented in the next section confirm our results here. As we will see by applying 2λ separation, the mean capacity remains constant for the zone less than 150 m and starts to decrease afterwards. However, by applying larger separations (*e.g.*, 4λ and 6λ), the mean capacity remains constant for all the zones (10 m- 500 m).

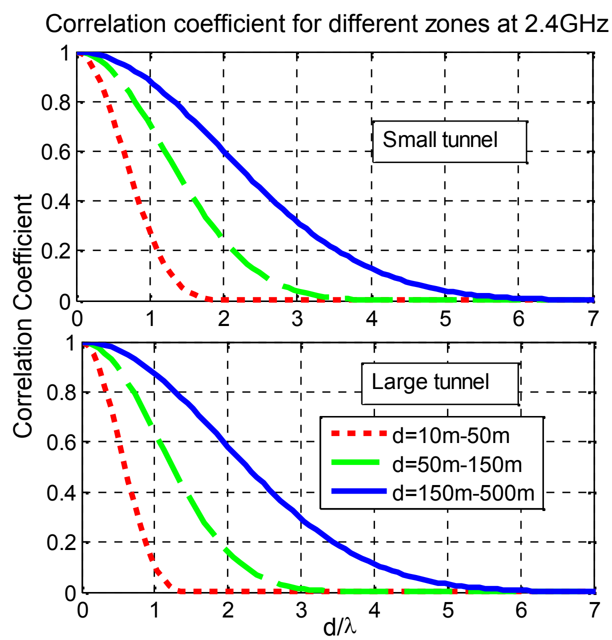

Figure 6-10 Correlation coefficient of ULA antennas vs. their separation for small and large tunnels across 10 m-500 m distance (multimode waveguide model).

In [140], an expression is derived, which relates the antenna spacing of a ULA to their correlation coefficient in an environment with Gaussian PAS. For a planar wave that arrives from angle φ with respect to the normal to the array axis, assuming a Gaussian PAS and $\sigma_\varphi << 25^o$, the required separation to ensure correlation of $|\rho|$ can be approximated by [140]:

$$\frac{d}{\lambda} = \frac{\sqrt{-2\ln(|\rho|)}}{2\pi\sigma_\varphi \cos(\mu_\varphi)} \qquad (8)$$

where d, $|\rho|$, μ_φ and σ_φ are antenna separation, envelope correlation between two successive antenna elements on the array, mean AOA (radians) and AS (radians), respectively. Because we found the PAS in tunnels follows a Gaussian distribution with angular spreads much less than 25^o for most parts, (8) can also be used to calculate ULA antenna spacing. For a given antenna separation, correlation coefficient obtained by formula (8) matches the one obtained from Figure 6-10.

6.4.5 Characterization of MIMO Channel Capacity

6.4.5.1 *Simulation Setup*

To characterize the channel capacity, 4×4-MIMO matrices (**H**) were constructed across the tunnel, **H**-matrices are normalized to their Frobenius norm, the operating frequency is considered to be 2.4 GHz, and the SNR is assumed to be fixed and equal to 20 dB. To find the 4×4-MIMO capacity, the transmitting and receiving ULAs are placed horizontally at the middle height (y=0). For the transmitter, a 4-element array is considered, which was placed perpendicular to the tunnel axis, and in the middle of the tunnel. For the receiver, 4-element ULAs whose centres were located in an area of $x \in \left[-\frac{w}{4} : 2\lambda : \frac{w}{4}\right]$, $z \in [10m : 1m : 500m]$ were considered. The orientations were the same for the receiver and the transmitter ULA. Intuitively, the chosen orientation for the ULA will provide optimum performance because it occupies the largest space orthogonal to the arriving signals. In the assessment of capacity, complementary-cumulative-distribution-functions (CCDF) of all the capacities calculated in this area are considered, while for the mean capacity over distance, at each longitudinal distance (*z*-axis) capacity was averaged over the tunnel width (*x*-axis).

6.4.5.2 *Mean Channel Capacity vs. Distance*

In this section, we evaluate 4×4-MIMO capacity vs. distance for several antenna spacings at SNR=20dB. Figure 6-11 compares capacity as a function of transmitter-receiver distance for four interelement separations based on the multimode model. As it can be seen, for λ/2 interelement separation, capacity reduces with a sharp slope for very close distances (10 m-20 m). As Tx-Rx distance increases, the reduction rate gradually becomes less, and finally becomes almost zero. The same behaviour was observed for the AS of the small tunnel in Figure 6-8, which confirms the existence of high correlation between the channel capacity and the AS of the surrounding environment. For 2λ separation, mean capacity decreases with a lower slope and for larger separations (4λ and 6λ) the reduction rate becomes zero, and accordingly more consistent capacity can be achieved. These results reveal that λ/2 interelement separation shows lower capacity compared to the larger separations for most locations inside the tunnel, however, for very close distances (10 m-20 m), due to sufficiently large AS, λ/2 separation also shows high capacity.

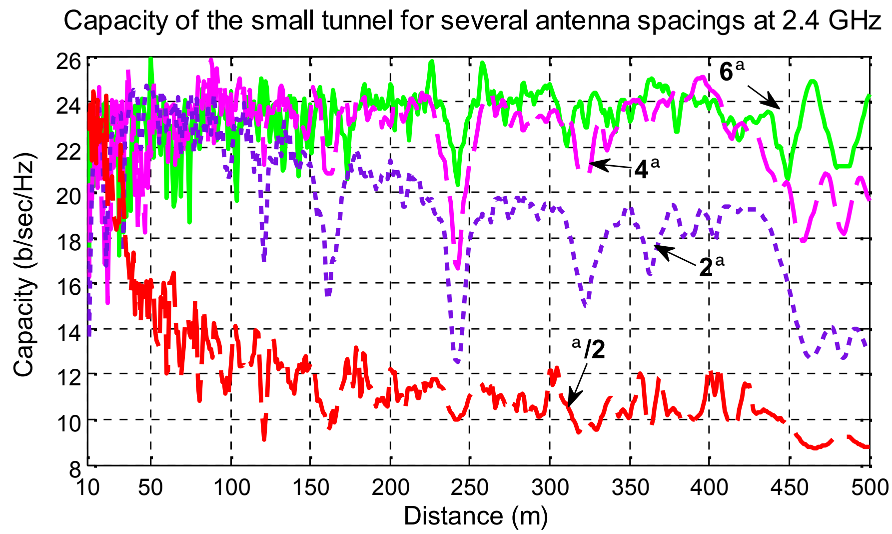

Figure 6-11 Comparison of 4×4-MIMO capacity vs. Tx-Rx distance for 4 antenna spacings (SNR=20 dB).

6.4.5.3 *MIMO Capacity CCDF*

In this section, we find 4×4-MIMO capacity CCDFs at different tunnel zones and for several antenna spacings at SNR = 20dB. This can help to assess and quantify the median and outage capacity improvement by increasing the interelement separation at different tunnel zones: (1) 10 m-50 m, (2) 50 m-150 m, and (3) 150 m-500 m. The results are summarized in Table 6-3. Based on these results, we can quantify the improvement of median and %10 outage capacity achieved by increasing the interelement separation from λ/2 to 2λ, 4λ, and 6λ.

As can be seen, significant improvement in capacity statistics can be observed by increasing the separation from λ/2 to 2λ. By increasing the spacing to 6λ, further improvement can be achieved, and capacity statistics becomes constant over the whole tunnel regardless of region. As a result, the increase in antenna spacing not only increases the median and 10% outage capacity, but also increases the performance (capacity) consistency for different longitudinal distances. To have a better comparison, Figure 6-12 is presented, which shows capacity CCDFs for two interelement separations of λ/2 and 6λ in different tunnel zones. In the near zone, capacity is higher due to the larger AS, resultant from larger number of active propagation modes compared to the far zone. Therefore, in 10 m-50 m region, CCDFs of both spacings (λ/2 and 6λ) are closer than those of other zones, meaning that the capacity in this area is less affected by the array element spacing.

Considering the CCDFs given in Figure 6-12 and Table 6-3, for the entire region (10 m-500 m), we can see that for λ/2 antenna separation (off-the-shelf products) the %10 outage capacity is 9 bit/sec/Hz, while for 6λ, it is 20.7 bit/sec/Hz. Therefore, 11.7 bit/sec/Hz improvement on %10 outage capacity can be achieved by increasing separation to 6λ. Similarly, improvement of the median capacity is found to be 12.6 bit/sec/Hz. Additionally, difference of outage capacities, and also median capacities in different zones become insignificant (more consistency across the tunnel).

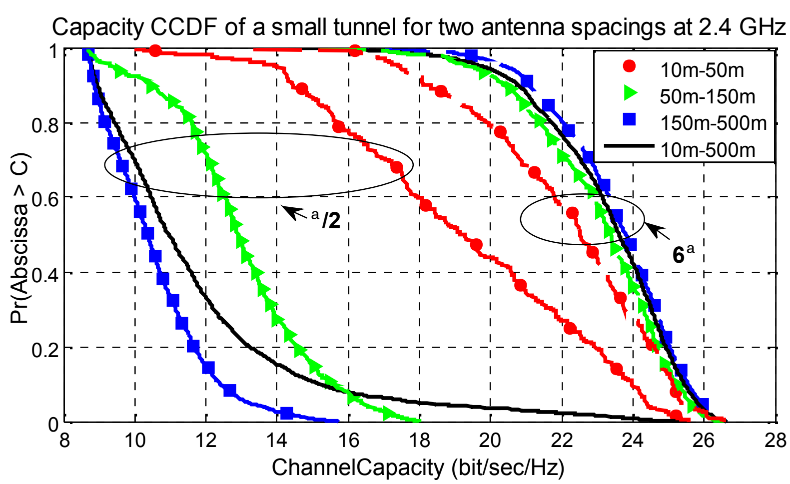

Figure 6-12 4×4-MIMO capacity CCDFs for several zones (10 m- 500 m) and two interelement separations of λ/2and 6λ (SNR=20 dB).

Table 6-3 Median and 10% outage 4×4 MIMO capacity (bit/sec/Hz) at SNR=20 dB for several interelement spacings and different zones of the small tunnel.

Distance (m)		10 -50	50-150	150-500	10-500
λ/2	C_{out}	14.7	10.5	8.9	8.9
	C_{median}	19	12.8	10.4	11
2λ	C_{out}	17.4	19.2	13.3	14
	C_{median}	22.8	22.8	18.4	19.3
4λ	C_{out}	17	21	18.8	19
	C_{median}	21	23.7	22.8	22.9
6λ	C_{out}	18	20.4	21	20.7
	C_{median}	22.5	23.3	23.7	23.6
i.i.d. Rayleigh	C_{out}	21	21	21	21
	C_{median}	24	24	24	24

6.5 Extension of the IEEE 802.11n MIMO Channel Model to Underground Mines

The MIMO channel model developed by the IEEE 802.11n channel modeling committee can be extended to underground mines using the results presented here together with a model for the channel impulse response. Using the PAS shape, AS, mean angle-of-arrival (AoA), and individual tap powers, correlation matrices of each tap can be determined as described in [132]. For the uniform linear array (ULA), the complex correlation coefficient at the linear antenna array is expressed as:

$$\rho = R_{XX}(D) + jR_{XY}(D) \tag{9}$$

where $D = \frac{2\pi d}{\lambda}$ and R_{XX} and R_{XY} are the cross-correlation functions between the real parts (equal to the cross-correlation function between the imaginary parts) and between the real part and imaginary part, respectively, with:

$$
\begin{cases}
R_{XX}(D) = \int_{-\pi}^{\pi} \cos(D \sin\phi) PAS(\phi)\, d\phi \\
R_{XY}(D) = \int_{-\pi}^{\pi} \sin(D \sin\phi) PAS(\phi)\, d\phi
\end{cases}
\tag{10}
$$

6.6 Conclusions

This chapter has focused on theoretical MIMO channel characterization, with particular interest on characterization of angular properties in underground mine tunnels. Angular properties, correlation of array elements and channel capacity for different tunnel zones have been studied based on the multimode waveguide model.

Based on our study, we conclude that the PAS inside a tunnel can be modeled by a zero-mean truncated-Gaussian function with an azimuth AS between 4.5^{o} and 23^{o}, depending on the Tx-Rx distance and the transverse dimension of the tunnel. For the near zone, the AS is large and for the far zone, it is small. For different zones and also for the entire tunnel, we found that the AS found is slightly larger in tunnels with larger transverse dimension. However, as Tx-Rx distance increases, the difference between AS of different size tunnels becomes insignificant, and therefore, it becomes independent of tunnel size.

For a typical mine size, multimode waveguide model predicts that AS starts at about 24^{o} at close distances to the transmitter (10 m), decreases with a sharp slope, and remains constant equal to 4^{o} at about 200 m away from the transmitter. Small AS for most parts of the mine, which is much smaller than AS of indoor environments (12^{o}- 40^{o}) requires customized MIMO antenna configuration design for underground tunnels. Our study shows that by careful antenna design and deployments, small AS (channel impairment for MIMO systems) can be overcome, and mining industry can benefit from MIMO technology for underground communications.

Several spacings (2λ, 4λ, and 6λ) at the transmitter and the receiver were chosen for performance assessment and comparison. Based on the correlation and capacity analysis, we found that λ/2 separation offers poor performance for a 4×4-MIMO system in most parts of the tunnel, and therefore, the element spacings of the array should substantially be increased to achieve desirable performance everywhere inside the tunnel, including at large Tx-Rx distances (more than 300 m). The choice of antenna separation for the ULA can differ depending on the transverse dimension and the coverage area inside the tunnel.

By increasing the interelement separation, capacity CCDFs show smaller standard deviation (less steep). This implies that larger separations not only offer higher median and outage capacity but also higher reliability (smaller standard deviation). Additionally, by increasing the interelement separation to 6λ, CCDFs of different zones become consistent over a range of 500 m, meaning that capacity performance does not degrade as distance increases, and therefore, performance consistency has also been achieved.

Zone-specific characterization proposed in this study, can be used in underground tunnels, and particularly in mines, in which depending on the application, coverage zones may differ from mine to mine and even from level to level within the same mine. Such studies can accelerate deployment of MIMO-based systems for revolutionary applications such as machine-to-machine communications, which requires highly reliable and efficient communications platform.

CHAPTER 7: OPTIMIZATION OF ANTENNA PLACEMENT IN DISTRIBUTED MIMO SYSTEMS FOR UNDERGROUND MINES

7.1 Introduction

MIMO-based systems promise an increase in capacity only if the fading signals observed at the receiving antenna elements are decorrelated. If the angular spread of the signals that arrive at the receiving antenna is low and the spacing of the antenna elements is insufficient, MIMO capacity will be degraded. Because environments such as tunnels and mines show a smaller angular spread than conventional environments do, they are subject to more of this degradation, and therefore careful consideration is required for the antenna design and deployment.

One of the most recent approaches for MIMO capacity enhancement is employing distributed antennas across the area of coverage [141]-[145]. Distributed antenna systems (DAS) were originally proposed to extend coverage and to decrease delay spread [146] in conventional indoor environments, mines and tunnels. However, interest in DAS has been recently renewed due to its ability to provide high quality-of-service, universal coverage and high capacity. For such deployments, independent antenna nodes separated spatially, cooperate as a single MIMO system. Therefore, the role of DAS has evolved from merely being a repeater to being a sophisticated but a cost-effective solution that only offers both extended coverage and increased capacity.

Extensive Monte-Carlo-based studies and modeling of DAS (or D-MIMO, *i.e.*, Distribured MIMO) have been performed in recent years with the main focus on the information theory and space-time coding aspects. Most of them have been developed based on a generalized model for distributed antenna that was proposed in [141], [142]. This model assumes independent small scale fading and uncorrelated shadowing, and exploits small scale fading and shadow fading simultaneously. In [147], the authors provided a closed-form expression for the cell averaged ergodic capacity of D-MIMO, however, their modeling is based on the assumption of high signal-to-noise-ratio (SNR) and uniform user distribution. More complex models have also been developed by relaxing the assumptions of high SNR, considering correlation of small scale fading with lognormal large scale fading and considering non-uniform mobile user distributions [142]-[144].

Based on the aforementioned modelings and assumptions, general insights have been proposed by a few studies in locating base stations (BS) in outdoor environments while optimizing capacity [144],[145]. Most of these studies have evaluated capacity enhancement achieved by employing D-MIMO in comparison with C-MIMO, *i.e*., Conventional MIMO or Colocated MIMO. They have also addressed common challenges such as power imbalance among distributed antennas in D-MIMO systems, which is due to the large separation between them. Because most of these theoretical works are based on Monte-Carlo simulations and statistical channel models that are developed for conventional indoor and outdoor environments, they may not be applicable to underground tunnel environments because of their different propagation behavior. DAS has been considered in transportation tunnels previously for coverage enhancement only [73],[148]. However, no previous study concerning capacity enhancement of D-MIMO systems in underground tunnels and mines has previously been conducted.

For our analysis of D-MIMO for access-point (AP) to mobile communications, we have used a deterministic model based on the multimode waveguide model [74], which has recently been developed to model electromagnetic (EM) propagation in underground mines and tunnels. Although this theoretical model has been experimentally validated for underground environments [74], we have also verified it experimentally to ensure the accuracy of our findings for short underground mine tunnels.

By employing this model to find the channel-gain-matrix (**H-**matrix), we have optimized and compared the capacities and power distributions of C-MIMO and D-MIMO systems by finding optimal locations for the APs. While the main focus of our performance assessment in this study is on received power and channel capacity, we have also studied another performance measure, *i.e.*, the condition-number (CN) of the **H**-matrix, in some parts of our analysis.

For the optimization part, we have chosen the particle-swarm-optimization (PSO) method developed almost twenty years ago by a social psychologist and an electrical engineer [149]. This method is a widely used optimization method and well known within the EM community for its successful use in antenna design [150],[151]. The PSO is a global optimization method that performs guided random search technique over discrete search spaces. The strengths of the PSO algorithm, including its robustness in overcoming the local minima problem, its ease of implementation, and its relatively fast convergence, make it suitable for our application.

The remainder of this chapter is organized as follows. In Sec. 2, we describe the theoretical basis of the multimode waveguide model. In Sec. 3, we explain our methodology, including details of the PSO method, the relevant performance measures, our model assumptions and scenarios. In Sec. 4, we discuss our results and significant findings. Finally, in Sec. 5, we summarize the main outcomes of this study.

7.2 Multimode Waveguide Modeling and Experimental Validation

Multimode modeling, which was proposed in [74], can be used to characterize wireless propagation in tunnels. It is an accurate theoretical model for high frequencies (upper ultra-high-frequency band and above) that takes into account higher order propagation modes. By considering higher order modes as well as the dominant mode, this model accurately characterizes not only the far field but also the near field of an empty tunnel [74], and therefore can be expected to be applicable to short underground mine drifts and tunnels as well. Here, we have used this model to find the **H**-matrix and the channel capacity (b/sec/Hz). In the following sections, the formulas used for multimode modeling are given, then experimental validation of the model for a short mine tunnel is presented and discussed.

7.2.1 Multimode Waveguide Model

In the multimode model, the tunnel is considered to be an oversized dielectric waveguide. Assuming the excitation is a *y*-directed (vertically polarized) dipole, the field distribution $E_{m,n}^{eigen}$ of *y*-polarized hybrid modes at any position (*x*, *y*, *z*) inside the tunnel can be found by solving Maxwell's equations for the specified cross-sectional (transversal) dimensions and the material of the tunnel in the form of the eigenfunctions [130],[74]:

$$E_{m,n}^{eigen}(x, y) = \cos\left(\frac{m\pi}{w}x + \varphi_x\right)\sin\left(\frac{n\pi}{h}y + \varphi_y\right), \qquad (1)$$

where w and h are the tunnel width and height, respectively, and φ_x and φ_y are parity designations which take values of 0 or π/2 depending on whether the integer values of m and n are even or odd [130]. The intensity of each mode depends on the excitation that can be found by applying the geometrical-optical (GO) model in the excitation plane (transmitting plane), *i.e.*, the cross-sectional plane that contains the transmitting antenna. The EM field distribution on the transmitting plane is, in fact, the sum of the fields of all modes. The mode intensities are estimated by a mode matching technique as given in Equation (2) [74] which, assumes that the transmitter is vertically polarized (y-polarized) and located at (x_0, y_0, z_0):

$$E^{Rx}(x, y, z) = \sum_{m=1}^{\infty}\sum_{n=1}^{\infty} C_{mn}(x_0, y_0)\, E_{m,n}^{eigen}(x, y)\, e^{-(\alpha_{mn} + j\beta_{mn})|z - z_0|} \qquad (2)$$

where C_{mn}, α_{mn}, and β_{mn} are the mode intensity in the excitation plane (which depends on the transmitter location), the attenuation coefficient, and the phase shift coefficient, respectively. Using the above formulas, we have constructed 4×4 C-MIMO and D-MIMO channel matrices (**H**-matrix) as follows:

$$h_{ij} = \frac{\sqrt{G_{Tx}G_{Rx}}}{2k}\sum_{m=1}^{\infty}\sum_{n=1}^{\infty} C_{mn}^{j}(x_j, y_j)\, E_{m,n}^{eigen}(x_i, y_i)\, e^{-(\alpha_{mn} + j\beta_{mn})|z_i - z_j|} \qquad (3)$$

where, i is the receiving antenna number, j is the transmitting antenna number, h_{ij} is the complex channel gain between the i^{th} receiver and the j^{th} transmitter, G_{Tx} and G_{Rx} are the antenna gains, k is the wave number, C_{mn}^{j} is the mode intensity of the j^{th} transmitter and $E_{m,n}^{eigen}(x_i, y_i)$ is thevalue of the (m,n) mode eigenfunction as observed at the i^{th} receiver.

7.2.2 Experimental Validation of Multimode Waveguide Model

In [74], the authors compared and validated the multimode model with experimental work conducted by another group [13] at the same frequency (450 MHz and 900 MHz) and over the same axial length (2500 m). The experimental work was conducted in an arched tunnel while the multimode modeling was applied for a rectangular tunnel with the same cross sectional area as the arched tunnel, *i.e.*, 7.8 m × 5.3 m. Their comparison shows the same trend and a good match between the multimode model and the experiment, particularly for long distances between the transmitter and receiver. However, the verification for short distances is not clearly observable.

Experimental verification of the multimode model for short distances is necessary because it has been claimed that the approach is also applicable to underground mine tunnels, which are much shorter than transportation tunnels. To validate this model for short distances, we used the data we collected for an ultra-wide-band-MIMO project in an underground mine at Myra Falls in BC, Canada (Figure 7-1). The tunnel width and height are 5.1 m and 3.8 m, respectively. The measurements were taken by moving the transmitter in 2 m increments from 1 m to 49 m from the receiver for a total of 25 points, as shown in Figure 7-1. Due to the mine restrictions, it was not possible to go further than 49 m. For our channel measurements, we used an Anritsu MS2034A vector-network-analyzer (VNA) to measure frequency response over a span of 2.49-4 GHz with 551 frequency points, RF over fibre optic cable for range extension, and two biconical antennas. Additional detail regarding the measurement setup can be found in Chapter 3.

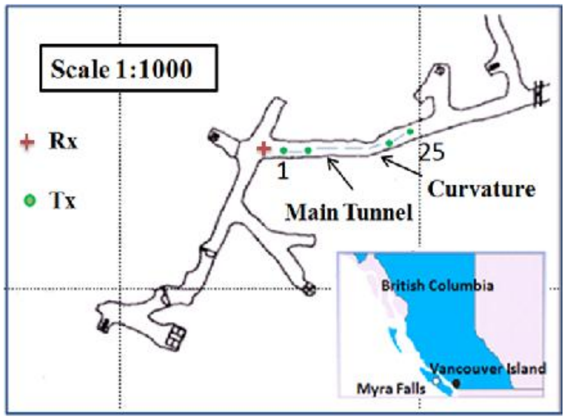

Figure 7-1 **Map of the Myra Falls mine in British Columbia, Canada and the transmitter (Tx) and receiver (Rx) locations.**

Figure 7-2 compares our experimental results with multimode modeling at 2.49 GHz for four scenarios, each of which is presented on a subplot. We have considered vertical polarization for two different transmitter and receiver heights: close to the ceiling and medium heights. Considering the fact that this mine, like most of mines has many irregularities in its geometry, overall good agreement can be seen for all the cases and for such short distances. After 35 m, the measurements and the multimode model start to diverge due to the presence of a curvature in the drift, as shown in Figure 7-1. Curvature adds extra loss that is not captured by the multimode model [109].

7.3 Optimization of C-MIMO and D-MIMO Configurations

In this section, we elaborate on how combining the multimode model with a global optimization method optimizes the performance measures that are relevant to C-MIMO and D-MIMO systems. We consider several scenarios for each system and use performance measures to evaluate and compare their performance.

7.3.1 Particle Swarm Optimization Method

The PSO algorithm optimizes a problem by iteratively trying to improve a candidate solution with regard to a given measure of quality. We used this optimization algorithm to optimize the average capacity inside the tunnel. We formulated the cost function as follows:

$$\text{cost} = \left(\frac{average(Capacity)}{desired(Capacity)} \right)^2 \tag{4}$$

where the average capacity is found by considering a grid of receivers, and desired capacity is the capacity of an independent-identically-distributed (i.i.d.) Rayleigh fading channel at a given SNR.

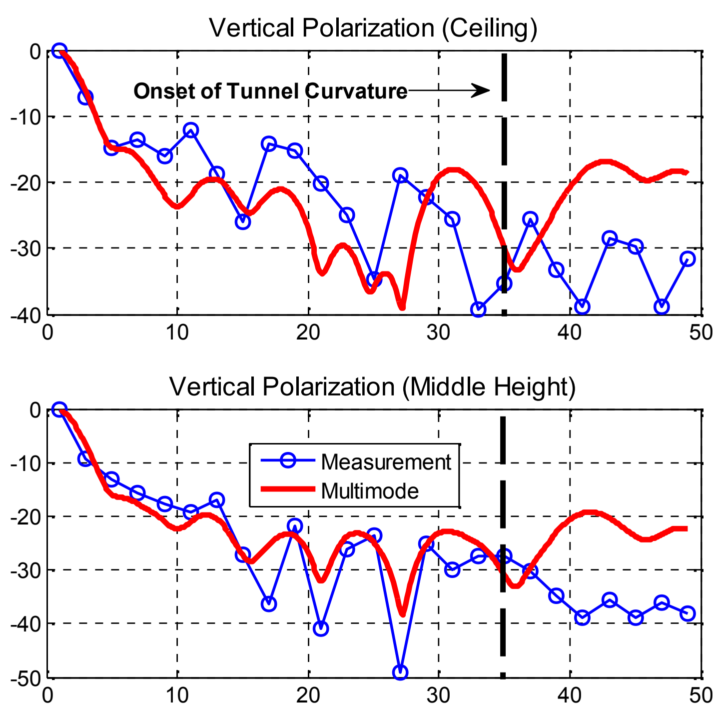

Figure 7-2 Experimental validation of multimode model in a short underground mine tunnel; antennas are placed at medium height and close to the ceiling.

In the PSO method, the particles (APs) are initially placed randomly in a search space, and then move through the search space based on (5). Assume there are M particles in a swarm, along with *N* geometrical parameters to be optimized. In our study, 10 AP sets are considered as the particles (M=10) and each AP set consists of 4 antennas, each of which has a 3D location vector (*x, y, z*) (N=12). At each iteration, the particles' positions and velocities are updated and stored in *X* and *V* matrices, respectively. As (5) shows, at each iteration, the velocity of each particle is determined by the distances from its current position to the "personal best" (p_{best}) and the "global best" (g_{best}) locations. The p_{best} is each particle's personal knowledge, the locations where each particle (AP) attains its best fitness value (average capacity) up to the current iteration, and g_{best} is the global (or swarm) knowledge, which is chosen from the *M* p_{best}'s, the location where the best fitness value was attained by any particle (locations of an AP set which gives the highest average capacity).

$$\begin{aligned} V_t &= wV_{t-1} + c_1\eta_1\left(P_{t-1} - X_{t-1}\right) + c_2\eta_2\left(G_{t-1} - X_{t-1}\right) \\ X_t &= X_{t-1} + V_t \end{aligned} \tag{5}$$

In (5), *t* denotes the present iteration, and the are $M \times N$ matrix *P* is the particles' best local position, matrix *G* is the particles' best global position, matrix *X* is the particles' position and matrix *V* is the particles' velocity. Parameters c_1 and c_2 are scaling factors for best personal and global positions, and η_1, η_2 are randomly chosen numbers uniformly distributed over the interval [0,1]. Previous optimization studies recommend c_1 and c_2 to be 1, however, they can be chosen based on numerical experiments. Inertia weight, *w*, is in the range of [0,1]. Numerical experiments indicate that the PSO algorithm converges faster if *w* is linearly damped with iterations starting at 0.9 and decreasing linearly to 0.4 at the last iteration [152].

7.3.2 Two Performance Measures: Capacity and Condition Number

According to the literature, several performance measures for MIMO-based systems have been considered, including channel capacity and the CN of the **H-**matrix [153]-[155]. Channel capacity is defined as the highest transfer rate of information with arbitrary low probability of error, whereas CN is the ratio of the maximum to minimum singular values of the **H**-matrix with the desirable value of one. CN is often stated in dB form:

$$\begin{aligned} &\kappa(\mathbf{H}) = \frac{\sigma_{\max}}{\sigma_{\min}} \geq 1 \\ &CN(dB) = 20\log_{10}(\kappa(\mathbf{H})) = 20\log_{10}\left(\frac{\sigma_{\max}}{\sigma_{\min}}\right) \end{aligned} \tag{6}$$

where κ, **H**, σ_{max}, σ_{min}, and CN are the linear condition number, channel gain matrix, maximum singular value, minimum singular value, and condition-number in dB, respectively.

Although channel capacity and CN are associated in some ways, they are not fully correlated, and therefore CN cannot be a strong metric for capacity. Equations (6) and (7) [6] show CN and capacity, respectively. As can be seen, CN only considers the largest and smallest singular values while the capacity depends on all singular values and the eigenstructure of the subchannels [156]:

$$C = \log_2\left[\det\left(\mathbf{I}_{\mathbf{N_{Rx}}} + \frac{SNR}{N_{Tx}}\mathbf{HH}^*\right)\right] = \sum_{i=1}^{k}\log_2\left(1+\frac{SNR}{N_{Tx}}\sigma_i^2\right) \tag{7}$$

where C, **I**, SNR, N_{Rx}, N_{Tx}, k, and σ_i are capacity, identity matrix, average SNR, number of receivers, number of transmitters, number of singular values, and i^{th} singular value, respectively.

In long-term-evolution (LTE) MIMO-based systems, CN is deterministically calculated from the instantaneous **H**-matrix (without the need for stochastic averaging) and is used to estimate the increase in SNR required for successful signal demodulation [157]. It can be directly measured by some of the recently developed vector signal analyzers [157],[158]. If CN is not too high, an increase in SNR may help to compensate the degrading effect of CN. If it is too high, it implies that the **H-**matrix is ill-conditioned, and the system will suffer from irreducible error rates. Consequently, the system may need to change the multiplexing mode to other available modes, *e.g.*, beamforming or diversity.

7.3.3 Model Assumptions and Scenarios

Our analysis focuses on AP-to-mobile communications in an empty tunnel, in which the mobile terminal is a laptop with four antennas positioned around the laptop screen as illustrated in Figure 7-3. The laptop screen is assumed to be 3λ by 2λ. The length of the tunnel is 100 m and the frequency of operation is assumed to be 2.4 GHz. Transmitter and receiver antennas are vertically polarized with gain equal to one.

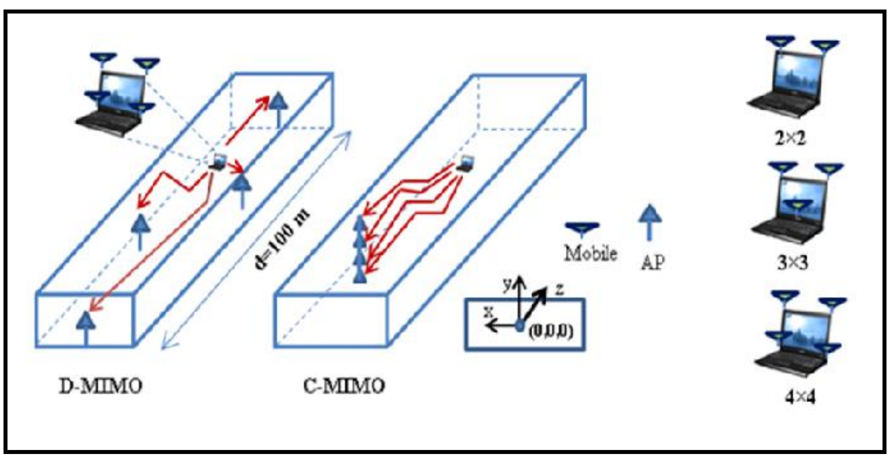

Figure 7-3 D-MIMO and C-MIMO setups for AP-to-mobile communications inside an empty rectangular tunnel.

For the C-MIMO case, four AP vertically polarized antennas are co-located in four configurations: three uniform linear arrays (vertical, horizontal, and diagonal) and one square array. The horizontal array is along the tunnel width, close to the ceiling, the vertical array is along the tunnel height and close to the sidewalls, the diagonal array is along the diagonal of tunnel cross-section, and the square configuration is aligned in parallel to the tunnel cross-section. The array along the tunnel axis was not considered because previous studies [21] show that it cannot offer significant capacity increase due to a high correlation between fading signals at the antenna elements. The linear arrays' interelement spacing is fixed and equal to 4λ while the square array's interelement spacing is 3λ by 2λ.

For the D-MIMO case, the AP antennas are distributed along the tunnel. In all cases, 300 iterations were performed to find the optimum locations for the AP antennas. In the three C-MIMO cases, the optimum location for an AP with a fixed length array was sought, while in the D-MIMO case, the locations for the distributed antennas were sought. For the D-MIMO case, we considered three system sizes: (2×2), (3×3), and (4×4).

Two scenarios of C-MIMO and D-MIMO systems for AP-to-mobile communications in a rectangular tunnel are given in Figure 7-3. In addition to vertical array, horizontal and diagonal arrays have also been considered for the C-MIMO case, which are not depicted in Figure 7-3. Because this work focuses on propagation and channel modeling aspects, capacity has been optimized without relying on power control from the transmitter. Therefore, for capacity analysis of both C-MIMO and D-MIMO, we assumed that the channel is known only at the receiver and equal power is radiated from each transmitting antenna. We set the P_{Tx} of each transmitting antenna to 0 dBm, and set the gains of the antennas at both the receiver and transmitter to one (G_{Tx}, G_{Rx}=1).

To find the AP positions that give optimum channel capacity, 300 iterations of the PSO algorithm were performed for mobile locations with the same height of 1 m over a grid of 1200 equally spaced points across the tunnel. For the D-MIMO case, four 3D position vectors indicating the location of the AP antennas were found that maximize the average capacity over the grid of receivers. For the C-MIMO case, because the AP antennas are co-located, one 3D position for the whole array has been found. The PSO algorithm was run several times for each scenario to ensure the consistency of the results. Different parameters and their values for the multimode waveguide model and PSO method are presented in Table 7-1.

7.4 Comparison of C-MIMO and D-MIMO System Performance

In this section, D-MIMO and C-MIMO performance are assessed and compared for several scenarios, including different system sizes, antenna configurations, antenna placements, and tunnel lengths. Our objectives are to determine: 1) how much enhancement is achievable by employing better performing 4×4 C-MIMO antenna configurations, 2) how the MIMO performance can be improved by optimally distributing the MIMO antennas across the tunnel rather than placing them in the same tunnel transverse plane, and 3) how the tunnel length and antenna placement can impact D-MIMO performance.

To accomplish these goals, we have considered different performance measures, including power distribution. In order to separately compare the power and other performance measures, first we analyze the power distribution, and then we study the CN and channel capacity while using normalized **H**-matrices. We also elaborate on placement strategies of AP antennas across the tunnel to enhance the capacity.

Table 7-1 Multimode and PSO simulation setup
(w: tunnel width, h: tunnel height, l: tunnel length)

Multimode Parameters	Tunnel dimension (w×h×l)	5.1×3.8×100 m^3
	Tunnel material characteristics	$\sigma = 0.01$ $\varepsilon = 5$
	Antenna polarization	Vertical
	Frequency of operation	2.4 GHz
	Mobile height	1 m
	Antenna spacing at	Mobile: 3λ,2λ C-MIMO: AP-linear:4λ AP-square:3λ,2λ
PSO Parameters	No. of iterations	300
	M: No. of particles	10
	N: No. of particles' parameters	12
	$c_1=c_2$	1

7.4.1 Power Analysis

For the C-MIMO case, power analysis is performed for different antenna configurations whereas for the D-MIMO case, it is performed for different numbers of APs. In both cases, the transmit power of each antenna is assumed to be 0 dBm (P_{Tx} = 0 dBm), and to have a fair comparison between different cases with differing number of antennas, the normalized received power of each case is plotted (Figure 7-4) using following formula:

$$P_{Normalized} = \frac{\|\mathbf{H}\|_{\mathbf{F}}^{2}}{N_{Tx} N_{Rx}} \tag{8}$$

where $\|\mathbf{H}\|_{\mathbf{F}}$ is the Frobenius norm of the **H**-matrix, and N_{Tx}, N_{Rx} are the number of transmitters and receivers, respectively. In the case of a single antenna AP (1×1 system), the **H**-matrix only has one element. Figure 7-4 illustrates the power cumulative-distribution-functions (CDF) for different C-MIMO configurations. Among them, the diagonal configuration shows better performance both in terms of %10 outage power (higher outage power) and power variation across the grid of 1200 receivers (steepest CDF).

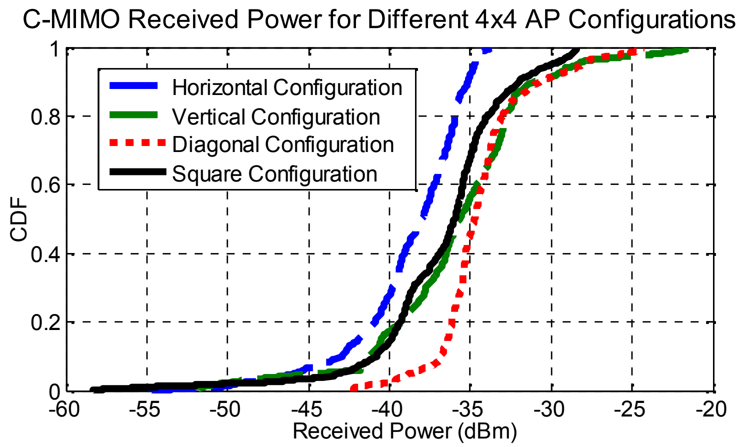

Figure 7-4 **Received power CDFs for different C-MIMO access-point configurations.**

Because antennas are spatially distributed and far apart from each other in D-MIMO systems, they are more subject to power imbalance, which is a degrading factor for D-MIMO systems. However, due to the waveguide effect in tunnels, power loss along the tunnel axis is lower compared to conventional environments, which makes D-MIMO systems even more suitable for use in tunnels. Figure 7-5 shows power CDF plots for different size D-MIMO systems where antennas are uniformly distributed inside the tunnel. In the case of a single antenna AP, the antenna is located in the middle of the tunnel. As can be seen in Figure 7-5, the CDF of 4×4 D-MIMO is the steepest CDF, which implies that it has the least power variation across the tunnel, and therefore is less vulnerable to power imbalance whereas 1×1 has the highest variation (least steep CDF). Figure 7-5 shows how power distribution changes for different size D-MIMO systems in a 100-m tunnel. Comparing the 4×4 D-MIMO case in Figure 7-5 with the cases in Figure 7-4, we can see that 4×4 D-MIMO offers lower power variation across the tunnel compared to C-MIMO configurations with similar size.

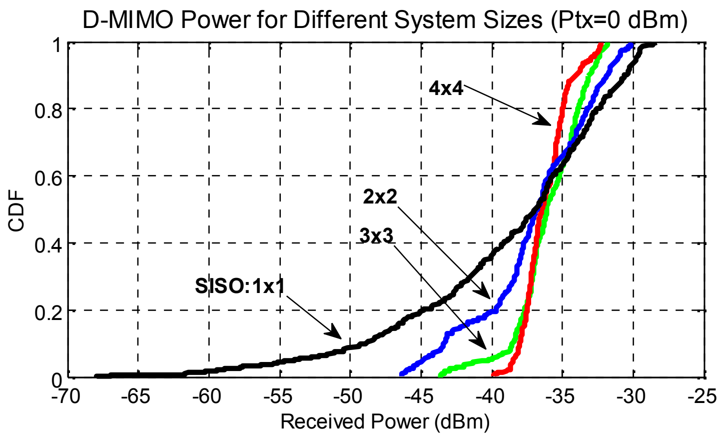

Figure 7-5 Received power CDFs for different D-MIMO system sizes.

The aforementioned setup for APs in which they were equally and uniformly distributed along the tunnel offers relatively balanced power, however, it does not necessarily offer optimum capacity and CN. In the next section, we will see that performing the PSO algorithm to distribute the antennas optimally can optimize capacity.

7.4.2 Capacity and Condition Number Analysis

For capacity analysis of C-MIMO, we have used (1) - (3) to construct 4×4 C-MIMO channel gain matrices and calculate channel capacity [6]:

$$C = \log_2\left[\det\left(\mathbf{I}_{\mathbf{N_{Rx}}} + \frac{SNR}{N_{Tx}}\mathbf{HH}^*\right)\right] \tag{9}$$

where * denotes the transpose-conjugate, N_{Tx} is the number of the transmitting antennas, N_{Rx} is the number of receiving antennas, $\mathbf{H}$ is the $N_{Rx}\times N_{Tx}$ normalized channel gain matrix (based on the Frobenius norm) and we have assumed that the N_{Tx} sources have equal power and are uncorrelated. Because the **H**-matrix is normalized in this formula, pathloss is removed, and therefore capacity is mainly controlled by the degree of correlation between the subchannels.

Figure 7-6 shows the capacity CDFs of different 4×4 C-MIMO configurations. They are all lower than the capacity for the case with i.i.d. Rayleigh fading channels. As can be seen, C-MIMO capacity is highly dependent on the AP configurations. MIMO horizontal and vertical array configurations offer very low capacity in most parts of the tunnel. The diagonal configuration offers the best performance in terms of both power and capacity, but may not be a practical solution. Square C-MIMO shows similar average capacity to diagonal configuration, however, its outage capacity is much lower than that of diagonal and its capacity variation across the tunnel is very large compared to its counterparts.

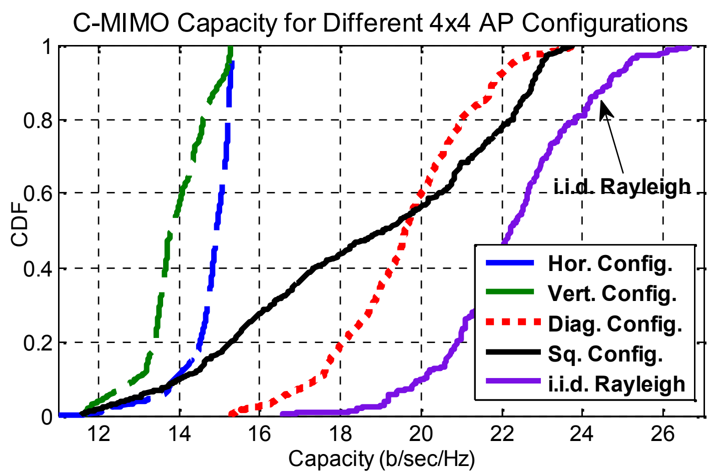

Figure 7-6 **Capacity CDFs for different C-MIMO access-point configurations.**

We increased the interelement spacing between the AP antennas for C-MIMO cases but no improvement was achieved. This may be due to limited size of the array at the mobile terminal and the low angular spread inside the tunnel. For such scenarios, the angular spread is too low to provide sufficient decorrelation among the C-MIMO subchannels, and due to the constraints imposed by the size of the tunnel cross-section, further increasing the element spacing is not possible. Figure 7-7 compares D-MIMO capacities with their i.i.d. Rayleigh counterparts. They are all close to i.i.d. Rayleigh capacity except for the 4×4 case. This shows that increasing the number of antennas increases the capacity, however, full multiplexing gain may not be achieved.

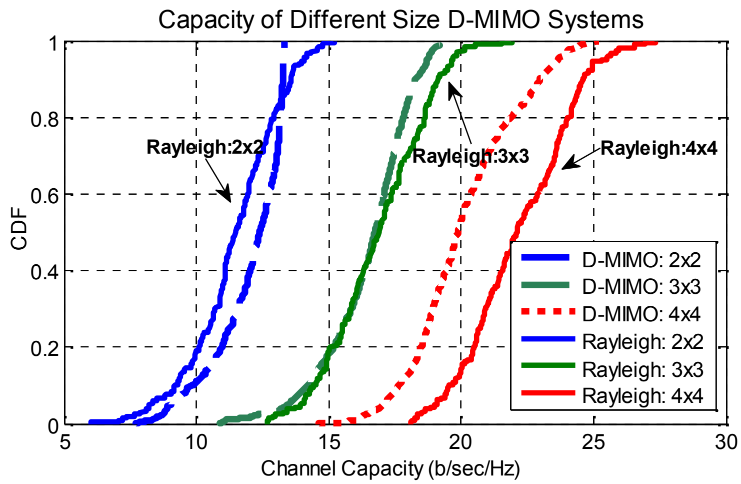

Figure 7-7 Capacity CDFs for different D-MIMO system sizes.

The CNs of all C-MIMO configurations were found to be very poor for most cases, which confirms that full multiplexing gain cannot be achieved by the 4×4 C-MIMO systems we have considered in the tunnel under study. Figure 7-8 compares CN of D-MIMO systems. As it is shown, 2×2 D-MIMO shows the best CN, which is very close to that of an i.i.d. Rayleigh fading channel. For larger size D-MIMO systems, higher capacity can be achieved (as is shown in Figure 7-7), however, they are more susceptible to noise (as is shown in Figure 7-8).

From Figure 7-5, Figure 7-7, and Figure 7-8, it can be concluded that among the scenarios that we considered, 2×2 D-MIMO shows desirable performance in terms of power, capacity and CN. By employing 3×3 D-MIMO, high capacity is still achievable, however, its CN shows it is more susceptible to the noise compared to 2×2 D-MIMO systems. For larger size D-MIMO systems, if full multiplexing gain is not achievable, it may be more appropriate to consider both multiplexing and diversity gains to obtain enhancement of the capacity as well as reliability.

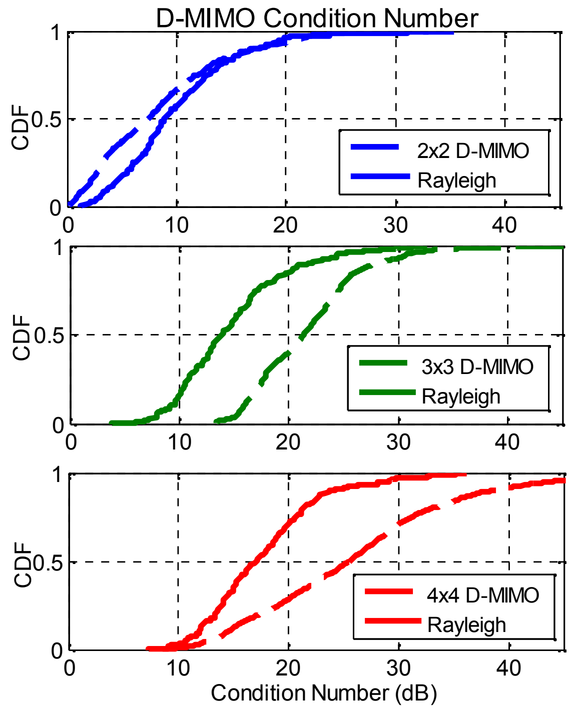

Figure 7-8 Condition number CDFs for different D-MIMO system sizes.

7.4.3 Impact of Antenna Placement on 2×2 D-MIMO Performance

In this section, we show how much performance enhancement is achievable by properly positioning APs in the cross-sectional plane of the tunnel. For this purpose, we have considered the following cases: (1) APs are distributed uniformly along the tunnel axis ($z_1 = \frac{100}{3}, z_2 = \frac{2*100}{3}$) and placed at the center of the tunnel (x = 0, y = 0), (2) APs are distributed uniformly along the tunnel axis, placed at the medium height (y = 0) and close to the sidewalls (1/5th – 1/4th of the tunnel width from the sidewalls), (3) APs are first distributed uniformly along the tunnel axis, and then PSO finds the cross-sectional (xy-plane) locations that optimize capacity (PSO algorithm with constraint), and (4) PSO finds APs' locations everywhere inside the tunnel that optimize capacity (PSO algorithm with no constraint). Final results are given in Figure 7-9.

Figure 7-9 shows that although uniformly distributing the APs along the tunnel axis and locating them at the center of the tunnel offer optimum power distribution, optimum capacity may not be achieved. On the other hand, AP locations that offer optimum capacity do not necessarily lead to optimum power distribution. Two other cases that are very similar fall in between. By running PSO several times, we have observed that by first uniformly distributing APs along the tunnel axis, and then placing them in $1/5^{th}$ – $1/4^{th}$ of the tunnel width from the sidewalls with medium height (y = 0), desirable performance (both capacity and power distribution) can be achieved. In addition, we found that performance may be improved further by shifting antennas from the medium height towards the ceiling ($1/5^{th}$ – $1/4^{th}$ of the tunnel height from the ceiling). Physical interpretation for achieving better performance from placing APs at off-centered locations in the transverse plane can be attributed to the excitation of larger number of waveguide propagation modes in off-centered locations, which leads to an increase in decorrelation of D-MIMO subchannels.

Based on the aforementioned results, the following strategy can be employed for AP antenna deployment based on D-MIMO system. First, based on desired power and capacity, the number of APs should be set. Then, APs should be uniformly distributed along the tunnel axis (z-axis) and placed close to the sidewalls and ceiling. To find the optimal cross-sectional location, which may differ from mine to mine and for different size MIMO systems (*e.g.*, 3×3 or 4×4), position adjusments (fine position tuning) can be performed on the cross-sectional plane. By uniformly distributing APs, one is less likely to encounter power imbalance problems, and therefore one wll be less dependent on AP power control at the transmitter. Furthermore, by placing APs in the appropriate cross-sectional position, desirable capacity is achievable without degrading the power (as shown in Figure 7-9).

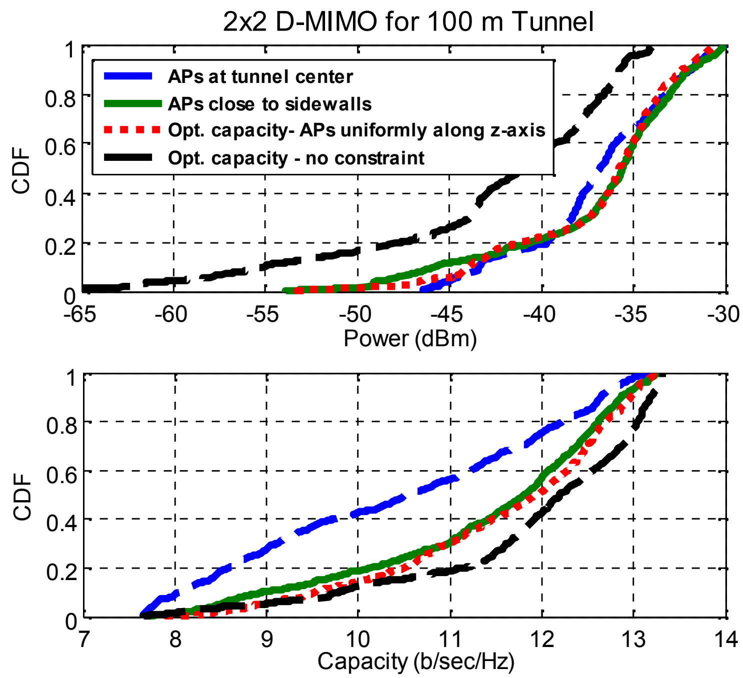

Figure 7-9 2×2 D-MIMO system performance for several scenarios.

7.4.4 Impact of Tunnel Length on D-MIMO Performance

In this section, we show how tunnel length impacts power and capacity distributions of 2×2 D-MIMO systems. For this purpose, three tunnel lengths, 100 m, 300 m, and 600 m, are considered. Figure 7-10 and Figure 7-11 show power and capacity distributions of a 2×2 D-MIMO configuration for different tunnel length and different placements of AP in the transverse plane. The results show that for a 2×2 D-MIMO system, the power distribution is more sensitive to the tunnel length while the capacity distribution is more sensitive to the cross-sectional location of APs. In addition, Figure 7-11 shows that in all cases, the capacity is higher for AP locations close to the sidewalls compared to the center location.

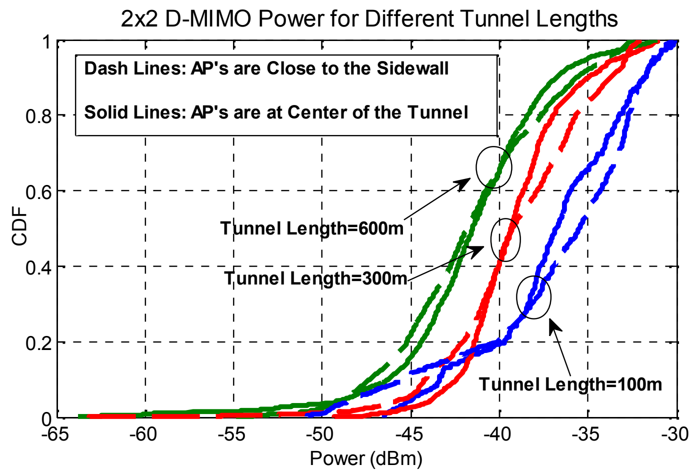

Figure 7-10 **2×2 D-MIMO power distribution for different cross-sectional locations of APs in tunnels with different lengths.**

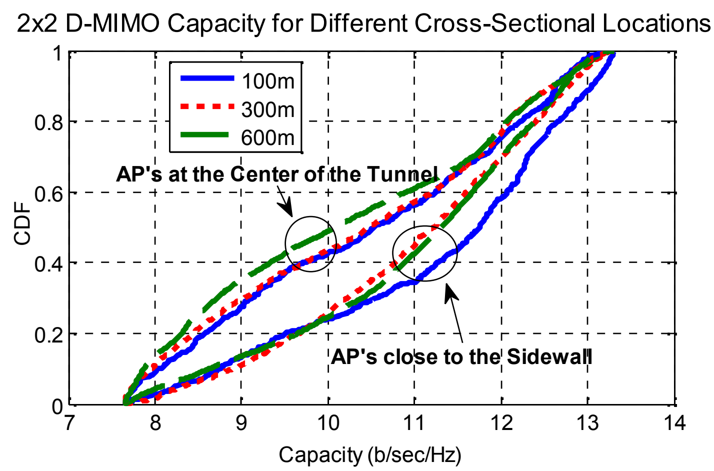

Figure 7-11 **2×2 D-MIMO capacity distribution for different cross-sectional locations of APs in tunnels with different lengths.**

For AP positions that offer higher capacity, *i.e.*, close to the sidewall and ceiling (about 1/5th - 1/4th of the width and height), we have also compared and evaluated different size D-MIMO systems for tunnels with different lengths. As Figure 7-12 illustrates, 2×2 D-MIMO capacity remains almost the same for the three considered lengths, whereas the larger D-MIMO sizes; capacity decreases as the tunnel length increases. As it can be seen, the deviation of capacity CDFs for different tunnel lengths increases as the size of D-MIMO system increases.

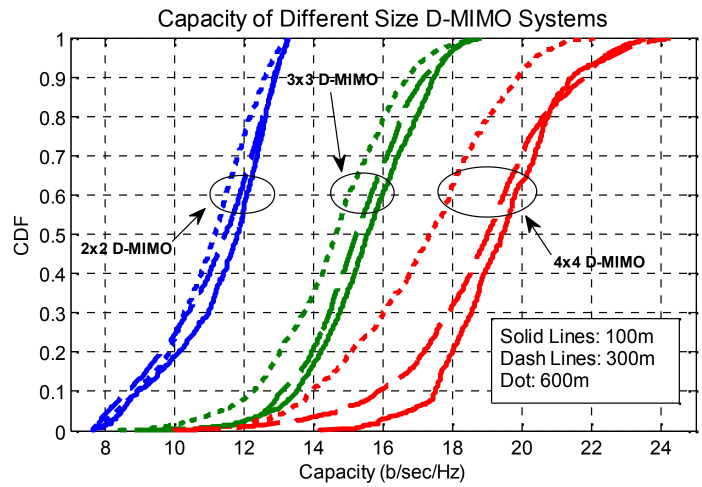

Figure 7-12 Comparison of different size D-MIMO systems for several tunnel lengths with AP locations close to the sidewall and ceiling (1/5th- 1/4th of the width and height).

7.5 Conclusions

In this study, we have developed a novel technique to assess, compare and optimize the performance of co-located and distributed MIMO systems for AP-to-mobile communications in underground short tunnels (*e.g.,* mines). This technique combines the recently developed multimode waveguide model with the PSO global optimization method to find optimal locations of APs in a short rectangular tunnel. Because the verification of the multimode waveguide model performed previously for short tunnels was not as clear as it is for long ones, we verified it with our experimental work in an underground mine to ensure the applicability of the model to short tunnels.

Assessing several C-MIMO antenna deployments for AP-to-mobile communications, we found that C-MIMO may not show the performance it is capable of in above-ground environments, which can be attributed to the very low angular spread in underground tunnels and high correlation among antenna elements at mobile station. The common practice of increasing the spacing of array elements may not be considered as a solution because of the constraints imposed by the tunnel cross-sectional size. This study reveals that low angular spread can be overcome by employing D-MIMO systems. In comparison with C-MIMO deployments, significant improvement in capacity and power distribution can be achieved. However, the level of the improvement is critically dependent on the AP locations. If AP antennas are optimally distributed across the tunnel, they can noticeably outperform co-located deployments.

The results of this study have allowed us to develop a deployment strategy for D-MIMO based APs, which takes into account both channel capacity and power distribution across the tunnel, and can be summarized as follows: 1) uniformly distributing the APs along the tunnel (for desirable power distribution) and 2) optimizing their locations on the transverse plane (tuning for higher capacity); in this way higher capacity can be achieved without degrading the power distribution. The optimum locations of D-MIMO antennas are found to be close to the sidewalls (about $1/5^{th}$-$1/4^{th}$ of the tunnel width from the wall) and ceiling (about $1/5^{th}$-$1/4^{th}$ of the tunnel height from the ceiling), as in these locations larger number of higher order waveguide modes can be excited. We also showed that tunnel length and antenna transverse location impact the power distribution and channel capacity of different size D-MIMO systems. For 2×2 D-MIMO systems in particular, the impact of tunnel length found to be more evident on the power distribution, while the impact of antenna transverse location found to be more evident on the capacity.

The results of this study confirm that D-MIMO systems can be a suitable alternative to facilitate development of applications that require high data-rate in underground tunnels and mines. One of such applications can be transmission of real-time 3D high definition video streaming of the mining process from the face area to the surface or other safe terminals to enhance tele-mining procedure, which makes mines safer and more productive work places. This work can be improved further by including the impact of tunnel geometry (*e.g.*, curvature) and infrastructure in the model that are expected to affect the performance of D-MIMO systems.

CHAPTER 8: CONCLUSIONS

We have achieved our objectives and thereby contributed to the efficient and effective deployment of MIMO-based wireless systems in underground mines and transportation systems.

8.1 Contributions

The overarching contributions of this work are: 1) determination of the reduction in the angular spread of multipath signals that arrive at the receiver in an underground mine compared to that observed in conventional surface environments and the manner in which it decreases with increasing transmitter-receiver separation and 2) demonstration that the antenna elements in MIMO antenna arrays used in underground environments must therefore be separated by several wavelengths (rather than the customary half-wavelength used in surface environments) in order to achieve acceptable performance. Further, the separation between the antennas must increase as the transmitter-receiver separation increases, higher order modes attenuate and, as a consequence, angular spread decreases.

More specific contributions are as follows: Our MIMO channel measurement system (described in Chapter 3) performed well and allowed us to conduct measurement campaigns in relatively harsh underground mine and tunnel environments including a service tunnel underneath the Woodward Instructional Resources Centre at the University of British Columbia and a lead-zinc mine operated by Nystar Mining at Myra Falls, BC. Since then, the underlying platform has become a permanent part of our lab's research infrastructure and has been used by several other teams to conduct their own measurement campaigns.

The measurement campaigns conducted in the service tunnel at UBC and the underground mine at Myra Falls (described in Chapters 4 and 5) allowed us to verify that the trends and values revealed by ray-tracing and multimode waveguide modelling are substantially correct despite the simplifications and assumptions inherent to these approaches. Among different practical scenarios, we identified two better performing antenna array configurations: (1) a horizontal array oriented perpendicular to the tunnel axis and placed under the ceiling with vertically polarized antennas, (2) a vertical array placed close to one of the sidewalls with horizontally polarized antennas. These two better performing array configurations perform differently depending on the existence of extensive infrastructure. The results obtained during our measurement campaigns also allowed us to verify that the multimode waveguide model accurately predicts path loss for transmitter-receiver separations of less than 100 metres (as described in Chapter 6).

The multimode waveguide model (described in Chapter 6) allowed us to characterize angular-spread and MIMO channel capacity and reveal that the angle of arrival distribution in underground mines closely follows a Gaussian distribution and the manner in which angular spread decreases with increasing transmitter-receiver separation. We note that these observations are sufficient to permit the correlation matrix required to extend the IEEE 802.11n MIMO channel model to underground mining environments.

Finally, we have used the multimode waveguide model in combination with particle swarm optimization (PSO) to realize a novel technique for assessing and optimizing the performance of Distributed-MIMO (D-MIMO) antenna systems in underground mine environments (as described in Chapter 7). While D-MIMO systems are deployed in other environments due to mitigating shadowing (diversity gain) or multiplexing gain, shadowing is not a concern in straight sections of tunnels. In such cases, we recognize for the first time that the D-MIMO solution is more attractive for longer-range applications due to the reduction of angular spread versus distance compared to conventional MIMO. D-MIMO system performance is greatly dependent on the axial distribution of the antennas as well as their location in the cross-sectional plane.

8.2 Recommendations for Future Work

The focus of our work for the most part was on fundamental issues associated with wave propagation in straight sections. The next step will be to pursue a follow on study of wave propagation in the vicinity of more complicated geometries such as bends and junctions. Toward this end, it would be useful to establish the feasibility of combining the multimode waveguide model with ray-tracing so that runtime and implementation issues for handling more complex and arbitrary geometries (*e.g.*, walls' tilt, indentation, curvature, branches, and infrastructure) can be resolved. This can be implemented by dividing the study area into two sections separated by a planar boundary. One section can have arbitrary geometry and the other one should have a canonical waveguide shape. EM field distribution on the boundary plane (excitation plane) can be determined using the ray-tracing method. This field distribution can be viewed as the weighted sum of the field of all modes. The mode intensities are estimated by a mode-matching technique. Once the mode intensity is determined in the excitation plane, the EM field in the rest of the tunnel can be predicted by summing the EM field of each mode.

It would be useful to determine whether it is necessary to include surface roughness in modelings (while it is desirable to keep models as compact as possible). Surface roughness may be neglected for cases in which antennas are not very close to the wall/ceiling. However, it may need to be considered if antennas are very close or attached to the walls. In addition, to make the multimode waveguide model more general, the radiation pattern of the antenna can also be included.

REFERENCES

[1] “Rock Solid: The Mining Industry in British Columbia 2008,” PriceWaterhouseCoopers LLP, Vancouver, BC, 5 May 2009, 32 pp.

[2] P. Delogne, *Leaky Feeders and Subsurface Radio Communication*, Stevenage, UK: Peter Pegrinus, 1982.

[3] P. Delogne, “Mini-review: EM propagation in tunnels,” *IEEE Trans. Antennas Propag.*, vol. 39, pp. 401-406, 1991.

[4] W. C. Jakes, *Microwave Mobile Communications*, New York: McGraw-Hill, pp. 110, 1974, p. 110.

[5] D. J. R. Martin, “Leaky-feeder radio communication: a historical review,” in *Proc. IEEE VTC ‘84*, 21-23 May 1984, pp. 25-30.

[6] J. Foschini and M. Gans “On the limit of wireless communications in a fading environment when using multiple antennas,” *Wireless Personal Commun.*, vol. 6, pp. 311-335, 1998.

[7] P. Almers, *et al.*, “Survey of channel and radio propagation models for wireless MIMO systems,” *EURASIP J. Wireless Commun. Networking*, vol. 2007, article ID 19070, 19 pp.

[8] P. E. Mogensen *et al*., “Antenna arrays and space division multiple access,” in *GSM Evolution Towards 3rd Generation Systems*, Editors: Z. Zvonar, P. Jung and K. Kammerlander, Dordrecht, The Netherlands: Kluwer Academic Publishers, 1999, pp. 122-123.

[9] K. Haneda, J. Poutanen, L. Liu, C. Oestges, F. Tufvesson, and P. Vainikainen, “Comparison of delay and angular spreads between channel measurements and the COST2100 channel model,” in *Proc. IEEE AP-URSI*, Nov. 2010, pp. 477-480.

[10] A. Paulraj, R. Nabar, and D. Gore, “Space-Time Propagation,” *Introduction to Space Time Wireless Communications*, Cambridge: University Press, 2003, p. 24.

[11] A. Emslie, R. Lagace, and P. Strong, “Theory of the propagation of UHF radio waves in coal mine tunnels,” *IEEE Trans. Antennas Propag.*, vol. 23, pp. 192-205, 1975.

[12] M. Lienard and P. Degauque, “Natural wave propagation in mine environments,” *IEEE Trans. Antennas Propag.*, vol. 48, pp.1326-1339, 2000.

[13] D. G. Dudley, M. Lienard, S.F. Mahmoud, and P. Degauque, “Wireless propagation in tunnels,” *IEEE Antennas Propag. Mag.*, vol. 49, pp. 11-26, 2007.

[14] S. F. Mahmoud and J. R. Wait, “Geometrical optical approach for electromagnetic wave propagation in rectangular mine tunnels,” *Radio Sci.*, vol. 9, pp. 1147–1158, 1974.

[15] Y. Hwang, Y. P. Zhang, and R. G. Kouyoumjian, "Ray-optical prediction of radio-wave propagation characteristics in tunnel environments, Part 1: Theory," *IEEE Trans. Antennas Propag.*, vol. 46, pp. 1328-1336, 1998.

[16] D. Didascalou, T. M. Schafer, F. Weinmann, and W. Wiesbeck, "Ray-density normalization for ray-optical wave propagation modeling in arbitrarily shaped tunnels," *IEEE Trans. Antennas Propag.*, vol. 48, pp. 1316-1325, 2000.

[17] A. H. Wong, M. J. Neve, and K. W. Sowerby, "Antenna selection and deployment strategies for indoor wireless communication systems," *IET Commun.*, vol.4, pp. 732-738, 2007.

[18] C. Hermosilla, R. Feick, R. Valenzuela, and L. Ahumada, "Improving MIMO capacity with directive antennas for outdoor-indoor scenarios," *IEEE Trans. Wireless Commun.*, vol. 8, pp. 2177-2181, 2009.

[19] P. Kyritsi, D. C. Cox, R. A. Valenzuela, and P. W. Wolniansky, "Correlation analysis based on MIMO channel measurements in an indoor environment," *IEEE J. Sel. Areas Commun.*, vol. 21, pp. 713-720, 2003.

[20] P. Kyritsi, D. C. Cox, R. A. Valenzuela, and P. W. Wolniansky, "Effect of antenna polarization on the capacity of a multiple element system in an indoor environment," *IEEE J. Sel. Areas Commun.*, vol. 20, pp. 1227-1239, 2002.

[21] M. Lienard, P. Degauque, J. Baudet, and D. Degardin, "Investigation on MIMO channels in subway tunnels," *IEEE J. Sel. Areas Commun.*, vol. 21, pp. 332-339, 2003.

[22] J. Molina-Garcia-Pardo, M. Lienard, P. Stefanut, and P. Degauque, "Propagation in tunnels: experimental investigations and channel modeling in a wide frequency band for MIMO applications," *EURASIP J. Wireless Commun. Netw.*, vol. 2009, pp. 1-9, 2009.

[23] M. Lienard and P. Degauque, "MIMO communication in tunnels: Influence of the range and of the tunnel geometry on system performances," *Proc. Wireless Commun. Sys.*, 2004, pp. 290-293.

[24] J. Molina-Garcia-Pardo, M. Lienard, P. Degauque, D.G. Dudley, and L. Juan-Llacer, "Interpretation of MIMO channel characteristics in rectangular tunnels from modal theory," *IEEE Trans. Veh. Technol.*, vol. 57, pp. 1974-1979, 2008.

[25] http://en.wikipedia.org/wiki/Mining, visited on May 2012.

[26] "Mine 2010: Back to the Boom," *Price Waterhouse Coopers*, 2010.

[27] "World mining equipment: Industry forecasts for 2013 and 2018," *Freedonia Group*, 2009.

[28] D. G. Large, L. Ball, and A. J. Farstad, "Radio transmission to and from underground coal mines-Theory and experiment," *IEEE Trans. Commun.*, vol. 21, pp. 194–202, 1973.

[29] R. S. Nutter and M. D. Aldridge, “Status of mine monitoring and communications,” *IEEE Trans. Ind. Appl.*, vol. 24, pp. 820–826, 1988.

[30] P. Delogne, “The INIEX mine communications systems,” in *Proc. Radio: Roads Tunnels Mines*, Apr. 1974, pp. 129–136.

[31] J. Murphy and H. E. Parkinson, “Underground mine communications,” in *Proc. IEEE*, Jan. 1978, pp. 26–50.

[32] D. J. R. Martin and R. Webster, “The use of radio in British coal mines,” in *Proc. Radio: Road Tunnels Mines*, Apr. 1974, pp. 110–128.

[33] D. J. R. Martin, “Leaky-feeder radio communication: A historical review,” in *Proc. IEEE VTC*, May 1984, pp. 25–30.

[34] P. Delogne, “EM propagation in tunnels,” *IEEE Trans. Antennas Propag.*, vol. 39, pp. 401–406, 1991.

[35] “Underground coal mining disasters and fatalities-U.S. 1900-2006.” [Online]. Available: http://www.cdc.gov/mmwr/preview/mmwrhtml/mm5751a3.htm

[36] L. K. Bandyopadhyay, S. K. Chaulya, P. K. Mishra, and A. Choure, “Wireless information and safety system for underground mines,” in *Proc. URSI*, Aug. 2008, pp. 9–16.

[37] K. Srinivasan, M. Ndoh, and K. Kaluri, “Advanced wireless networks for underground mine communications,” in *Proc. IEEE ICWCUCA*, Jun. 2005, pp. 51–54.

[38] W. H. Schiffbauer and J. F. Brune, “Coal mine communications,” *American Longwall Mag.*, 2006.

[39] P. Laliberte, “Summary study of underground communications technologies-Final project report,” *CANMET*, 2009.

[40] “OMSHR.” [Online]. Available:

http://www.cdc.gov/niosh/mining/works/publicationlist.html

[41] S. Yarkan, S. Guzelgoz, H. Arslan, and R. Murphy, “Underground mine communications: A survey,” *IEEE Commun. Surv. Tutorials*, vol. 11, pp. 125–142, 2009.

[42] T. Sarkar, Z. Ji, K. Kim, A. Medouri, and M. Salazar-Palma, “A survey of various propagation models for mobile communication,” *IEEE Trans. Antennas Propag.*, vol. 45, pp. 51–82, 2003.

[43] D. G. Michelson and S. S. Ghassemzadeh, “Measurement and modeling of wireless channels,” in *New Directions in Wireless Communications Research,*, V. Tarokh, Ed. Springer, 2009, ch. 1, pp. 1–27.

[44] W. Pittman and R. Church, “Through-the-earth electromagnetic trapped miner location systems: A review,” *Bureau of Mines*, 1985.

[45] D. Hill and J. Wait, “Theoretical noise and propagation models for through-the-earth communication,” *U.S. Bureau Mines*, 1982.

[46] J. Durkin, “Apparent earth conductivity over coal mines as estimated from through-the-earth electromagnetic transmission tests,” *U.S. Bureau of Mines*, 1984.

[47] T. D. Barkand, N. W. Damiano, and W. A. Shumaker, “Through-the earth, two-way, mine emergency, voice communication systems,” in *Proc. IAS*, Oct. 2006, pp. 955–958.

[48] C. J. Bise, R. Ferriter, J. Joy, J. A. Lamonica, D. Lauriski, J. Main, J. N. Murphy, and W. York-Feirn, “Improving mine safety technology and training: Establishing U.S. global leadership,” *Mine Safety Technol. Training Commission*, pp. 2–4, 2006.

[49] “Mine site technologies.” [Online]. Available:

http://www.minesite.com.au/applications

[50] A. Chehri, P. Fortier, and P. M. Tardif, “UWB-based sensor networks for localization in mining environments,” *Elsevier Ad Hoc Netw.*, vol. 7, pp. 987–1000, 2009.

[51] D. Frielos, “Xstrata mines RFID´s benefits,” *RFID J.*, 2007.

[52] “Becker Varis.” [Online]. Available: http://www.varismine.com

[53] D. A. Hill, *Radio Wave Propagation Ground Effects*, V. Tarokh, Ed. Wiley, 2005.

[54] A. C. Tripp, R. McNearny, and C. Furse, “Prof. James R. Wait and mining production technology-An appreciation,” *IEEE Trans. Antennas Propag.*, vol. 48, pp. 1438–1441, 2000.

[55] S. F. Mahmoud, “On the attenuation of monofilar and bifilar modes in mine tunnels,” *IEEE Trans. Microw. Theory Techn.*, vol. 22, pp. 845– 847, 1974.

[56] S. F. Mahmoud and J. R. Wait, “Theory of wave propagation along a thin wire inside a rectangular waveguide,” *Radio Sci.*, vol. 9, pp. 417–420, 1974.

[57] D. T. Updyke, W. C. Muhler, and H. C. Turnage, “An evaluation of leaky feeder communication in underground mines,” *U. S. Dept. Interior, Bureau of Mines*, 1980.

[58] E. A. J. Marcatili and R. A. Schmeltzer, “Hollow metallic and dielectric wave-guides for long distance optical transmission and lasers,” *Bell Syst. Tech. J.*, vol. 43, pp. 1783–1809, 1964.

[59] J. I. Glaser, “Attenuation and guidance of modes on hollow dielectric waveguides,” *IEEE Trans. Microw. Theory Techn.*, vol. 17, pp. 173–174, 1969.

[60] C. Nerguizian, C. Despins, S. Affes, and M. Djadel, “Radio-channel characterization of an underground mine at 2.4 GHz,” *IEEE Trans. Wireless Commun.*, vol. 4, pp. 2441–2453, 2005.

[61] S. R. Saunders and A. Aragon-Zavala, *Antennas and Propagation for Wireless*

Communication Systems. Chichester, England: Wiley, 2007.

[62] J. R. Wait, “A fundamental difficulty in the analysis of cylindrical waveguides with impedance walls,” *IEEE Electron. Lett.*, vol. 3, pp. 87–88, 1967.

[63] J. M. Molina-Garcia-Pardo, M. Lienard, A. Nasr, and P. Degauque, “On the possibility of interpreting field variations and polarization in arched tunnels using a model for propagation in rectangular or circular tunnels,” *IEEE Trans. Antennas Propag.*, vol. 56, pp. 1206–1211, 2008.

[64] J. C. Chiba, T. Inaba, Y. Kuwamoto, O. Banno, and R. Sato, “Radio communication in tunnels,” *IEEE Trans. Microw. Theory Tech.*, vol. 26, pp. 439–443, 1978.

[65] C. L. Holloway, D. A. Hill, R. A. Dalke, and G. A. Hufford, “Radio wave propagation characteristics in lossy circular waveguides such as tunnels, mine shafts and boreholes,” *IEEE Trans. Antennas Propag.*, vol. 48, pp. 1354–1366, 2000.

[66] D. G. Dudley, “Wireless propagation in circular tunnels,” *IEEE Trans. Antennas Propag.*, vol. 53, pp. 435–441, 2005.

[67] D. G. Dudley and S. F. Mahmoud, “Linear source in a circular tunnel,” *IEEE Trans. Antennas Propag.*, vol. 54, pp. 2034–2047, 2006.

[68] Y. P. Zhang and Y. Hwang, “Enhancement of rectangular tunnel waveguide model,” in *Proc. IEEE APMC*, Dec. 1997, pp. 197–200.

[69] Y. P. Zhang, “New model for propagation loss prediction in tunnels,” *IEEE Trans. Veh. Technol.*, vol. 52, pp. 1308–1314, 2003.

[70] Z. Sun and I. Akyildiz, “Channel modeling and analysis for wireless networks in underground mines and road tunnels,” *IEEE Trans. Commun.*, vol. 58, pp. 1758–1768, 2010.

[71] Y. P. Zhang, Y. Hwang, and R. G. Kouyoumjian, “Ray-optical prediction of radio-wave propagation characteristics in tunnel environments-Part 2: Analysis and measurements,” *IEEE Trans. Antennas Propag.*, vol. 46, pp. 1337–1345, 1998.

[72] M. Lienard and P. Degauque, “Propagation in wide tunnels at 2 GHz: A statistical analysis,” *IEEE Trans. Antennas Propag.*, vol. 47, pp. 1322– 1328, 1998.

[73] T. Klemenschits and E. Bonek, “Radio coverage of road tunnels at 900 and 1800 MHz by discrete antennas,” in *Proc. IEEE PIMRC*, 1994, pp. 411–415.

[74] Y. P. Zhang, G. X. Zheng, and J. H. Sheng, “Radio propagation at 900 MHz in underground coal mines,” *IEEE Trans. Antennas Propag.*, vol. 49, pp. 757–762, 2001.

[75] M. Boutin, A. Benzakour, C. L. Despins, and S. Affes, “Radio wave characterization and modeling in underground mine tunnels,” *IEEE Trans. Antennas Propag.*, vol. 56, pp. 540–549, 2008.

[76] J. B. Keller, “Geometrical theory of diffraction,” *J. Opt. Sci. Amer.*, vol. 52,

pp. 116–130, 1962.

[77] R. Kouyoumjian and P. Pathak, “A uniform geometrical theory of diffraction for an edge in a perfectly conducting surface,” in *Proc. IEEE*, Nov. 1974, pp. 1448–1461.

[78] S. F. Mahmoud and J. R. Wait, “Geometrical optical approach for electromagnetic wave propagation in rectangular mine tunnels,” *Radio Sci.*, vol. 9, pp. 1147–1158, 1974.

[79] P. Beckmann and A. Spizzichino, *The Scattering of Electromagnetic Waves from Rough Surfaces*. Artech House, 1963, p. 124.

[80] C. I. Beard, “Coherent and incoherent scattering of microwaves from the ocean,” *IRE Trans. Antennas Propag.*, vol. 9, pp. 470–483, 1961.

[81] D. Didascalou, T. M. Schfer, F. Weinmann, and W. Wiesbeck, “Ray density normalization for ray-optical wave propagation modeling in arbitrarily shaped tunnels,” *IEEE Trans. Antennas Propag.*, vol. 48, pp. 1316–1325, 2000.

[82] P. Mariage, M. Lienard, and P. Degauque, “Theoretical and experimental approach of the propagation of high frequency waves in road tunnels,” *IEEE Trans. Antennas Propag.*, vol. 42, pp. 75–81, 1994.

[83] Y. Hwang, Y. P. Zhang, and R. G. Kouyoumjian, “Ray-optical prediction of radio wave propagation characteristics in tunnel environments-Part 1: Theory,” *IEEE Trans. Antennas Propag.*, vol. 46, pp. 1328–1336, 1998.

[84] L. Ramirez, F. Hasselmann, and Y. Zhang, “Channel characteristics in tunnels: FDTD simulations and measurement,” *J. Microw. Opt. Electromag. Appl.*, vol. 10, pp. 121–130, 2011.

[85] M. F. Hadi and S. F. Mahmoud, “Modeling wireless propagation in a rectangular tunnel with the compact-FDTD method,” in *Proc. IEEE RWS*, Jan. 2008, pp. 339–342.

[86] Y. Wu, M. Lin, and I. J. Wassell, “Modified 2D finite-difference time domain based tunnel path loss prediction for wireless sensor network applications,” *J. Commun.*, vol. 4, pp. 214–223, 2009.

[87] D. Didascalou, M. Dottling, N. Geng, and W.Wiesbeck, “An approach to include stochastic rough surface scattering into deterministic ray-optical wave propagation modeling,” *IEEE Trans. Antennas Propag.*, vol. 51, pp. 1508–1515, 2003.

[88] M. Ndoh, G. Y. Delisle, and R. Le, “A novel approach to propagation prediction in confined and diffracting rough surfaces,” *Int. J. Numer. Model*, vol. 16, pp. 535–555, 2003.

[89] A. Chehri, P. Fortier, and P. M. Tardif, “Characterization of the ultrawideband channel in confined environments with diffracting rough surfaces,” *Wireless Personal Commun.*, vol. 62, pp. 859–877, 2012.

[90] S. Boutin, M.and Affes, C. Despins, and T. Denidni, “Statistical modeling of a radio

propagation channel in an underground mine at 2.4 and 5.8 GHz," in *Proc. IEEE VTC*, vol. 1, May-Jun. 2005, pp. 78–81.

[91] Y. Rissafi, L. Talbi, and M. Ghaddar, "Experimental characterization of an UWB propagation channel in underground mines," *IEEE Trans. Antennas Propag.*, vol. 60, pp. 240–246, 2012.

[92] Y. P. Zhang and Y. Hwang, "Characterization of UHF radio propagation channels in tunnel environments for microcellular and personal communications," *IEEE Trans. Veh. Technol.*, vol. 47, pp. 283–296, 1998.

[93] J. S. Seybold, *Introduction to RF Propagation*. Wiley, 2005.

[94] B. Nkakanou, G. Y. Delisle, and N. Hakem, "Experimental characterization of ultra-wideband channel parameter measurements in an underground mine," *J. Comput. Netw. Commun.*, vol. 2011, pp. 1–7, 2011.

[95] C. Nerguizian, C. Despins, and S. Affes, "Geolocation in mines with an impulse response fingerprinting technique and neural networks," *IEEE Trans. Wireless Commun.*, vol. 5, pp. 603–611, 2006.

[96] H. I. Volos, C. R. Anderson, W. C. Headley, R. M. Buehrer, C. R. C. Silva, and A. Nieto, "Preliminary UWB propagation measurements in an underground limestone mine," in *Proc. IEEE GLOBECOM*, Nov. 2007, pp. 3770–3774.

[97] M. Lienard, P. Stefanut, and P. Degauque, "Modeling and understanding MIMO propagation in tunnels," *J. Commun.*, vol. 4, pp. 241–247, 2009.

[98] Y. Sun and B. Zhang, "System model of underground UWB based on MB-OFDM," *Int. J. Commun., Netw. Syst. Sci.*, vol. 4, pp. 59–64, 2011.

[99] X. Yuan, "Comb-type pilot-aided OFDM channel estimation for underground WLAN communications," Ph.D. dissertation, Laval University, Canada, 2007.

[100] H. Hashemi, D. Lee, and D. Ehman, "Statistical modeling of the indoor radio propagation channel: Part II," in *Proc. IEEE VTC*, May 1992, pp. 839–843.

[101] P. K. Misra, "Underground mine location sensing system," M.Sc. Thesis, University of New South Wales, Australia, 2009.

[102] J. Karedal, S. Wyne, P. Almers, F. Tufvesson, and A. Molisch, "A measurement based statistical model for industrial ultra-wideband channels," *IEEE Trans. Wireless Commun.*, vol. 6, pp. 3028–3037, 2007.

[103] D. Cassioli, M. Win, F. Vatalaro, and A. Molisch, "Low complexity rake receivers in ultra-wideband channels," *IEEE Trans. Wireless Commun.*, vol. 6, pp. 1265–1275, 2007.

[104] A. Chehri, P. Fortier, and P. Tardif, "An investigation of UWB-based wireless networks in industrial automation," *Int. J. Comput. Sci. Netw. Security*, vol. 8, pp. 179–188, 2008.

[105] L. Bernado, A. Roma, A. Paier, T. Zemen, N. Czink, J. Karedal, A. Thiel,

F. Tufvesson, A. F. Molisch, and C. F. Mecklenbrauker, “In-tunnel vehicular radio channel characterization,” in *Proc. IEEE VTC*, May 2011, pp. 1–5.

[106] P. Delogne, *Leaky Feeders and Subsurface Radio Communications*. Peter Pegrinus, 1982.

[107] A. E. Goddard, “Radio propagation measurements in coal mines at UHF and VHF,” in *Proc. Through-Earth Electromagn.*, Aug. 1973, pp. 15–17.

[108] Y. P. Zhang and Y. Hwang, “Measurements and statistical modeling of 900 MHz radio propagation channels for microcellular and personal communications in tunnels,” *Wireless Personal Communic.*, vol. 7, pp. 25–39, 1998.

[109] Y. Zhang, Y. Hwang, and P. Ching, “Characterization of UHF radio propagation channel in curved tunnels,” in *Proc. IEEE PIMRC*, Oct. 1996, pp. 798–802.

[110] Y. P. Zhang, G. X. Zheng, and J. H. Sheng, “Excitation of UHF radio waves in tunnels,” *Microw. Opt. Technol. Lett.*, vol. 22, pp. 408–410, 1999.

[111] Y. P. Zhang, “Enhancement of waveguide model for propagation-loss prediction in tunnels,” *Microw. Opt. Technol. Lett.*, vol. 30, pp. 10–12, 2001.

[112] Y. Yamaguchi, T. Honda, and M. Sengoku, “Reduction of wave propagation loss by mesh in rectangular tunnels,” *IEEE Trans. Electromagn. Compat.*, vol. 37, pp. 88–93, 1995.

[113] Y. P. Zhang, Y. Hwang, and R. Kouyoujian, “Ray-optical prediction of radio-wave propagation characteristics in tunnel environments, Part 2: Analysis and measurements,” *IEEE Trans. Antennas Propag.,* vol. 46, pp.1337-1345, 1998.

[114] Y. P. Zhang, “Novel model for propagation loss prediction in tunnels,” *IEEE Trans. Veh. Technol.,* pp. 1308-1314, 2003.

[115] I. E. Telatar, “Capacity of multi-antenna Gaussian channels,” *Eur. Trans. Telecommun.,* vol 10, pp. 569-709, 1999.

[116] M. A. Jensen and J. W. Wallace, “A review of antennas and propagation for MIMO wireless communications,” *IEEE Trans. Antennas Propag.*, vol. 52, pp.2810-2824, 2004.

[117] A. Frozena, D. J. Love, and R. W. Heath, “Simplified spatial correlation models for clustered MIMO channels with different array configurations,” *IEEE Trans. Veh. Technol.,*vol. 56, pp. 1924-1934, 2007.

[118] J. Molina-Garcia-Pardo, M. Lienard, A. Nasr, and P. Degauque, “On the possibility of interpreting field variation and polarization in arched tunnels using a model for propagation in rectangular or circular tunnels,” *IEEE Trans. Antennas Propag.*, vol. 56, pp. 1206-1211, 2008.

[119] J. Molina-Garcia-Pardo, M. Lienard, P. Degauque, C. Garcia-Pardo, and L. Juan-Llacer, “MIMO channel capacity with polarization diversity in arched Tunnels,” *IEEE Antenna Wireless Propag. Letters*, vol. 8, pp. 1186-1189, 2009.

[120] Z. Sun and I. F. Akyildiz, "Optimal MIMO antenna geometry analysis for wireless networks in underground tunnels," *Proc. IEEE GLOBECOM*, Nov. 30-Dec. 4, 2009, pp.1-6.

[121] V. R. Anreddy and M. A. Ingram, "Capacity of measured Ricean and Rayleigh indoor MIMO channels at 2.4 GHz with polarization and spatial diversity," in *Proc. IEEE WCNC*, Apr. 2006, pp. 946-951.

[122] G. Tsoulos, *MIMO System Technology for Wireless Communications (Electrical Engineering and Applied Signal Processing)*, CRC Press, Inc., 2006, p. 194.

[123] S. F. Mahmoud, "Modal propagation of high frequency electromagnetic waves in straight and curved tunnels within the earth," *J. Electromagn. Waves Appl.*, vol. 19, pp. 1611-1627, 2005.

[124] I. Ben Mabrouk, L. Talbi, and m. Nedil, "Performance evaluation of a MIMO system in underground mine gallery," *IEEE Antennas Propag. Lett*., vol. 11, pp. 830-833, 2012.

[125] T. Svantesson and J. Wallace, "Statistical characterization of the indoor MIMO channel based on LOS/NLOS measurements," in *Proc. IEEE Signals Syst. Computers, Provo, UT, USA*, Nov. 2002, pp. 1354-1358.

[126] A. Chehri, P. Fortier, H. Aniss, and P. M. Tardif, "UWB spatial fading and small scale characterization in underground mines," *IEEE Commun. Biennial Symp.*, 2006, pp. 213-218.

[127] A. Chehri, P. Fortier, and P. M. Tardif, "Characterization of the ultra-wideband channel in confined environments with diffracting rough surfaces," *Wireless Personal Commun*., vol. 62, pp. 859-877, 2012.

[128] C. Garcia-Pardo, J. Molina-Garcia-Pardo, M. Lienard, D. P. Gaillot, and P. Degauque, "Double directional channel measurements in an arched tunnel and interpretation using ray tracing in a rectangular tunnel," *PIERM*, vol. 22, pp. 91-107, 2012.

[129] Remcom Incorporated, "Wireless InSite User's Manual", version 2.6.3, PA, USA, 2011.

[130] K. D. Laakmann and W. H. Steier, "Waveguides: Characteristic modes of hollow rectangular dielectric waveguides," *Appl. Opt.*, vol. 15, pp. 1334-1340, 1976.

[131] S. M. Wentworth, "Waveguides," *Applied Electromagnetics: Early Transmission Lines Approach*, John Wiley, 2007, p. 344.

[132] V. Erceg *et al*., "IEEE P802.11 Wireless LANs," *TGn Channel Models*, 2004.

[133] L. Schumacher, K. I. Pedersen, and P. E. Mogensen, "From antenna spacings to theoretical capacities-Guidelines for simulating MIMO systems," in *Proc. IEEE PIMRC*, Sep. 2002, pp. 587-592.

[134] B. Allen, R. Brito, M. Dohler, and H. Aghvami, "Performance comparison of

spatial diversity array topologies in an OFDM based wireless LAN," *IEEE Trans. Consum. Electron.* vol. 50, pp. 420-428, 2004.

[135] H. Asplund, A. A. Glazunov, A. F. Molisch, K. I. Pedersen, and M. Steinbauer, "The COST 259 directional channel model - Part II: Macrocells," *IEEE Trans. Wireless Commun.*, vol. 5, pp. 3434-3450, 2006.

[136] K. I. Pedersen, P. E. Mogensen, and B. H. Fleury, "Power azimuth spectrum in outdoor environments," *Electron. Lett.*, vol. 33, pp. 1583-1584, 1997.

[137] Q. H. Spencer, B. D. Jeffs, M. A. Jensen, and A. L. Swindlehurst, "Modeling the statistical time and angle of arrival characteristics of an indoor multipath channel," *IEEE J. Sel. Areas Commun.*, vol. 18, pp. 347-360, 2000.

[138] C. X. Wang, X. Hong, H. Wu, and W. Xu, "Spatial-temporal correlation properties of the 3GPP spatial channel model and the Kronecker MIMO channel model," *EURASIP J. Wireless Commun. Netw.*, 2007.

[139] C. C. Chong, C. M. Tan, D. I. Laurenson, S. McLaughlin, M. A. Beach, and A. R. Nix, "A new statistical wideband spatio-temporal channel model for 5-GHz band WLAN systems," *IEEE J. Sel. Areas Commun.*, vol. 21, pp. 139-150, 2003.

[140] R. M. Bueher, "Generalized equations for spatial correlation for low to moderate angle spread," *Wireless Pers Commun.*, vol. 592, pp. 101-108, 2002.

[141] R. Wonil and A. Paulraj, "MIMO channel capacity for the distributed antenna," in *Proc. IEEE VTC,* Sep. 2002, pp. 706-709.

[142] H. Zhang and H. Dai, "On the capacity of distributed MIMO systems," in *Proc. IEEE CISS,* Mar. 2004, pp. 1-5.

[143] Z. Ni and D. Li, "Effect of fading correlation on capacity of distributed MIMO," *Proc. IEEE PIMRC,* Sep. 2004, pp. 1637-1641.

[144] X. Wang, P. Zhu, and M. Chen, "Antenna location design for generalized distributed antenna systems," *IEEE Commun. Lett.*, vol.13, pp. 315-317, 2009.

[145] W. Choi and J. G. Andrews, "Downlink performance and capacity of distributed antenna systems in a multicell environment," *IEEE Trans. Wireless Commun.*, vol. 6, pp. 69-73, 2007.

[146] A. M. Saleh, A. J. Rustako, and R. S. Roman, "Distributed antennas for indoor radio communications," *IEEE Trans. Commun.*, vol. 35, pp. 1245-1251, 1987.

[147] D. Wang, X. You, J. Wang, Y. Wang, and X. Hou, "Spectral efficiency of distributed MIMO cellular systems in a composite fading channel," in *Proc. IEEE ICC,* May 2008, pp. 1259-1264.

[148] C. Briso-Rodriguez, J. M. Cruz, and J. I. Alonso, "Measurements and modeling of distributed antenna systems in railway tunnels," *IEEE Trans. Veh. Technol.*, vol. 56, pp. 2870-2878, 2007.

[149] J. Kennedy and R. Eberhart, "Particle swarm optimization," in *Proc. IEEE ICNN*,

Nov.-Dec. 1995, pp. 1942-1948.

[150] J. Robinson and Y. Rahmat-Samii, "Particle swarm optimization in electromagnetics," *IEEE Trans. Antennas Propag.,* vol. 52, pp. 397-407, 2004.

[151] J. Nanbo and Y. Rahmat-Samii, "Advances in particle swarm optimization for antenna designs: Real-number, binary, single-objective and multiobjective implementations," *IEEE Trans. Antennas Propag.,* vol. 55, pp. 556-567, 2007.

[152] M. Shihab, Y. Najjar, N. Dib, and M. Khodier, "Design of non-uniform circular antenna arrays using particle swarm optimization," *J. Electrical Eng.,* vol. 59, pp. 216-220, 2008.

[153] V. Erceg, P. Soma, D. S. Baum, and A. J. Paulraj, "Capacity obtained from multiple-input multiple-output channel measurements in fixed wireless environments at 2.5 GHz," in *Proc. IEEE ICC*, May 2002, pp. 396-400.

[154] H. Sampath, S. Talwar, J. Tellado, V. Erceg, and A. J. Paulraj, "A 4^{th} generation MIMO-OFDM broadband wireless system: Design, performance, and field trial results," *IEEE Commun. Mag.,* vol. 40, pp.143-149, 2002.

[155] R. W. Heath and A. J. Paulraj, "Switching between diversity and multiplexing in MIMO systems," *IEEE Trans. Commun.,* vol. 53, pp. 962-968, 2005.

[156] C. Oestges, "Multi-link propagation modeling for Beyond Next Generation wireless," in *Proc. IEEE AP-URSI,* Nov. 2011, pp. 1-8.

[157] Agilent Technologies Inc., "MIMO Performance and Condition Number in LTE," *Test Application Note,* Oct. 2009.

[158] Rohde & Schwarz, "Assessing a MIMO Channel," *White Paper,* Feb. 2011.